Modeling of Total Ionizing Dose Effects in Advanced Complementary Metal-Oxide-Semiconductor Technologies

by

Ivan Sanchez Esqueda

A Dissertation Presented in Partial Fulfillment
of the Requirements for the Degree
Doctor of Philosophy

Approved April 2011 by the
Graduate Supervisory Committee:

Hugh Barnaby, Chair
Gennady Gildenblat
Keith Holbert
Dieter Schroder

ARIZONA STATE UNIVERSITY

May 2011

ABSTRACT

The increased use of commercial complementary metal-oxide-semiconductor (CMOS) technologies in harsh radiation environments has resulted in a new approach to radiation effects mitigation. This approach utilizes simulation to support the design of integrated circuits (ICs) to meet targeted tolerance specifications. Modeling the deleterious impact of ionizing radiation on ICs fabricated in advanced CMOS technologies requires understanding and analyzing the basic mechanisms that result in buildup of radiation-induced defects in specific sensitive regions. Extensive experimental studies have demonstrated that the sensitive regions are shallow trench isolation (STI) oxides. Nevertheless, very little work has been done to model the physical mechanisms that result in the buildup of radiation-induced defects and the radiation response of devices fabricated in these technologies.

A comprehensive study of the physical mechanisms contributing to the buildup of radiation-induced oxide trapped charges and the generation of interface traps in advanced CMOS devices is presented in this dissertation. The basic mechanisms contributing to the buildup of radiation-induced defects are explored using a physical model that utilizes kinetic equations that captures total ionizing dose (TID) and dose rate effects in silicon dioxide (SiO_2). These mechanisms are formulated into analytical models that calculate oxide trapped charge density (N_{ot}) and interface trap density (N_{it}) in sensitive regions of deep-submicron devices. Experiments performed on field-oxide-field-effect-transistors (FOXFETs) and metal-oxide-semiconductor (MOS) capacitors permit investigating TID effects

and provide a comparison for the radiation response of advanced CMOS devices. When used in conjunction with closed-form expressions for surface potential, the analytical models enable an accurate description of radiation-induced degradation of transistor electrical characteristics.

In this dissertation, the incorporation of TID effects in advanced CMOS devices into surface potential based compact models is also presented. The incorporation of TID effects into surface potential based compact models is accomplished through modifications of the corresponding surface potential equations (SPE), allowing the inclusion of radiation-induced defects (i.e., N_{ot} and N_{it}) into the calculations of surface potential. Verification of the compact modeling approach is achieved via comparison with experimental data obtained from FOXFETs fabricated in a 90 nm low-standby power commercial bulk CMOS technology and numerical simulations of fully-depleted (FD) silicon-on-insulator (SOI) n-channel transistors.

To my family

ACKNOWLEDGMENTS

I would like to express my greatest respect and thanks to everyone who supported me during my doctoral studies. Particularly, I would like to express my utmost gratitude to my advisor, Professor Hugh Barnaby, for his incredible support and steady guidance throughout my entire post-graduate work. I would also like to thank Professor Keith Holbert for his incredible support specially during many experiments in the radiation facilities, Professor Gennady Gildenblat for his imperative support of my work and invaluable contributions to the compact modeling efforts described in this dissertation and Professors Dieter Schroder and Dragica Vasileska for their support of my research and insightful technical discussion. I would like to also thank Philippe Adell of JPL/NASA, Harry Hjalmarson of Sandia National Labs, Kitt Reinhardt of AFOSR, Ken LaBel of NASA, Jie Chen of RMD Inc., Ronald Pease of RLP, Ronald Schrimpf of Vanderbilt University and Younes Boulghassoul of ISI/USC for their support of this work. Without the support of all of these organizations/individuals, my research would not have been possible.

I would like to thank everyone in my family specially my parents for their endless love and support. Mamá y Papá a ustedes les debo todo lo que soy, su amor y apoyo me mantienen siempre avanzando y por eso les agradezco y amo inmensamente. A mis hermanos Josué, Saúl y Lucia y a todo el resto de mi familia también les agradezco por siempre estar junto a mí, por su compañía y su constante apoyo.

TABLE OF CONTENTS

Page

Page

LIST OF TABLES

Table Page

LIST OF FIGURES

Figure Page

Figure Page

Figure Page

Figure Page

Figure Page

Figure Page

Figure Page

Figure Page

Figure Page

CHAPTER 1. INTRODUCTION

1.1 Background and Motivation

The field of *radiation-induced surface effects in semiconductors* originated in the 1960s following the detonation of the high-altitude nuclear device *Starfish* by the U. S. in 1962 and other similar events by the Soviet Union in the same year [1]. As a result of these events, an enhancement in nuclear contaminants in the Earth's Van Allen belts caused failure in the communication satellite *Telstar I* in 1963, due to detrimental effects from ionizing radiation [1]. The birth of this new field led the way for the study of radiation effects in Metal-Oxide-Semiconductor (MOS) devices as the emphasis shifted from bipolar transistors to MOS Field-Effect-Transistors (MOSFETs) used in high-density, low-power Complementary MOS (CMOS) integrated circuits required for satellite systems [1].

Prior to the failure of *Telstar I*, early efforts in the study of radiation effects in semiconductors were limited to analyzing the degradation of material properties as a result of lattice-displacement defects in bulk crystalline semiconductor materials. These effects were studied using optical absorption, electronic transport and electron spin resonance (ESR) measurement techniques on bulk semiconductor materials exposed to several types of radiation such as α-particles, neutrons, and/or protons [1, 2]. An important discovery from these studies was that minority-carrier lifetime, being an essential parameter for the operation of bipolar transistors, was the most radiation-sensitive bulk material parameter. However, it was not until the failure in *Telstar I* that the focus of

studies became that of surface related effects of ionizing-radiation in semiconductor devices.

Initial studies of total-ionizing-dose (TID) degradation in MOS devices done at the Naval Research Laboratory (NRL) in 1964 by Hughes and Giroux demonstrated a significant sensitivity to ionizing radiation in both n-channel and p-channel transistors [3]. The following year, Hughes discovered that charges generated within the oxides, rather than on the oxide surface, were responsible for the TID degradation observed in bipolar transistors with silicon dioxide (SiO_2) passivation [4, 5]. Both of these discoveries led to the adoption of MOS transistors for studying the effects of radiation-induced oxide charges since they allow convenient parameter extractions [1]. During the second half of the 1960s, the detrimental effects of ionizing radiation on MOS devices were investigated by exposing transistors and capacitors to ^{60}Co γ-rays, x-rays, and high energy electrons [1, 3-9]. These studies revealed that the key mechanisms of TID degradation were the buildup of positive oxide trapped charge (N_{ot}) in the gate-oxide region [6, 8], and the creation of surface states denoted as interface traps (N_{it}) [7-9] at the SiO_2-semiconductor interface. At the same time, studies of transient-radiation phenomena identified latchup mechanisms in CMOS integrated circuits exposed to high dose-rate ionizing radiation [1, 10].

In the early 1970s, many radiation-hardening efforts were applied to CMOS integrated circuits. Several oxides-hardening techniques were investigated for processing of gate oxide films in MOSFETs. For example, doping of the SiO_2 film, the use of double-layer oxide structures, the use of new gate insulator

materials and changing the growth conditions of SiO_2 in gate oxides [1]. A comparison of these techniques is provided in [11] via experimental extractions of radiation-induced shifts in threshold voltage (ΔV_{th}) of MOSFETs with various types of gate-oxide materials. However, as CMOS technology transitioned from aluminum gates to self-aligned polysilicon gate structures, the gain in radiation hardness was lost since new fabrication processes increased the radiation sensitivity of polysilicon MOS devices. Other advances in CMOS technology during the 1980s, required for improved reliability and higher component density in VLSI (very-large-scale of integration) circuits, presented new hardening challenges [12]. For example, new radiation-sensitive oxide structures were introduced with the implementation of local-oxidation-of-silicon (LOCOS) technique for lateral isolation of active regions. The use of LOCOS resulted in a detrimental encroachment on the channel width (i.e., the bird's beak) and increased radiation sensitivity due to charging in this region. The use of buried oxides (BOX) in fabricating silicon-on-insulator (SOI) CMOS devices for mitigating radiation-induced latchup and single-event-upset (SEU) phenomena also introduced additional TID susceptibility since charge trapping in the BOX results in back-channel leakage currents [13].

Advancements in CMOS technologies and aggressive scaling during the 1990s and 2000s progressed into submicron (i.e., feature sizes of less than 1 μm), and then deep-submicron (i.e., feature sizes of less than 0.18 μm) technologies. Most deep-submicron CMOS technologies use shallow-trench-isolation (STI) field oxides, instead of the LOCOS, for lateral isolation [14]. In addition to

allowing a higher density of integration, planarization processing and increasing reliability, STI oxides eliminate the bird's beak region therefore reducing the susceptibility to TID effects due to charge buildup in these regions. A cross-sectional diagram for a generic deep-submicron bulk CMOS technology featuring STI oxides, dual polysilicon gates and self-align silicides is shown in Fig. 1.1.

As a result of scaling, reduction in gate-oxide thickness (t_{ox}) and an increase in channel and body doping has improved the inherent radiation hardness of most deep-submicron CMOS technologies. This is due to the suppression of classical radiation threats (i.e., buildup of fixed oxide charge in the gate oxides) that, to first order, scales with oxide thickness (t_{ox}) [15]. However, the buildup of N_{ot} and N_{it} near the interface of the semiconductor body and the STI oxide still presents a potential radiation threat [16-20] and has a measurable impact on key integrated circuit (IC) specifications [21, 22]. For example, a significant increase in standby current (I_{SB}) as a function of TID is reported in [23] for unhardened SRAM circuits fabricated in a commercial 90 nm bulk CMOS process. A reduction in the SRAM cell write margin was also observed after irradiation through shifts in the switching voltages at the bit lines [23].

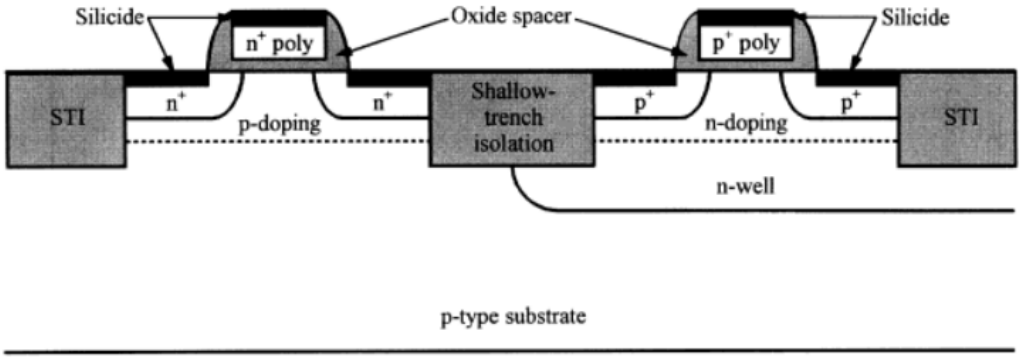

Fig. 1.1. Cross-sectional diagram for a generic deep-submicron bulk CMOS technology [24].

The deleterious impact of ionizing radiation on CMOS ICs can be mitigated through the use of well-established process hardening techniques. While radiation-hardening-by-process (RHBP) is quite a reliable method for manufacturing hardened components, it is susceptible to low volume concerns, such as yield, process instability, and high manufacturing costs [21]. Because of these disadvantages, some developers of radiation-hardened electronics prefer the use of radiation-hardening-by-design (RHBD) techniques. RHBD techniques consist of manufacturing electronic components in commercial foundries but use specialized layout and/or design approaches to mitigate radiation effects and meet radiation performance specifications. Some disadvantages of RHBD are the increased use of area and the larger gate capacitance of devices with modified topologies [21]. The impact of RHBD on power, speed, and area specifications must be taken into account, and designers must often perform detailed modeling and experiments to determine which RHBD technique needs to be implemented to meet specific mission requirements.

Even with the many technological advances and strong efforts in RHBP and RHBD, the ability to predict total-dose radiation hardness of advanced technologies from initial electrical characterization remains inadequate [1]. The elevated cost of radiation testing of on-board test structures and ICs suggest an alternative approach based on simulation and compact modeling methodologies. This approach to radiation effects characterization and analysis supports the design of ICs that meet targeted tolerance specifications for a particular environment [25]. It requires the incorporation of radiation effects into compact models that can be used in commercial circuit simulators, enabling designers to predict the operation of circuits and sub-circuits in a specific environment prior to fabrication. The purpose of this approach and its advantages can be understood by considering system level hardening activities. Shown in Fig. 1.2 is a flow diagram describing the NASA approach to radiation hardness assurance (RHA) taken from the short course on radiation-hardening at the system level presented at the Nuclear Space and Radiation Effects Conference (NSREC) in 2007 [26]. Once the top-level requirements and technologies needed are defined, the RHA approach begins with evaluation of the radiation threats, their severity for the mission environment, and their effect on the required technologies. In the following stages, an iterative process of evaluating the radiation response of device performance (i.e., through testing and analysis) and developing mitigation strategies takes place [27]. As described in [26], testing, analysis and mitigation are time-consuming and expensive in terms of project resources, schedule and system performance. These expenses can be alleviated by means of a compact

modeling approach based on the simulation of radiation effects on devices and ICs, reducing the number of iterations required for testing analysis and mitigation activities.

The incorporation of radiation effects into “radiation-aware” compact models (i.e., mathematical descriptions of a semiconductor device that has been exposed to ionizing radiation [28]) is a challenging task that requires understanding of the physical mechanisms contributing to the buildup radiation-induced defects in advanced CMOS devices, and the effects of these defects on its electrical characteristics. Moreover, the mathematical formulation for the description of the radiation effects must remain suitable for use within a compact model without losing physical meaning and accuracy.

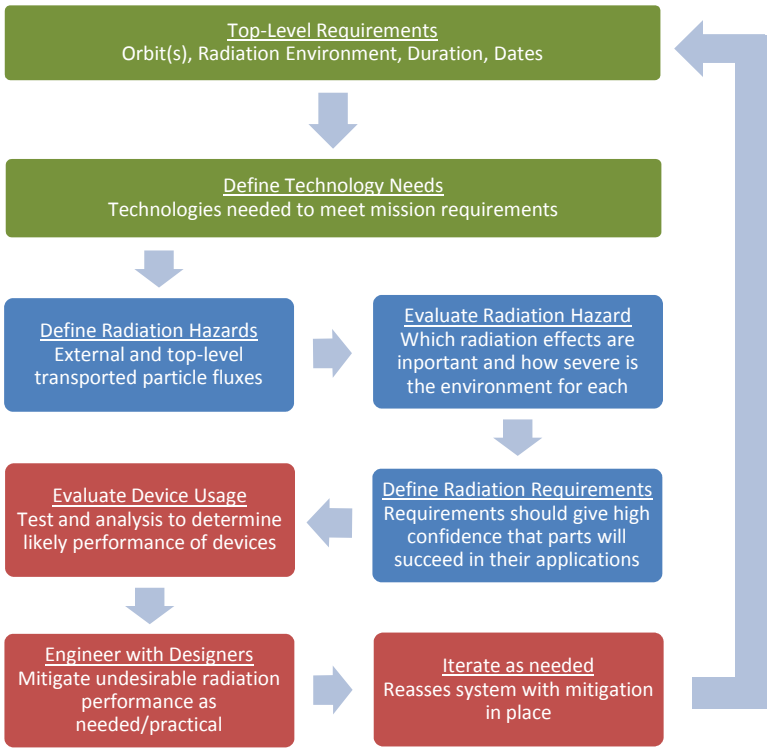

Fig. 1.2. Flow diagram describing NASA's approach to radiation hardness assurance (RHA) [26].

In this dissertation, a detailed study of the physical mechanisms contributing to the radiation-induced degradation of advanced CMOS devices is conducted experimentally and using numerical simulations to arrive at analytical models that describe buildup of defect densities (i.e., N_{ot} and N_{it}) in sensitive oxide regions. In order to determine the key mechanisms required to analytically model TID effects in advanced CMOS technologies, a physical model based kinetic equations for the buildup of radiation-induced defects in SiO_2 is presented. Numerical calculations for a one-dimensional (1-D) MOS system, obtained through a finite difference representation of the physical device, allow analytical models to be developed for

the basic mechanisms that describe TID effects in STI oxides. An approach for the incorporation of the analytical models into surface potential based compact models for field-oxide-field-effect-transistors (FOXFETs) and SOI transistors is also presented in this dissertation. Comparison with experimental data obtained from FOXFETs fabricated in a 90 nm low-standby power (LSP) commercial bulk CMOS technology and fully-depleted (FD) SOI n-channel transistors will provide verification of the presented approach for incorporating TID effects into surface potential based compact models.

1.2 Overview of Radiation Effects in MOS Devices

Shown in Fig. 1.3 is a schematic representation of the energy band diagram for an MOS structure with a positive bias applied at the gate [1]. The basic processes contributing to the time-dependent radiation response of MOS systems are also indicated in Fig. 1.3 and labeled (1)–(4). Processes (1)–(3) have to do with the generation, transport and trapping of holes within the SiO_2 film, and (4) has to do with the radiation-induced buildup of interface traps at the SiO_2-Si interface. The first two processes constitute what is referred to as the short-term response. At room temperature, the short-term response extends typically from picoseconds to the order of seconds and depends mostly on applied field, type of radiation, temperature and oxide thickness. Processes (3) and (4) make up the two components involved in the long-term radiation response of MOS systems. Long-term radiation effects are manifested through parametric shifts in MOS devices and can last for hours to years. A brief description of the different mechanisms

responsible for short-term and long-term radiation effects in the MOS system are presented below.

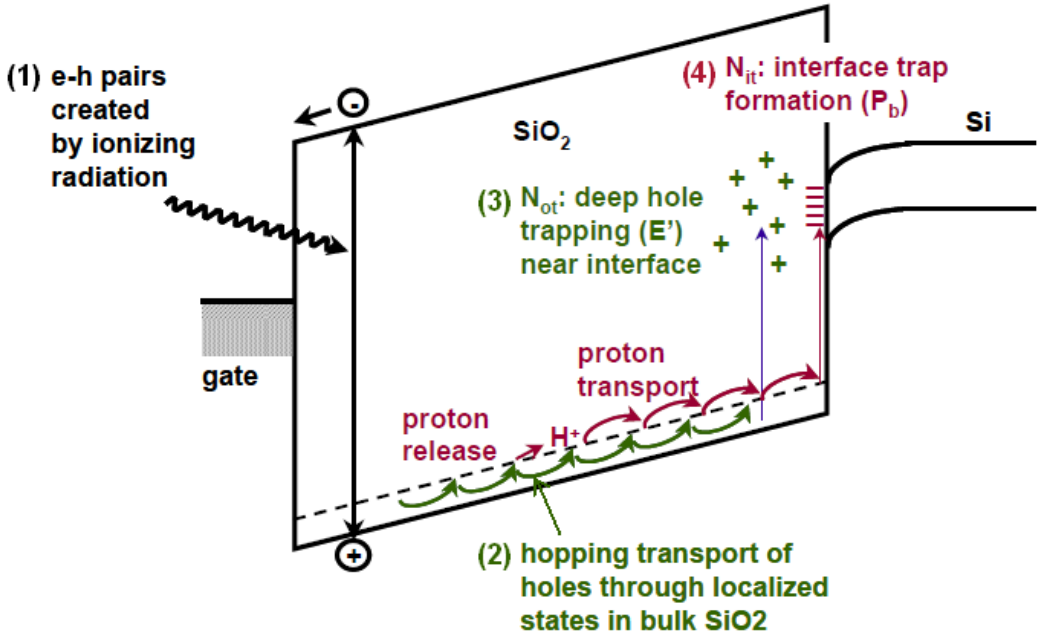

Fig. 1.3. Schematic energy band diagram for an MOS structure with a positive bias at the gate indicating the basic radiation-induced processes [1, 29].

As ionizing radiation passes through the SiO_2 film, energy is transferred from high energy photons and/or charged particles (e.g., protons, electrons, α-particles, energetic heavy ions) through direct and/or indirect ionization mechanisms, to generate electron-hole pairs (ehps). The amount of energy deposited by ionizing radiation is referred to as total ionizing dose (TID) and is defined as the absorbed energy per unit mass of a material. The SI unit for TID is the gray (1 Gy = 1 J/kg), however, the rad (radiation absorbed dose) is the conventional unit used in the radiation effects community (1 rad = 100 erg/g = 6.24×10^{13} eV/g = 1×10^{-2} Gy). The energy required to generate an electron/hole pair (i.e., the ionization energy,

E_p) in SiO_2 was first determined by McLean and Ausman to be 18 ± 3 eV [30]. Later, more accurate experiments by Benedetto and Boesch established that E_p = 17 ± 1 eV [31]. The density of ehps generated per unit dose of ionizing radiation is typically denoted by the conversion factor g_0 and is determined to be 8.1×10^{12} $cm^{-3}rad^{-1}$ (SiO_2). In general, g_0 can be obtained as a function of E_p and the density of the target material and is given by

$$g_0\left[\frac{\#\ \text{ehps}}{\text{cm}^3\cdot\text{rad}}\right] = 100\left[\frac{\text{erg}}{\text{g}}\right]\left[\frac{1}{\text{rad}}\right]\cdot\frac{1}{1.6\times10^{-12}}\left[\frac{\text{eV}}{\text{erg}}\right]\cdot\frac{1}{E_p}\left[\frac{\#\ \text{ehps}}{\text{eV}}\right]\cdot\rho\left[\frac{\text{g}}{\text{cm}^3}\right] \qquad (1.1)$$

The relationship between ionization energy, material density, and generated carriers are listed in Table 1.1 for GaAs, Si, and SiO_2, respectively [32].

TABLE 1.1
IONIZATION ENERGY AND CARRIER GENERATION FOR GIVEN MATERIAL

Material	E_p (eV)	Density (g/cm^3)	Pair density, g_0 ($ehps/cm^3\cdot rad$)
GaAs	~4.8	5.32	7.6×10^{12}
Silicon	3.6	2.328	4×10^{13}
Silicon Dioxide	17	2.2	8.1×10^{12}

Following the generation of ehps, as electrons and holes begin to transport within the oxide, some fraction will recombine, reducing the initial density of the free charged carriers. A very short time window is available for initial recombination processes to occur, since electrons, being much more mobile than holes, are very rapidly swept out of the oxide. The mobility of electrons in SiO_2 is approximately 20 $cm^2V^{-1}s^{-1}$ at room temperature [33], whereas for holes, the mobility is typically between 10^{-4} and 10^{-11} $cm^2V^{-1}s^{-1}$ depending on temperature

and field [34]. Holes are therefore relatively immobile in SiO_2, and the window available for initial recombination is determined by the time required for electrons to transport out of the oxide. For oxides with thicknesses of a few hundred nm and with a few volts applied (or even unbiased), this time window is in the order of picoseconds. Due to the time scale of the initial (or prompt) recombination processes, experiments are typically insensitive to the initial transient response (i.e., related to the transport of electrons) and can only characterize the late time response (i.e., related to the transport of holes) and long-term effects (i.e., as $t \rightarrow \infty$).

A fraction of holes that escape initial recombination (i.e., the hole fractional yield) will slowly travel towards the SiO_2-Si interface resulting in long-term TID effects. As will be described in Chapter 2, transporting holes induce internal space-charge fields that will also have an effect on the transient and dose-rate response. Hole fractional yield (f_y) is strongly dependent on the magnitude of the oxide electric field acting upon the generated charge pairs. A higher field will tend to rapidly separate electrons and hole and therefore suppress recombination. Another factor that determines f_y is the mean separation between the generated ehps, which is inversely proportional to the electronic stopping power of the ionizing radiation, and is therefore a function of the incident particle type and energy [35]. Shown in Fig. 1.4 is a plot of the hole fractional yield as a function of the electric field for several types of radiation incident on SiO_2 [1]. This plot summarizes experimental results from several studies [31, 36-41]. Electronic stopping power measures the amount of energy transferred from an incident

particle to a material per unit of track length (dE/dx) and is typically expressed in units of keV/μm. dE/dx can also be expressed in terms of its linear energy transfer (LET) in units of eV/g/cm^2. Shown in Fig. 1.5 is a plot of the LET in SiO_2 vs. particle energy for electrons, protons, and secondary electrons from 10-keV X-rays and 1.25-MeV ^{60}Co gamma rays [42].

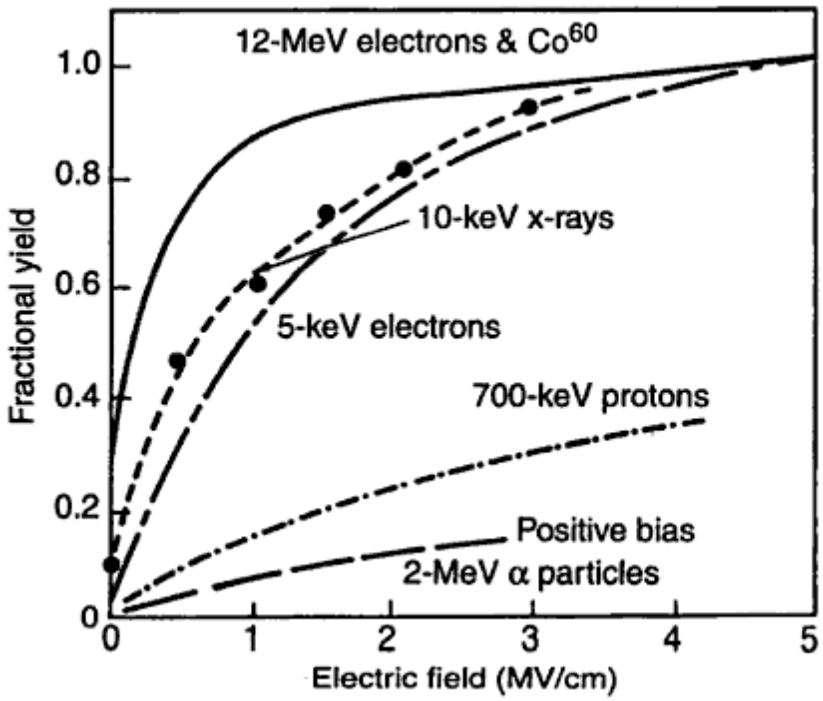

Fig. 1.4. Fractional yield as a function of electric field for different kinds of radiation incident on SiO_2 [1].

Hole yield can be successfully described analytically in thermally grown SiO_2 using initial recombination models that were originally developed for gases exposed to ionizing radiation. The basic models that describe the limiting cases are: 1) the columnar model for the case where the mean separation between the

generated ehps is much smaller than the thermalization distance (i.e., the initial separation between an electron and a hole of the same pair after reaching thermal equilibrium energies); 2) the geminate model for the case when the mean separation between the generated ehps is much larger than the thermalization distance. For SiO_2, the thermalization distance is approximately 8 nm [30]. The mean separation between generated ehps is given by the inverse of the electron/hole pair line density, which can be calculated from the LET of the incident particle. For low-LET particles (e.g., high-energy electrons and secondary Compton electrons from ^{60}Co gamma interactions), electron/hole pair line density is low since they generate a sparse density of ehps with a mean distance of separation much larger than the thermalization distance. In this case, the geminate model is appropriate for describing initial recombination. In fact, for particles with an LET below ~ 9 MeV/g/cm^2 one can typically use the geminate model as indicated by the shaded region below the lower dotted line in Fig. 1.5. On the other hand, radiation from particles with a high-LET (e.g., 700-keV protons, 2-MeV α particles) results in a high electron/hole pair line density where the mean distance of separation between ehps is much lower than the thermalization distance, and therefore, the columnar model applies. As indicated in Fig. 1.5, the columnar model is appropriate for particles with an LET higher than ~ 90 MeV/g/cm^2. The results summarized in Fig. 1.4 show that for particles with a low LET, recombination is relatively weak process, and therefore hole fractional yield is high. For example, at an electric field of 1 MV/cm, the fractional yield is approximately 90% for the case of 12-MeV electrons and ^{60}Co

gamma rays. In contrast, for highly ionizing particles (i.e., particles with a high LET), recombination is a strong process and hole fractional yield is low. At an electric field of 1 MV/cm, hole yield is around 10% for the case of 700-keV protons and 2-MeV α particles.

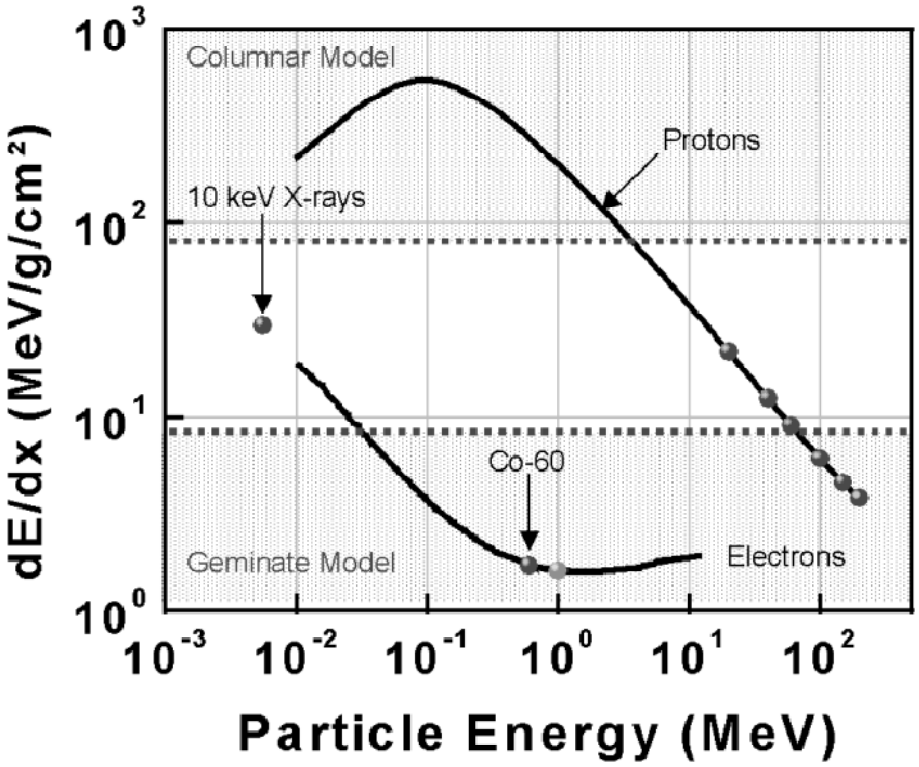

Fig. 1.5. Linear Energy Transfer (LET) in SiO_2 vs. particle energy for electrons, protons, and secondary electrons from 10-keV X-rays and 1.25-MeV ^{60}Co gamma rays [42].

Radiation-induced generation and prompt recombination of ehps constitute the first basic process contributing to the time-dependent radiation response of MOS systems indicated in Fig. 1.3. As mentioned above, together with the second basic process, i.e., transport of holes through the SiO_2 layer, generation and prompt recombination of ehps make up the short-term radiation response of MOS

systems. Extensive studies of hole transport in amorphous SiO_2 have revealed unusual properties that will be summarized in the remainder of this section. As described in [1], a major motivating factor for these studies was the recognition early on that the short-term transient response of MOS systems following pulsed irradiation is dominated by hole transport through the SiO_2 film. Typically, hole transport in SiO_2 has been characterized experimentally by exposing the MOS samples to a short pulse of radiation and observing the post-irradiation response as a function of time. The post-irradiation response is monitored through the recovery of parametric shifts, i.e., flatband voltage shifts (ΔV_{fb}) in MOS capacitors or threshold voltage shifts (ΔV_t) in MOSFETs, as a function of time and for different conditions (e.g., temperature, field, thickness). Representative experimental data sets that emphasize different properties of hole transport in SiO_2 and the effects of temperature, field and thickness can be found in the published works of Boesch *et al*. [43, 44] and McLean *et al*. [45, 46]. These studies have shown that while electrons are rapidly swept out of the SiO_2 layer, the transport of holes is much slower and is highly dispersive in time. This means that hole transport through SiO_2 takes place over many decades of time and can extend typically up to an order of seconds at room temperature [35]. These studies have also demonstrated the universality of hole transport, i.e., the fact that temperature, field and thickness only affect the time scale for transport but not the amount of dispersion [45]. This feature establishes that when a measured parameter (e.g., ΔV_{fb}) is plotted in time units normalized to a characteristic recovery time (e.g., half-recovery time), the data for different conditions of

temperature, electric field and oxide thickness will trace out the same universal curve. Other important features are that the hole transit time possess Arrhenius-type temperature activation dependence above ~140 K, but becomes thermally nonactivated below ~140K, and that it has a strong superlinear power law dependence on oxide thickness [43].

Most of the hole transport properties discussed above can be attributed to the broad distribution of transit times of individual holes within the oxide. The reason for such a broad distribution can be understood by considering two kinds of microscopic hole transport mechanisms: a) transport via valence band conduction intervened by multiple trapping and de-trapping events, where small differences in energy levels lead to a wide distribution for the de-trapping time; and b) random hopping transport via tunneling between localized states, where fluctuations in hopping distance or activation energy can lead to a large variation in hopping times. Both of these transport mechanisms would result in the aforementioned broad distribution of transit times for individual holes and are illustrated schematically in Fig. 1.6. As described in [1], these transport mechanisms can be treated within the framework of the generalized continuous-time random walk (CTRW) model. The CTRW model, was originally developed by Montroll *et al*. [47] and applied to hole transport in SiO_2 by McLean *et al*. [34, 43, 48, 49] and Hughes *et al*. [50, 51]. The idea behind the model is that a hole transit-dependent response (e.g. ΔV_{fb}) can be characterized by a function $f(\alpha, t/t_s)$, where α is a disorder parameter that describes the amount of dispersion, but is independent of temperature (T), oxide electric field (E_{ox}) and thickness (t_{ox}). These

parameters enter only on the characteristic time scale of $t_s = f(T, E_{ox}, t_{ox})$. Further details of the CTRW model, its application to hole transport in SiO_2, and comparison with experimental data can be found in [45].

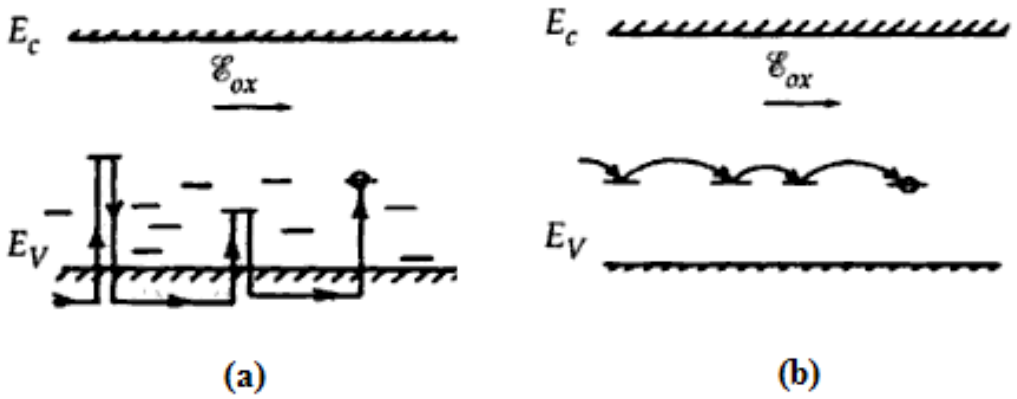

Fig. 1.6. Hole transport mechanisms: (a) trap-modulated transport via valence band conduction and (b) hopping transport via tunneling between localized states [35].

Following the short-term radiation response processes discussed above, the MOS system typically exhibits residual long-term detrimental effects as a result of hole trapping (and annealing) near the Si-SiO_2 interface and the generation of interface states at the Si-SiO_2 interface. These are processes (3) and (4) indicated in Fig. 1.3. As holes transport towards the Si-SiO_2 interface, a fraction will be trapped in deep energy-level sites located near the Si-SiO_2 interface. Several studies [20, 29, 35, 52-54] have confirmed that the dominant defect responsible for deep-level hole trapping in amorphous SiO_2 are oxygen vacancies located in the strained transition region where excess Si exists due to incomplete oxidation during fabrication. An oxygen vacancy is typically formed when two Si atoms are

joined by a weak strained Si-Si bond and each is also back bonded to three oxygen atoms. Lenahan and Dressendorfer were able to correlate radiation-induced oxide trapped charge with an E_γ' center signal using electron spin resonance (ESR) characterization [54].

The E_γ' center is formed by the capture of a hole at the Si-Si bond. When the positive charge is captured, the Si-Si bond is broken and the lattice relaxes asymmetrically as described by Feigl *et al*. [55]. In the asymmetric relaxation of the lattice, the positively charged Si relaxes away from vacancy and into a planar configuration, while the neutral Si relaxes towards the vacancy. The formation of an E_γ' center (i.e., the hole trapping mechanism) is illustrated in Fig. 1.7. As shown here, the E_γ' complex consists of a positively charged trivalent Si atom bonded to three oxygen atoms and a neutral trivalent Si atom bonded to three oxygen atoms and having an unpaired spin electron. It is important to notice that ESR studies done by Lenahan *et al*. have not determined that any other defects in SiO_2 play a measurable role in long-term hole trapping. However, other oxygen vacancies that result in shallow energy-level states are associated with the temporal dispersion of hole transport in SiO_2 [56].

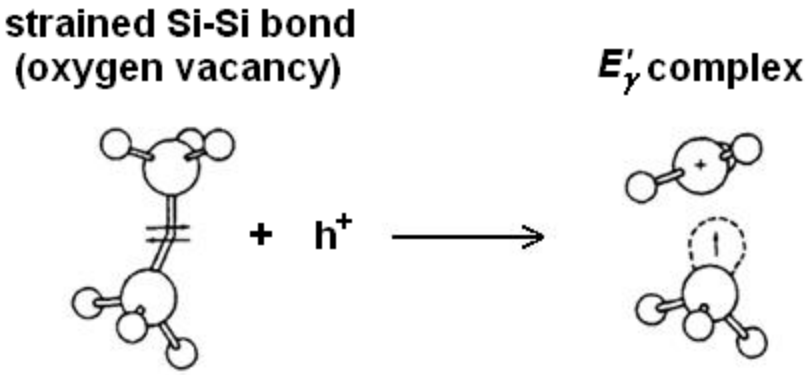

Fig. 1.7. Model for hole trapping and de-trapping (annealing) and formation of E'_γ complex [35].

The annealing/compensation of radiation-induced trapped holes in SiO_2 is a long-term process that is strongly dependent on temperature and applied electric field. The basic mechanisms for electron compensation are tunneling of an electron from the Si substrate and compensation by thermal excitation of an electron from the valence band [35]. Both tunneling and thermal emission have been combined into a single model by McWhorter *et al*. that describes a tunneling front and a thermal emission front, where the position of both varies logarithmically with time [57]. In other words, the distance into the oxide bulk from where trapped holes can be removed, measured from either the Si-SiO_2 interface for the case of tunneling or from the valence band edge for thermal emission, varies as ln(*t*). Hole trapping along with the annealing/compensation processes are illustrated in Fig. 1.8. As shown in Fig. 1.8, the trapped positive charge can be neutralized by adding an electron to the relaxed E'_γ center. The

added electron will eliminate the unpaired spin and therefore compensate for the positive charge by creating a dipole structure as described in Fig. 1.7 by the transition from (b) → (c). The electron compensation process is reversible as illustrated in Fig. 1.7 by the transition from (c) → (b), where the electron has tunneled back into the substrate. True annealing can occur when the electrostatic force between the two ends of the dipole structure in Fig. 1.7(c) is sufficient to reform the Si-Si bond. This situation is indicated by the transition from (c) → (a) in Fig 1.7 [35].

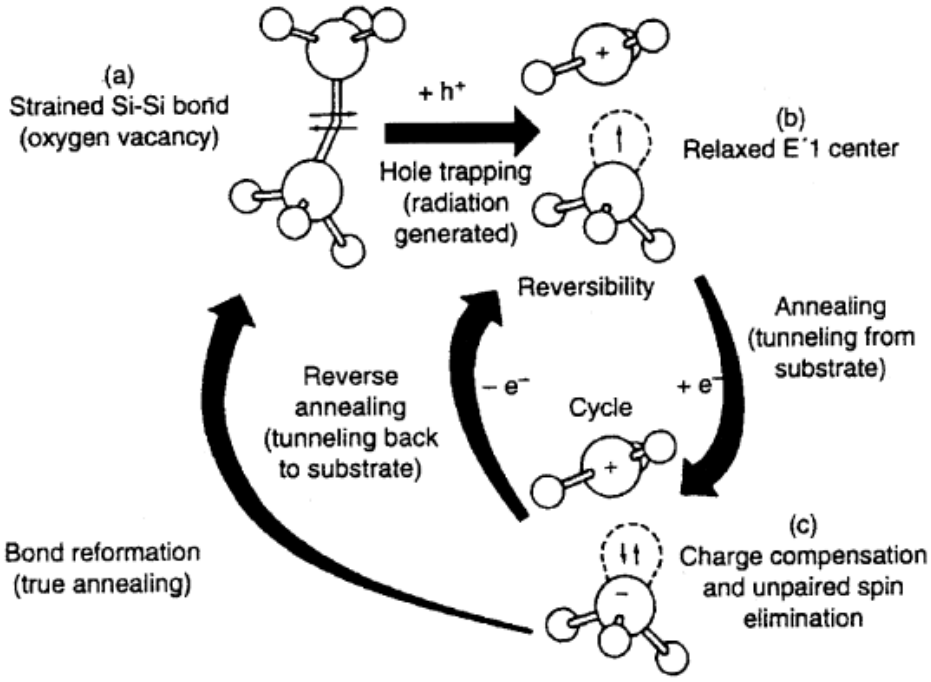

Fig. 1.8. Model for hole trapping and de-trapping (annealing) and for intermediate electron compensation and reverse annealing phenomenon [35].

The second component of the long-term response of MOS systems is the generation of interface traps at the Si-SiO_2 interface. Unlike trapped holes, which are “fixed” and positive, interface traps are localized and electrically active states

with energy levels within the Si bandgap that can exchange charge with the silicon bulk. Their occupancy is determined by the position of the Fermi level at the interface, and therefore, the charge state of interface traps is determined by the surface potential. As discussed in [35], there are three classes of models that have been proposed for the formation of interface states. The first class is the two-stage model presented by McLean [58]. In the first stage, radiation-generated holes release protons (H^+) in the SiO_2 bulk as they transport through the oxide. In the second stage, protons transport towards the interface where they react to form interface traps. The release and transport of protons and the formation of interface traps at the Si-SiO_2 interface are illustrated in Fig. 1.3, and indicated as the 4^{th} basic process contributing to the time-dependent radiation response of MOS systems. In the two-stage model, the dispersive transport of protons towards the interface determines the rate of interface trap formation. A second class of models suggests that diffusion of neutral hydrogen plays an important role in the formation of interface traps. In [59], Brown presents chemical kinetic equations that describe the diffusion of molecular hydrogen in SiO_2 in order to determine the time dependence of post-irradiation interface trap buildup. This model is an extension of the model originally presented by Griscom [60]. A third class of models assumes that the breaking of strained Si-O-Si bonds as a result of hole trapping near the interface plays a key role in the formation of interface traps as the released mobile non-bridging oxygen propagates to the interface where it reacts to form an interface state [61, 62].

The time, temperature and field dependence of interface trap generation processes have been investigated experimentally through electrical characterization of irradiated MOS samples. Many of the experimental studies have confirmed that the largest effect accounting for ~ 90% of the total interface trap buildup is the two-stage process described in the McLean model [34, 46, 63-65]. However, other processes have been determined to account for smaller parts of the total buildup of interface traps. One of these processes is related to a relatively fast field-dependent effect that correlates in orders of magnitude in time with the initial generation of interface states [66, 67]. Another is a diffusion process of a neutral species that accounts for the formation of interface traps with no field polarity dependence [66]. Using ESR techniques, Lenahan *et al*. [54, 68] were able to correlate radiation-induced interface states with the P_{b0} center in (111) Si. The microscopic nature of the P_{b0} center was originally identified in (111) Si by Caplan *et al*. [69] as a trivalent Si bonded to three other Si atoms at the interface and having a dangling bond extending into the oxide and normal to the surface. Poindexter *et al*. [70] observed two P_b centers (i.e., P_{b0} and P_{b1}) in (100) Si and identified the P_{b1} center as a trivalent Si bonded to two Si atoms and to one oxygen atom with a dangling bond extending into the oxide at an angle. However, previous studies have determined that the buildup of radiation-induced interface traps consists entirely of P_{b0} centers [71], and that the P_{b1} centers are electrically inactive [72]. Shown in Fig. 1.9 are schematic diagrams of the P_b centers in the (111) and (100) Si-SiO_2 interface. Fig. 1.10 plots the experimental

results by Lenahan *et al*. showing the correlation of the P_{b0} center in (111) Si with the radiation-induced interface trap density [68].

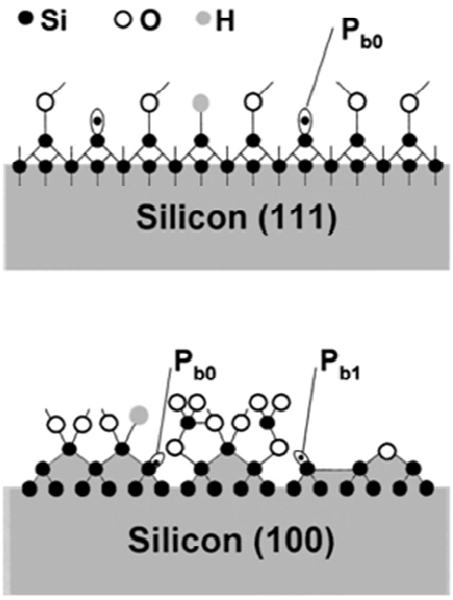

Fig. 1.9. Schematic diagram of Si-SiO_2 interface showing P_{b0} and P_{b1} centers [73].

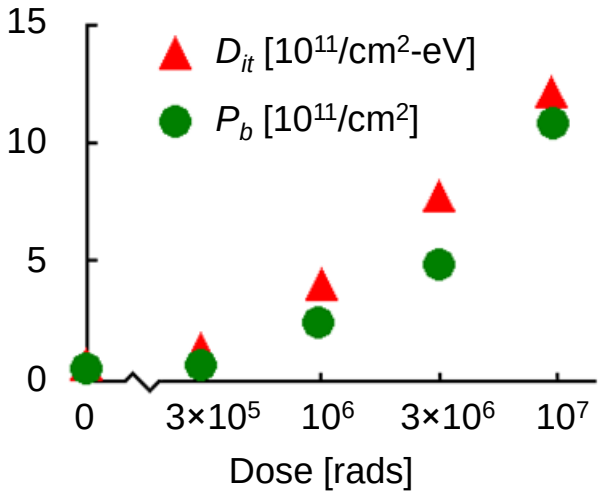

Fig. 1.10. experimental results by Lenahan et al. showing the correlation of the P_{b0} center in (111) Si with the radiation-induced interface trap density [68].

1.3 TID Effects in Deep-Submicron CMOS Technologies

For technologies with sub-micron and deep-submicron critical dimensions, radiation damage is assumed to occur primarily in the isolating field oxides. This is due to the reduction of classical radiation threats (i.e., buildup of fixed oxide charge in the gate oxides) that to first order scale with t_{ox}. By contrast, the buildup of N_{ot} and N_{it} near the thicker semiconductor-isolation oxide interface presents a much greater radiation threat [16-20] and has a measurable impact on key IC specifications [21, 22, 74]. Therefore, the radiation response of these technologies most often depends on the structural features and the processing of the isolation oxides. Typical STI oxide processing involves etching a trench pattern through a nitride layer, sidewall oxidation to grow a thin oxide liner, chemical vapor deposition to fill the trench and chemical-mechanical planarization polishing [75]. However, unlike gate oxide processing, fabrication conditions for isolation oxides are typically not as tightly controlled. Thus, the trapping properties of STI oxides can be significantly different than for gate oxides, with large variations observed between processes. Even thermally grown field oxides have been shown to have a qualitatively different radiation response than gate oxides [76].

Fig. 1.11 shows the cross-sectional diagrams of n-channel MOSFETs with (a) LOCOS isolation and (b) STI. In Fig. 1.11, the radiation-induced charge buildup is indicated with the "+" symbol. For the case of LOCOS isolation, charge buildup occurs at the bird's beak region and along the base of the field oxide (extending from drain to source where the gate overlaps the thick field oxide). In STI oxides, radiation-induced charge will build up near the trench

corner and along the base of the field oxide. In most deep-submicron technologies, LOCOS isolation has been replaced with STI and therefore radiation damage to STI oxides will be the primary focus in this dissertation.

The primary effect of field oxide charging is the creation of leakage paths that result in the degradation of device performance and IC functionality. The possible leakage paths that are typically associated with defect buildup along the base and sidewalls of field oxides are indicated on the layout of two inverters in parallel shown in Fig. 1.12. These are indicated as: (1) leakage between drain and source of an n-channel transistor, (2) leakage between the n^+ drain/source regions of different n-channel devices, (3) leakage between an n-well of a p-channel device and the n^+ drain/source region of a nearby n-channel device, and (4) leakage between the n-well regions of two isolated p-channel devices.

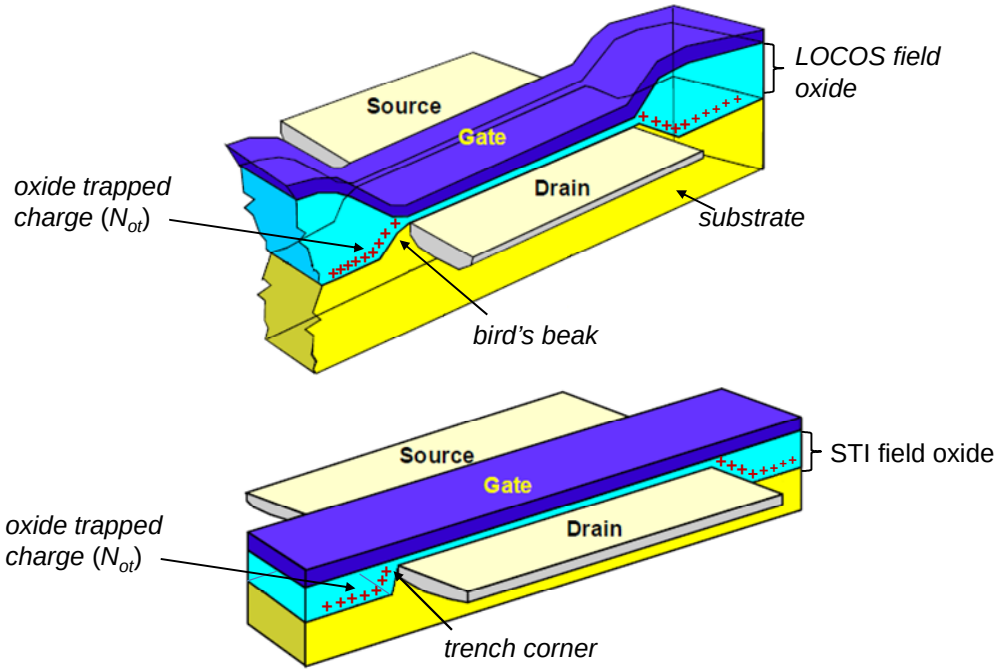

Fig. 1.11. Cross-sectional diagrams of n-channel MOSFETs with (a) LOCOS isolation and (b) STI [29, 77].

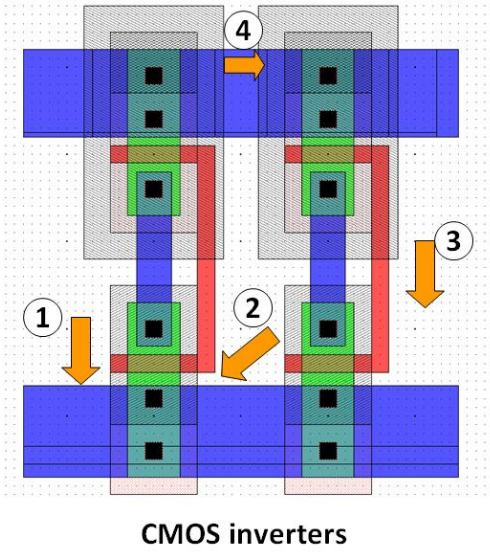

Fig. 1.12. Layout of two inverters in parallel showing possible leakage paths associated with defect buildup along the base and sidewalls of field oxides [35].

Drain-to-source leakage is also referred to as edge leakage or intra-device leakage and is typically associated with the buildup of radiation-induced defects along the sidewall of the field oxides. This kind of leakage can typically be characterized by measuring the radiation-induced degradation of the *I-V* characteristics for a specific n-channel transistor. Leakage that occurs between two separate devices (i.e. leakage paths 2, 3 and 4 in Fig. 1.12) is also known as under leakage or inter-device leakage and is typically associated with the buildup of radiation-induced defects along the base of the field oxides (i.e., the bottom of the trench). Characterizing inter-device leakage requires specially designed test structures such as the FOXFETs or field-oxide capacitors (FOXCAPs). Shown in Fig. 1.13 is a cross-sectional diagram indicating drain-to-source and leakage (l) and leakage between the n+ source/drain region of an n-channel device and the n-well region of an adjacent p-channel device (2).

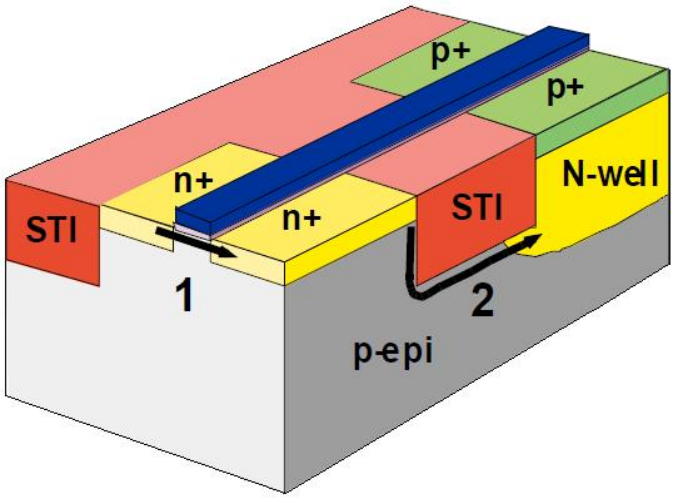

Fig. 1.13. Cross-sectional diagram indicating: (1) drain-to-source leakage and (2) leakage between the n+ source/drain region of an n-channel device and the n-well region of an adjacent p-channel device [29, 77].

1.4 Goals and Approach

This dissertation is divided into six chapters containing several topics related to the modeling of TID effects in advanced CMOS technologies. The topics discussed in this dissertation comprise different levels of modeling, ranging from the basic physical mechanism of radiation damage in MOS structures to surface-potential-based compact modeling techniques for advanced bulk and SOI CMOS technologies. The main focus of this dissertation is to provide a comprehensive study of the physical mechanisms contributing to the buildup of N_{ot} and N_{it} in advanced CMOS technologies; determining the key mechanisms required to model the dependence of the buildup on external conditions (e.g., dose-rate, bias); and formulating analytical models that are suitable for incorporation into advanced surface-potential-based compact models of modern CMOS devices. Whereas Chapter 1 has provided background information and an overview of radiation effects in MOS technologies, the remaining chapters present a detailed description of modeling techniques for advanced CMOS devices.

Chapter 2 focuses on the basic mechanisms of TID effects in advanced CMOS technologies. This chapter reviews a selection of experimental data from several published works characterizing the physical mechanisms contributing to radiation effects in CMOS technologies. A theoretical perspective for key reactions leading to the buildup of radiation-induced defects (N_{ot} and N_{it}) in STI oxides is presented in this chapter. A set of reactions is formulated into a physical model that describes the time-dependent effects of ionizing radiation in the oxide regions of CMOS devices.

In Chapter 3, experimental data from FOXFETs and MOS capacitors are presented. The FOXFETs are uniquely designed to characterize defect buildup and the general susceptibility of STI oxides to ionizing radiation. These devices are fabricated in a low-standby power (LSP) high performance 90 nm commercial bulk CMOS technology. The time-dependent radiation response of these devices is characterized by step stress irradiations and room temperature anneals for different dose-rates and biasing conditions. MOS capacitors with 200 nm thermal oxides grown on n-type Si wafers and Al gate contacts are fabricated at Arizona State University. These devices allow characterizing TID and dose-rate effects in thermally grown SiO_2 and support parameterization of the radiation response model.

In Chapter 4, numerical calculations for the time-dependent buildup of N_{ot} and N_{it} are obtained through a finite difference representation of the physical model. These calculations provide insight on key factors that determine total dose and dose rate effects in STI oxides. Comparison with experimental data allow investigating the different mechanisms that impact the time-dependent buildup of N_{ot} and N_{it} in STI oxides of advance CMOS technologies. The influence of parameters that affect the radiation response of STI oxides such as applied bias, dose-rate and non-uniform distribution of trapping precursors (i.e., processing defects) is quantified through numerical simulations. Analytical descriptions for the buildup of N_{ot} and N_{it} are also presented in Chapter 4. The time-dependent buildup of N_{ot} and N_{it} are analytically calculated using general equations that describe the generation, transport and trapping of holes as well as the reaction of

holes with hydrogen source sites resulting in the release of protons and subsequent formation of interface traps. The analytical models are validated against technological parameters such as doping concentration and oxide thickness by comparison with numerical calculation and experimental data. When used in conjunction with closed-form expressions for surface potential, the analytical models enable an accurate description of radiation-induced degradation of transistor electrical characteristics allowing the incorporation of TID effects into surface potential based compact models.

Chapter 5 describes the incorporation of TID effects into surface-potential-based compact models for advanced CMOS technologies. The incorporation is accomplished through modifications of the surface potential equations (SPE), allowing for the inclusion of radiation-induced defects (i.e., N_{ot} and N_{it}) into the calculations of surface potential. Verification of the compact modeling approach is achieved via comparisons to experimental data on degraded current-voltage (*I-V*) characteristics and to degradation parameters, such as threshold voltage shifts, increased off-state leakage current and changes in the subthreshold swing in bulk and SOI CMOS transistors.

The final chapter summarizes the dissertation, discusses my contributions, and suggests future work.

CHAPTER 2. MECHANISMS OF RADIATION EFFECTS IN CMOS DEVICES

2.1 Ionizing Radiation Damage in Deep-Submicron CMOS Technologies

The susceptibility to ionizing radiation of most deep-submicron CMOS technologies has been reduced due to aggressive semiconductor device scaling. The amount of charge that can be trapped in an oxide layer is proportional to the oxide volume and therefore scales with t_{ox} [19]. Moreover, a sharp decrease in the radiation-induced defect buildup is observed for thicknesses below 7 – 10 nm due to tunneling mechanisms. This effect was first investigated by Saks *et al*. [78, 79] who observed that the rate of defect buildup in thin oxides was much smaller than what would be extrapolated from thicker oxides. Since for most deep-submicron technologies the gate oxide thickness is less than 7 nm, degradation in the thin gate dielectrics is unlikely to have an impact in the radiation response. STI oxides in deep-submicron technologies, by contrast, have thicknesses typically between 290 – 450 nm regardless of the technology generation. Therefore, the shallow trench isolation oxides are significantly more susceptible to radiation damage than gate oxides for advanced CMOS technologies [16, 18, 19, 77, 80, 81].

Early studies on the ionizing radiation response of STI oxides determined that TID susceptibility in 0.5 µm and 0.35 µm CMOS technologies was comparable to older technologies with LOCOS isolation [77, 82]. In [77], Shaneyfelt *et al*. determined that hardening STI was in fact more complex than using a traditional hardened oxide as the trench dielectric. In both of these studies, leakage at the trench corner was noted as a significant contributor to the radiation-

induced increase in off-state leakage (ΔI_{off}). A later study by Johnston *et al*. [83] discussed the importance of the trench structural details and particularly the rounding of the trench corner on the radiation response. Sharp corners result in a localized reduction in gate oxide thickness and ensuing "corner leakage" or a "hump" in the subthreshold *I-V* characteristics. Johnston *et al*. explain that technologies used in earlier studies had sharper trench corners and thicker gate oxides causing radiation-induced leakage in the trench corner to be the dominant mechanism. A trend in commercial CMOS processes towards higher total dose hardness was pointed out by Lacoe in [19]. Several factors such as scaling of the gate oxide, increased doping concentrations, advances in STI processing, and reduced supply voltage can be attributed to the increase in total dose hardness.

Shown in Fig. 2.1 are extractions for ΔI_{off} as a function of dose obtained from the degraded I_d-V_{gs} characteristics of minimum geometry n-channel transistor from the 0.35 µm, 0.25 µm and 0.18 µm TSMC processes after exposure to various levels of total ionizing dose [84-86]. All devices were exposed to ^{60}Co gamma rays under the same conditions and biased at the corresponding supply voltages. The supply voltages as well as other relevant technology characteristics are listed in Table 2.1. Since t_{ox} is less than or equal to 7 nm for all three processes, degradation from exposure to ionizing radiation is assumed to occur mainly in the field oxides. This is the case for all deep-submicron technologies considered in this dissertation. As shown in Fig. 2.1, I_{off} begins to increase at a lower dose for the 0.35 µm process with LOCOS isolation than for processes with STI oxides. Also, the rate of ΔI_{off} appears to be higher for the TSMC 0.35 µm

process. For the 0.25 µm and 0.18 µm processes, the rate of ΔI_{off} appears to be similar, but the increase begins at a lower dose level for the 0.25 µm process. Recent studies of the radiation-induced degradation of STI oxides in commercial technologies with deep-submicron critical dimensions (i.e., 130 nm and 90 nm) have shown much higher immunity to TID effects. For these technologies, less than an order of magnitude increase in I_{off} was measured up to 1 Mrad(SiO_2) of total dose [84, 87]. Although, in [87], McLain *et al*. determined enhanced susceptibility of I/O devices for a 90 nm commercial bulk CMOS technology.

TABLE 2.1
RELEVANT CHARACTERISTICS FOR TECHNOLOGIES CONSIDERED IN FIG. 2.1

Technology	t_{ox} (nm)	Isolation	Supply Voltage (V)
TSMC 0.35 µm	7.0	LOCOS	3.3
TSMC 0.25 µm	5.8	STI	2.5
TSMC 0.15 µm	3.2	STI	1.8

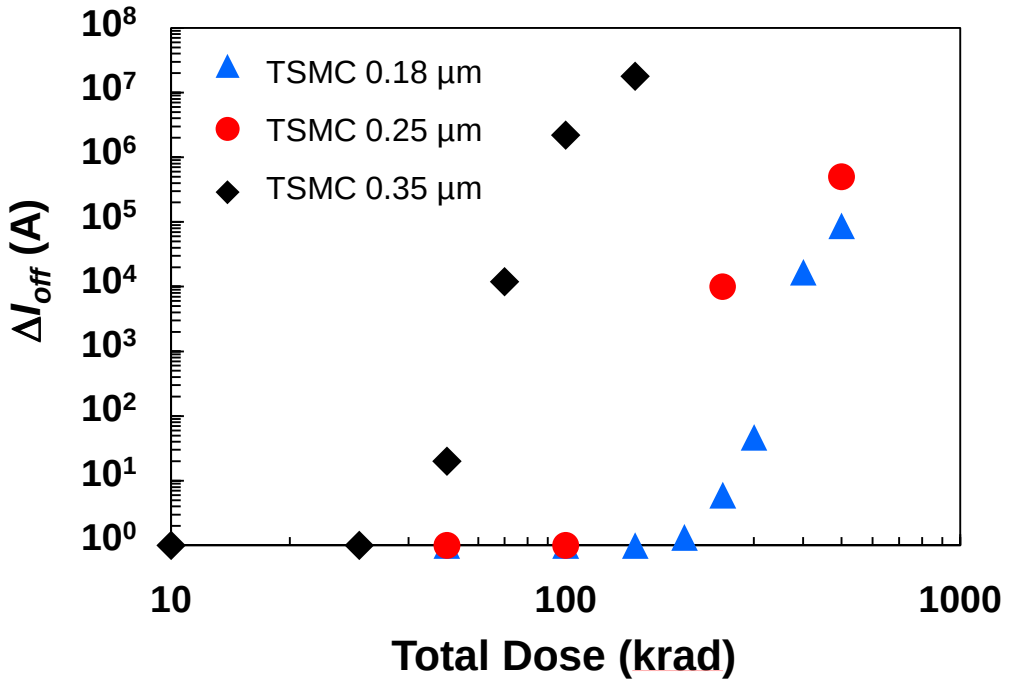

Fig. 2.1. ΔI_{off} as a function of dose obtained from the degraded I_d-V_{gs} characteristics of minimum geometry n-channel transistor from the 0.35 µm, 0.25 µm and 0.18 µm TSMC processes after exposure to various levels of total ionizing dose [84-86].

The strong dependence of ΔI_{off} on applied bias during irradiation is demonstrated in the plot of I_{off} vs. dose shown in Fig. 2.2 for devices under different bias conditions [83]. These results are for n-channel transistors from a 0.18 µm process exposed to ^{60}Co at doses between 50 and 100 rad(Si)/sec. The results in Fig. 2.2 indicate that for a gate-to-source bias (V_{gs}) of 0 volts during irradiation, the amount of charge trapping near trench corner is negligible as evident from the small change in I_{off} up to 300 krad(SiO_2). Increasing V_{gs} results in an increase in the slope of I_{off} vs. total dose curve, and a shift to lower total dose levels. In [83], Johnston *et al*. discuss the effects of non-uniformities (i.e., in

electric field and transport path lengths) on the spatial distribution of charge buildup along the sidewall of the STI. The three processes that contribute to the non-uniform distribution of charge buildup are: (1) charge yield, (2) charge transport by drift and diffusion and (3) hole trapping at the Si-STI interface (i.e., at the trench sidewall).

MOS structures with STI oxides as the intermediate dielectric (e.g., FOXFETs and FOXCAPs) can be used to investigate the buildup of radiation-induced defect densities without the non-uniform effects that accompany the irregular sidewall structures. Although these test structures will not provide information on the sidewall charge distribution that is critical in modeling edge leakage in regular n-channel transistors, they allow investigating the defect buildup along the base of the STI oxides. The non-uniformities of the trench sidewall and corner have a negligible effect on the electrical characteristics of these devices. Therefore, for FOXFETs and FOXCAPs it is possible to analyze the basic mechanisms that contribute to the time-dependent buildup of radiation-induced defects in STI oxides without the complexities introduced by these non-uniformities and to readily extract their densities (i.e., N_{ot} and N_{it}).

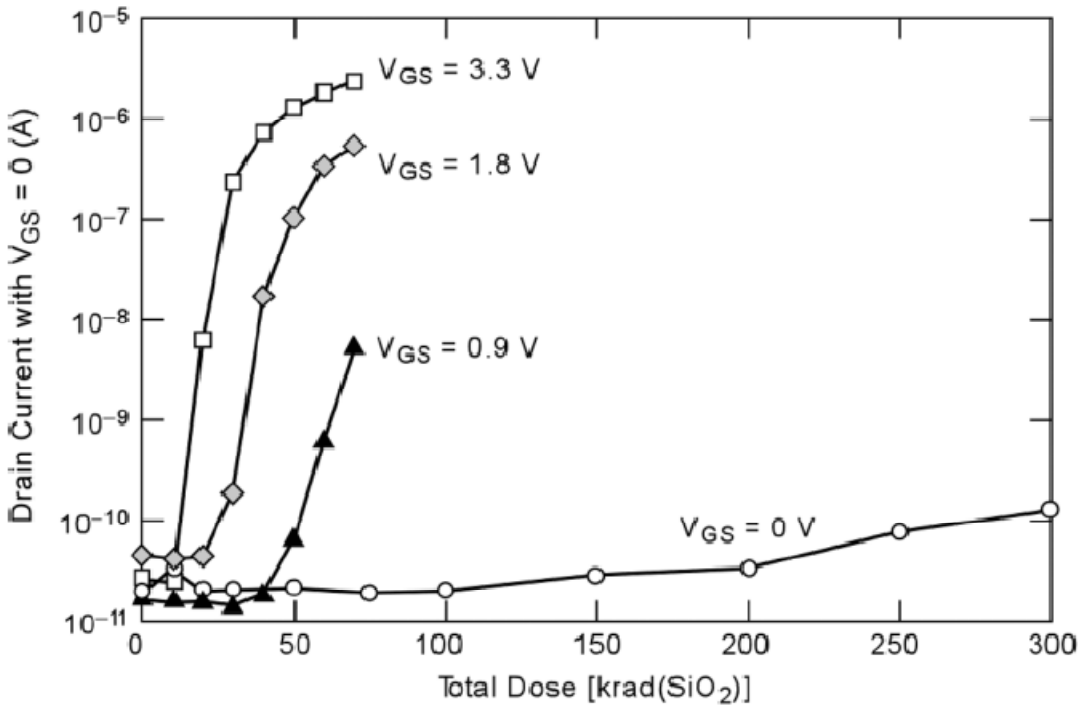

Fig. 2.2. I_{off} vs. dose for n-channel transistors from a 180 nm process exposed to ^{60}Co at doses between 50 and 100 rad(Si)/sec under different bias conditions [83].

Shown in Fig. 2.3 are extractions of shifts in threshold voltage (ΔV_{th}) plotted as a function of dose obtained from the degraded I_d-V_{gs} characteristics of FOXFET devices fabricated in TSMC 0.35 µm and TSMC 0.25 µm processes after exposure to different levels of total ionizing dose up to 100 krad(SiO_2) [85, 86]. The increase in ΔV_{th} as a function of dose indicates large densities of trapped charge in regions near the base of the STI and LOCOS field oxides. The results in Fig. 2.3 reveal a comparable increase in radiation-induced defect density as a function of dose as evident from the similarities in the values of ΔV_{th} for both processes. Since the 0.35 µm process has LOCOS isolation and the 0.25 µm process has STI, these results indicate that the mechanisms contributing to the

buildup rate of radiation-induced defects might be similar for both types of field oxides. Thus, the greater degradation in the regular n-channel transistors from the 0.35 µm process (as described by the greater increase in off-state leakage at lower dose levels plotted in Fig. 2.1) might be due to differences in the structural details of LOCOS and STI oxides particularly in the transition from thin gate oxide to thick field oxides (i.e., the bird's beak region).

Evidence of interface trap buildup at the Si-SiO_2 interface in the base of STI oxides is obtained from the degradation of the I_d-V_{gs} characteristics of FOXFET devices fabricated in a 0.18 µm CMOS image sensor process shown in Fig. 2.4 [88]. In these measurements, the decrease in subthreshold slope with increasing total dose indicates the buildup of interface traps as a function of dose. In a different study, Faccio *et al*. [89] investigated the radiation response of FOXFETs fabricated in a commercial 0.13 µm CMOS technology observing a similar response. Using charge pumping techniques, Faccio *et al*. determined that most radiation-induced switching states are interface traps rather than slower near interfacial switching states often referred to as "border traps" or "switching" oxide traps [89].

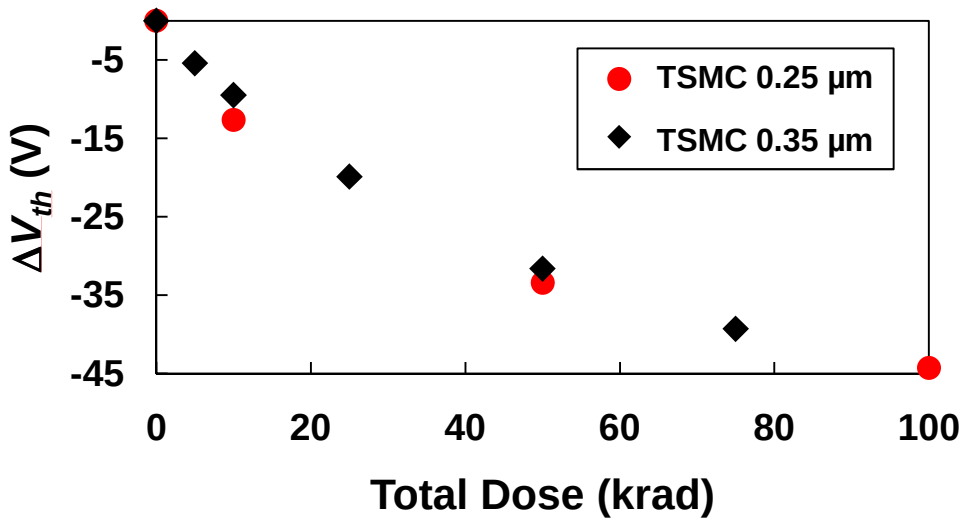

Fig. 2.3. Extractions threshold voltage shifts (ΔV_{th}) as a function of dose obtained from the degraded I_d-V_{gs} characteristics of FOXFET devices fabricated in TSMC 0.35 µm and TSMC 0.25 µm processes [85, 86].

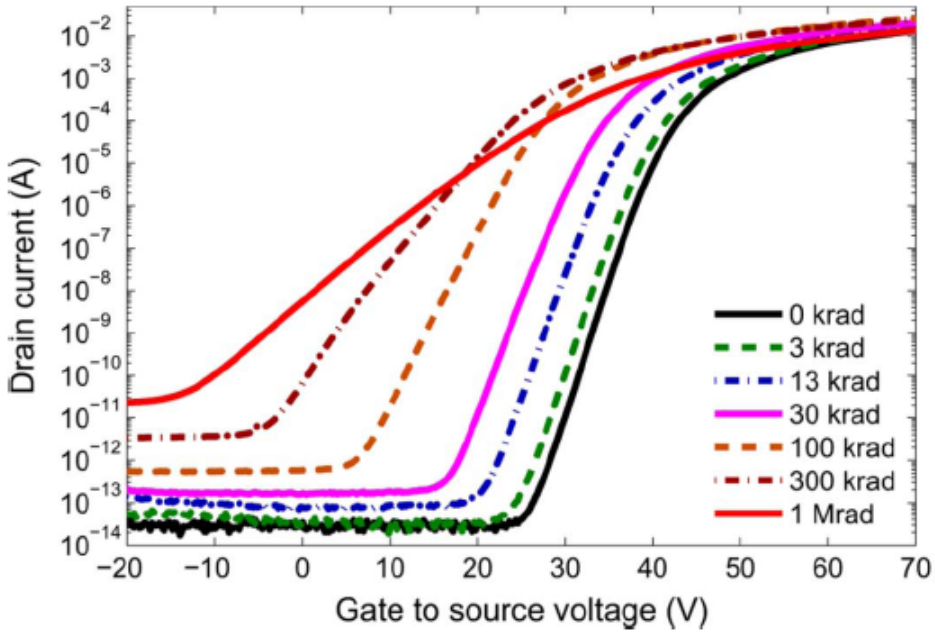

Fig. 2.4. I_d-V_{gs} characteristics of FOXFET devices fabricated in a 0.18 µm CMOS image sensor process after exposure to increasing total dose levels using 10 keV X-rays [88].

Recently, dose rate effects in advanced CMOS technologies were investigated by Witczak *et al*. [90] and Johnston *et al*. [91]. Contrary to the conventional wisdom, these studies seem to indicate some enhancement in degradation at low dose rates (LDR) measured by higher levels of edge leakage in n-channel devices. Shown in Fig. 2.5 is a plot of I_{off} as a function of irradiation and anneal time for standard n-channel transistors fabricated in the TSMC 0.18 µm process exposed to ^{60}Co gamma rays at different dose rates and up to a total dose of 80 krad(SiO_2) [90]. These results show that degradation is greater following LDR irradiation than high dose rate (HDR) irradiation plus anneal. In [90], Witczak *et al*. were able to obtain reasonable fits between the experimental data and simulations using a uniform sheet density of positive charge along the STI sidewall. The density is calculated by means of a simple first-order kinetics model for the trapping and de-trapping in the field oxide. From these results, Witczak *et al*. concluded that dose-rate sensitivity in some CMOS devices may be due to slower annealing rates at LDR suggesting the contribution of space charge effects by altering the spatial distribution of trapped holes in the field oxides. At LDR, charge trapping may concentrate in regions further away from the interface, therefore, decreasing the annealing rate.

In [91], Johnston *et al*. proposed that LDR enhancement was determined by the dose rate dependent buildup of trapped charge (holes) near the corner of the trench. The dose rate dependence was attributed to several factors: 1) initial recombination can be reduced at low-fields (i.e., higher charge yield at low dose rates) leading to higher degradation, 2) asymmetric field lines in the corner of the

shallow trench isolation (STI) leading to a non-uniform buildup of charge along the interface as a function of time and dose, and 3) recombination mechanisms acting upon charge confined within the STI oxide at high dose rates (HDR) [91]. More details on the mechanism for enhanced LDR damage are provided in the following section.

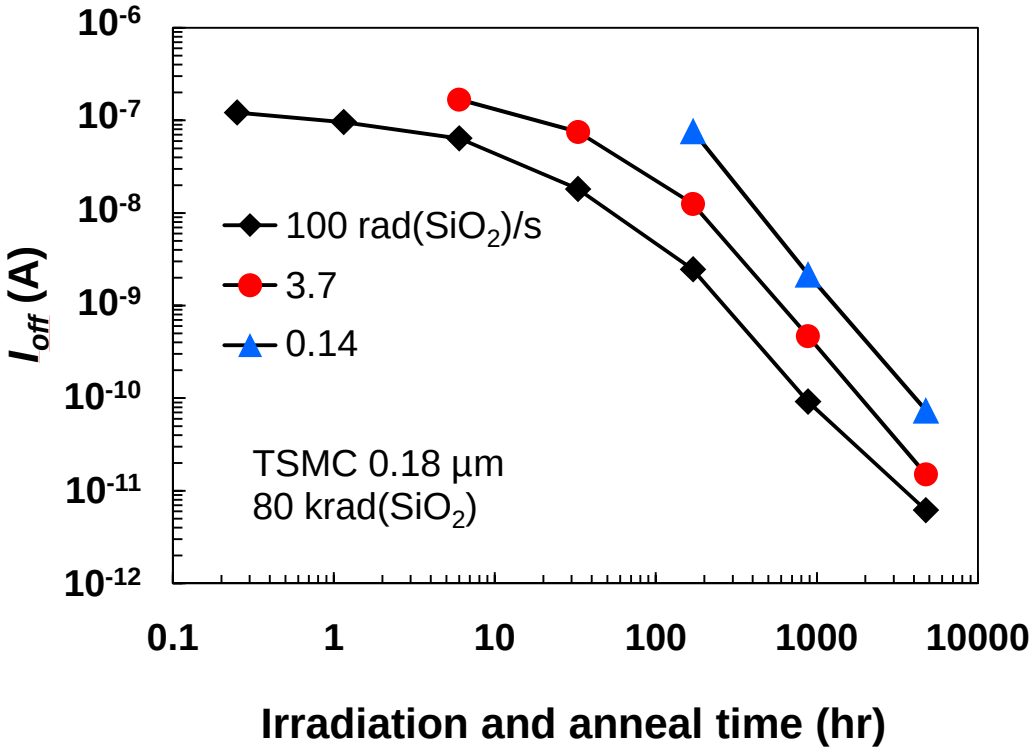

Fig. 2.5. I_{off} as a function of irradiation and anneal time for standard n-channel transistors fabricated in the TSMC 0.18 µm process exposed to ^{60}Co gamma rays at different dose rates and up to a total dose of 80 krad(SiO_2) [90].

In summary, degradation in the thin gate oxides of advanced deep-submicron CMOS technologies is greatly reduced by scaling and is unlikely to have an impact in the radiation response. Therefore, radiation damage is assumed to

occur primarily in the isolating field oxides. Since the depth of STI oxides is not very sensitive to scaling, the trend in commercial CMOS processes towards higher total dose hardness can be attributed to several other factors such as increased doping concentrations, advances in STI processing and reduced supply voltages. Dose-rate sensitivity in deep-submicron CMOS technologies has been previously examined through measurements of edge-leakage in standard n-channel transistors. The effects of non-uniform field lines along the sidewall of STI oxides on charge yield, hole transport and hole trapping and de-trapping have been suggested as the mechanisms contributing to the enhancement in leakage observed at low dose rates. Degradation observed in the I_d-V_{gs} characteristics of irradiated FOXFET devices has allowed determining a significant buildup of trapped holes and interface traps along the base of STI oxides in deep-submicron CMOS technologies. FOXFET devices allow analyzing the basic mechanisms contributing to the time-dependent buildup of radiation-induced defects in STI oxides without the nuisance of these non-uniformities and to readily extract their densities (i.e., N_{ot} and N_{it}). The following section discusses these mechanisms in terms of a physical model for the buildup of N_{ot} and N_{it} in STI oxides.

2.2 Theory of Radiation Effects in Shallow Trench Isolation Oxides

This section of the dissertation discusses a theoretical model for the physical mechanisms that contribute to the buildup of radiation-induced defects in SiO_2 following exposure to ionizing radiation. The presented model incorporates hole trapping and de-trapping mechanisms as well as the formation of interface traps

due to the release of hydrogen as described by the two-stage hydrogen model [58]. The key reactions of the basic two-stage model and the kinetic equations describing the motion of various species and their interactions are described in this section. The effects of the various parameters governing the time-dependent buildup of oxide trapped charge and interface traps are calculated and analyzed by solving the set of equations that form the physical model. Dose-rate effects are investigated following the approach described by Hjalmarson *et al*. in [92] which adopts most of the formalisms presented in [93-95]. Here, hydrogen cracking at positively charged defects and other bimolecular reactions are considered in the calculations for analyzing the physical mechanisms that lead to enhanced low dose rate sensitivity (ELDRS) in bipolar technologies. Additionally, space charge effects that lead to dose-rate sensitivity are also investigated. These effects are due to localized electric fields caused by radiation-generated species that can alter the transport of charged particles during irradiation.

Calculations incorporating key mechanisms are used to describe the dose-rate dependent buildup of radiation-induced defects in STI oxides of advanced CMOS technologies. Analyzing the effects of different model parameters and reactions on the dose-rate dependent buildup of N_{ot} and N_{it} allows determining how the basic mechanisms attributed to ELDRS apply to CMOS technologies. A modeling approach which allows readily determining the key reactions that result in proper modeling of the effects observed experimentally in advanced CMOS technologies is adopted in this dissertation. In this approach we begin by defining the most basic (i.e., minimum set) of reactions followed by an incremental inclusion while

monitoring and analyzing the simulation results. The complete finite-difference discretization of the differential equations that form the physical model as well as the numerical methods used for solving the system of equations are given in the Appendix.

Considering the two-stage model, the basic mechanisms to be included in the calculations are described by the following set of reactions between the mobile species and defects [92, 96]:

a) Hole trapping: $D_A + p \rightarrow D_A^+$ (2.1)

$D_A^+ + n \rightarrow D_A$ (2.2)

b) Proton Release: $D_BH + p \rightleftarrows D_BH^+$ (2.3)

$D_BH^+ \rightarrow D_B + H^+$ (2.4)

$D_BH^+ + n \rightarrow D_BH$ (2.5)

c) De-passivation reaction: $P_bH + H^+ \rightarrow P_b^+ + H_2$ (2.6)

Reactions (2.1) – (2.6) describe the physical mechanisms following radiation-induced generation of electron-hole pairs and initial "prompt" recombination. As described in Chapter 1, hole trapping occurs at defects sites (i.e., precursor centers) generally associated with oxygen vacancies in SiO_2. These neutral hole trapping precursors are denoted as D_A in reactions (2.1) – (2.2). When a hole is captured at an oxygen vacancy, it will produce a positively charged *E*' center (i.e., D_A^+) with a deep-energy level as described by reaction (2.1). The positively charged defect D_A^+ is assumed to be fixed (i.e., hole de-trapping mechanisms are not modeled), since *E*' centers have deep energy levels. However, a positively

charged defect can be neutralized by capturing an electron as described by reaction (2.2).

The formation of interface traps occurs through the "de-passivation" of P_b centers at the Si-SiO_2 interface. As described in the two-stage model [58], protons (H^+) are first released within the oxide and then migrate towards the interface where they can react with the passivated dangling bond to form interface traps. It is commonly assumed that the proton is released following hole capture [92]. The first stage of the model is described by reactions (2.3) – (2.5). In these reactions, D_B denotes the neutral hole trap, and D_BH the hydrogenated neutral hole trap. The atomic nature of D_B is not determined. Reactions (2.3) and (2.4) describe proton release following hole capture. Reaction (2.5) describes electron compensation at a positively charged hydrogenated defect (i.e., D_BH^+). Competition between reactions (2.4) and (2.5) make this mechanism dose-rate dependent [92]. In the second stage of the model the protons that have reached the Si-SiO_2 interface can react with passivated P_b centers (P_bH) as described by (2.6). The passivated P_b centers are dangling bonds that have been passivated by hydrogen during processing. This reaction will produce a dangling bond and a neutral hydrogen molecule.

Reactions are formulated into continuity equations describing the reactive transport for each mobile species. Following the notation in [92], the continuity equations are given by

$$\frac{dn_i}{dt} + \nabla \cdot \mathbf{J}_{si} = \sum_j \nu_{ij} R_j \,. \tag{2.7}$$

In (2.7), $n_i \equiv n_i(\mathbf{r},t)$ is the density for each species i defined as a function of position $\mathbf{r}$ and time t, $\mathbf{J}_{si}$ is the species current density, R_j is the reaction rate, and ν_{ij} is the stoichiometric coefficient giving the contribution from reaction j to species i [92]. The time and space dependent continuity equation for electrons, holes and protons in a simple 1-D SiO_2 structure are given by

$$\frac{\partial n}{\partial t} = -\frac{\partial f_n}{\partial x} + G_n - R_n, \tag{2.8}$$

$$\frac{\partial p}{\partial t} = -\frac{\partial f_p}{\partial x} + G_p - R_p, \tag{2.9}$$

$$\frac{\partial n_{H^+}}{\partial t} = -\frac{\partial f_{H^+}}{\partial x} + G_{H^+} - R_{H^+}. \tag{2.10}$$

In (2.8) – (2.10), the contributions from all reactions are included in the corresponding generation and recombination terms for electrons, holes and protons (i.e., G_n, R_n, G_p, R_p, G_{H^+} and R_{H^+}). The generation terms for electrons and holes describe the radiation-induced generation of ehps. The generation of ehps is determined by the product of the dose rate ($\dot{D}$), the hole fractional yield (f_y) and the conversion factor g_0 given by (1.1). Therefore,

$$G_n = G_p = G = \dot{D} g_0 f_y. \tag{2.11}$$

Charge yield is dependent on the magnitude of the local electric field and can be approximated as

$$f_y(\vec{E}) \approx \left(\frac{|\vec{E}|}{|\vec{E}| + E_0} \right), \tag{2.12}$$

where $\vec{E}$ is the local field vector and E_0 is the threshold field constant (= 5.5×10^5 V/cm) [97-100]. For ^{60}Co gamma rays and 10 keV X-rays, the field dependence of hole yield can be approximated empirically as [101, 102]

$$f_y(\vec{E}) = \left(\frac{0.5}{|\vec{E}|} + 1 \right)^{-0.7} \qquad \text{for } ^{60}\text{Co} \tag{2.13}$$

and

$$f_y(\vec{E}) = \left(\frac{1.35}{|\vec{E}|} + 1 \right)^{-0.9} \qquad \text{for X-rays,} \tag{2.14}$$

where $\vec{E}$ is in units of MV/cm. The remaining recombination and generation terms in Equations (2.8) – (2.10) are summarized in Table 2.2.

TABLE 2.2
SUMMARY OF RECOMBINATION REACTIONS AND RATES FOR ELECTRONS AND HOLES

Symbol	Description	Equation	Number
G_{pt1}	Hole capture at deep energy traps	$G_{pt1} = \sigma_{pta} f_p N_{TA}$	(2.15)
G_{pt2}	Hole trapping at hydrogenated defects	$G_{pt2} = \sigma_{ptb} f_p N_{TB}$	(2.16)
R_{pt1}	Electron compensation at positively charged deep energy traps	$R_{pt1} = \sigma_{npta} f_n p_{t,A}$	(2.17)
R_{pt2}	Electron compensation at positively charged hydrogenated defects	$R_{pt2} = \sigma_{nptb} f_n p_{t,B}$	(2.18)
R_{ptd}	Hole de-trapping from hydrogenated defect	$R_{ptd} = r_{ptd} p_{t,B}$	(2.19)
R_{pth}	Proton release from positively charged hydrogenated defect	$R_{pth} = r_{pth} p_{t,B}$	(2.20)
R_{it}	Formation of interface trap by de-passivation of P_b center	$R_{it} = \sigma_{it} f_{H^+} N_{P_b H}$	(2.21)

In application of the formalism described by (2.7), the sum of contributions from recombination mechanisms of all different reactions for electrons, holes, and traps are given by

$$\sum_j v_{nj} R_j = G_n - R_n = G - R_{pt1} - R_{pt2}, \tag{2.22}$$

$$\sum_j v_{pj} R_j = G_p - R_p = G + R_{ptd} - G_{pt1} - G_{pt2}, \tag{2.23}$$

$$\sum_j v_{H^+ j} R_j = G_{H^+} - R_{H^+} = R_{pth} - R_{it}. \tag{2.24}$$

In (2.15) – (2.21), N_{TA} and N_{TB} are the density of hole traps and hydrogenated defects (or DH centers), $p_{t,A}$ and $p_{t,B}$ are the density of trapped holes at hole traps and at hydrogenated defects, σ_{pta} and σ_{ptb} are the capture cross-sections for holes at hole traps and at hydrogenated defects, σ_{npta} and σ_{nptb} are the capture cross-sections for electrons at positively charged hole traps and at positively charged hydrogenated defects, r_{ptd} and r_{pth} are the hole emission and proton release coefficients for positively charged hydrogenated defects, and σ_{it} and N_{P_bH} are the capture cross section for protons at passivated P_b centers and the density of passivated P_b centers at the Si-SiO_2 interface. All densities listed above are space and time dependent variables and all capture cross-sections and release factors are constants. The rates for hole and electron trapping listed in Table 2.2 are directly proportional to the corresponding species flux (where flux of species i is $f_i = |\mathbf{J}_{si}|/q$). The electron, hole and proton fluxes are given by

$$f_n = \frac{|\mathbf{J}_n|}{q} = \frac{1}{q}\left|n\mu_n E_x + D_n \frac{\partial n}{\partial x}\right|, \tag{2.25}$$

$$f_p = \frac{|\mathbf{J}_p|}{q} = \frac{1}{q}\left|p\mu_p E_x - D_p \frac{\partial p}{\partial x}\right|, \tag{2.26}$$

$$f_{H^+} = \frac{|\mathbf{J}_{H^+}|}{q} = \frac{1}{q}\left|n_{H^+}\mu_{H^+} E_x - D_{H^+} \frac{\partial n_{H^+}}{\partial x}\right|. \tag{2.27}$$

Here, E_x is the electric field in the oxide, n, p and n_{H^+} are the electron, hole, and proton densities, μ_n, μ_p and μ_{H^+} the electron, hole and proton mobilities in SiO_2 and D_n, D_p and D_{H^+} are the electron, hole and proton diffusivities in SiO_2. The resulting kinetic equations for the trapped holes (i.e., p_{t1} and p_{t2}) and the interface traps (or de-passivated P_b center) are

$$\frac{dp_{t,A}}{dt} = \sigma_{pta} f_p N_{TA} - \sigma_{npta} f_n p_{t,A}, \tag{2.28}$$

$$\frac{dp_{t,B}}{dt} = \sigma_{ptb} f_p N_{TB} - \sigma_{nptb} f_n p_{t,B} - r_{ptd} p_{t,B} - r_{pth} p_{t,B}, \tag{2.29}$$

$$\frac{dP_b}{dt} = \sigma_{it} f_{H^+} N_{P_b H}. \tag{2.30}$$

Hole and electron trapping can be alternatively described in terms of a recombination rate and the corresponding species density (i.e., instead of being described in terms of the fluxes). In this case, the kinetic equations are given by

$$\frac{dp_{t,A}}{dt} = c_1 p N_{TA} - c_2 n p_{t,A}, \tag{2.31}$$

$$\frac{dp_{t,B}}{dt} = c_3 p N_{TB} - c_4 n p_{t,B} - r_{ptd} p_{t,B} - r_{pth} p_{t,B}, \tag{2.32}$$

$$\frac{dP_b}{dt} = c_5\, n_{H^+} N_{P_bH}, \tag{2.33}$$

where c_1, c_2, c_3, c_4 and c_5 are capture coefficients constants with units of [cm^3/s]. Capture coefficients are given by the product of the mobile species thermal velocity and the capture cross section of the defect [103].

In addition to the continuity equations for the mobile species and kinetic equations for trapped charges, the kinetic equations for the hole traps and the passivated P_b centers must be determined. These are given by

$$\frac{\partial N_{TA}}{\partial t} = R_{pt1} - G_{pt1}, \tag{2.34}$$

$$\frac{\partial N_{TB}}{\partial t} = R_{pt2} + R_{ptd} + R_{pth} - G_{pt2}, \tag{2.35}$$

$$\frac{\partial N_{P_bH}}{\partial t} = - R_{it}\,. \tag{2.36}$$

Finally, the electrostatic potential (ψ) is obtained by solving Poisson's equation given by

$$\frac{\partial^2 \psi}{\partial x^2} = -\frac{\rho_{ox}}{\varepsilon_{ox}} = -\frac{q}{\varepsilon_{ox}} \left(p + p_{t,A} + p_{t,B} + n_{H^+} + n_{P_b^+} - n \right), \tag{2.37}$$

where all charged particles are included in the charge density term (ρ_{ox}). Calculations of the time-dependent buildup of radiation-induced defect, i.e., N_{ot} and N_{it}, are respectively discussed in the remaining sections of this Chapter. There are certainly other processes likely to occur during irradiations that are not included in the present model (e.g., electron trapping, hydrogen re-trapping, proton neutralization, hydrogen dimerization) [92, 96]. However, the set of

reactions incorporated into the model are sufficient for reasonably describing the time-dependent buildup of N_{ot} and N_{it} in STI oxides of deep-submicron CMOS technologies. The effect of molecular hydrogen on the dose-rate sensitivity is also discussed by the introduction of hydrogen cracking mechanisms.

Initial calculations of the radiation-induced defects are presented in the remaining sections of this chapter. These calculations are included to demonstrate the contributions to the time-dependent buildup of N_{ot} and N_{it} from the different reactions considered in the model. Additional calculations are presented in Chapter 4 following an experimental parameterization of the model. These additional calculations allow investigating and simulating the key mechanisms contributing to the radiation response of STI oxides and to support the formulation of analytical models for ΔN_{ot} and ΔN_{it} as a function of dose and dose rate.

2.3 Numerical Calculations of Oxide Trapped Charge Density

This section of the dissertation describes 1-D numerical calculations for hole trapping in SiO_2 during exposure to ionizing radiation. These calculations incorporate the radiation-induced generation of ehps, geminate recombination, drift-diffusion transport of mobile species in SiO_2, hole trapping and electron compensation mechanisms. Therefore, for these calculations, only reactions (2.1) and (2.2) are included in the reactive transport of electron and holes following generation and prompt recombination. Reactions (2.3) – (2.6) are included in calculations of the time-dependent buildup of interface traps presented in the following section. In the following section additional reactions describing the

process of molecular hydrogen “cracking” at positively charged defects are introduced to model the effects of hydrogen on dose-rate. Electrostatic effects are included in the calculations through contributions to the time-dependent electric field from the gate bias, space-charge of all charged particles and band bending at the Si surface (i.e., calculations of surface potential ψ_s).

A finite-difference methodology is used to compute solutions for the densities of the mobile species as well as for the electrostatic potential (ψ) at nodes contained within a mesh superimposed on the solution domain. The time-dependent continuous differential equations are therefore replaced by discretized finite-difference approximations. The full expansion of the finite-difference continuity equations are given in the Appendix. The simultaneous set of equations is solved sequentially using a successive-under-relaxation (SUR) iterative method and an implicit time stepping scheme. Descriptions of the numerical methods are given in the Appendix. Shown in Fig. 2.6 is a schematic diagram of the simulated 1-D SiO_2 structure with thickness of t_{ox} = 425 nm indicating the coordinate and mesh notation and the electrostatic potential boundary conditions. The boundary conditions are set to allow mobile species to flow out of the sample. The electrostatic potential is fixed at the gate contact (i.e., at $x = 0$) by the gate bias and workfunction difference and at the Si surface (i.e. at $x = t_{ox}$) by the surface potential (ψ_s) which is calculated at every time step. A list of the material parameters used in these calculations is given in Table 2.3.

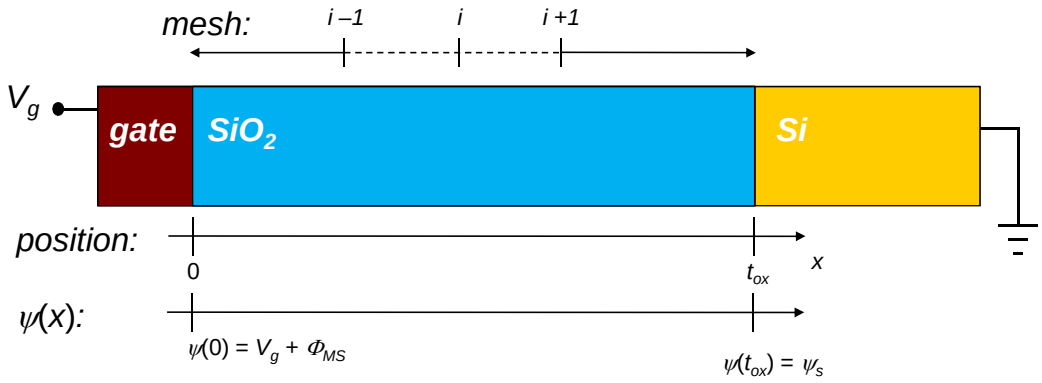

Fig. 2.6. Schematic diagram of the simulated 1-D SiO_2 structure with thickness of t_{ox} = 425 nm, indicating the coordinate and mesh notation, and the electrostatic potential boundary conditions.

TABLE 2.3
SUMMARY OF THE SiO_2 MATERIAL PARAMETERS USED IN SIMULATIONS

Parameter	Symbol	Value	Units
Energy Bandgap	E_g	9	eV
Permittivity	ε_{ox}	3.9	N/A
Valence band effective density of states	N_v	1×10^{19}	cm^{-3}
Conduction band effective density of states	N_c	1×10^{19}	cm^{-3}

Fig. 2.7 plots the distribution of $p_{t,A}$ (holes trapped in defects D_A) as a function of position (depth) at various total dose levels up to 500 krad(SiO_2). These results are for a uniform density of hole traps, i.e., $N_{TA} = 9.8\times10^{18}$ cm^{-3}, located within 25 nm of the Si-SiO_2 interface and for a dose rate of 100 rad(SiO_2)/s. Other simulation parameters are $\mu_n = 20$ $cm^2V^{-1}s^{-1}$, $\mu_p = 1\times10^{-6}$ $cm^2V^{-1}s^{-1}$, $\sigma_{pta} = 1.5\times10^{-14}$ cm^2, $\sigma_{npta} = 10^{-15}$ cm^2 and a gate bias of $V_g = 1$ V. In Fig. 2.7, solid lines are calculations obtained using the presented model and symbols are

obtained from the radiation effects module in Silvaco, a commercial TCAD (technology computer aided design) simulator that allows modeling ehps generation and trapping in SiO_2 [100]. Proton release mechanisms, proton transport, and interface trap formation by de-passivation mechanisms are not incorporated into Silvaco's radiation effects module. The calculations of $p_{t,A}$ indicate that for these conditions and simulation parameters, the buildup of trapped charge is fairly uniform in space up 500 krad(SiO_2).

The effects of the electron compensation process described by reaction (2.3) can be observed in the results plotted in Fig. 2.8. These calculations are for the same conditions except that the capture cross section of electrons at positively charge defects is increased by two orders of magnitude, i.e., $\sigma_{npta} = 10^{-13}$ cm^2. Increasing σ_{npta} results in a greater non-uniform spatial distribution of $p_{t,A}$ with greater accumulation of trapped holes near the Si-SiO_2 interface, and lower densities in regions away from the interface. The results in Fig. 2.8 also reveal that the effects of electron compensation are greater at higher dose levels where $p_{t,A}$ is greater, and therefore, the second term in the RHS of (2.28) becomes more significant.

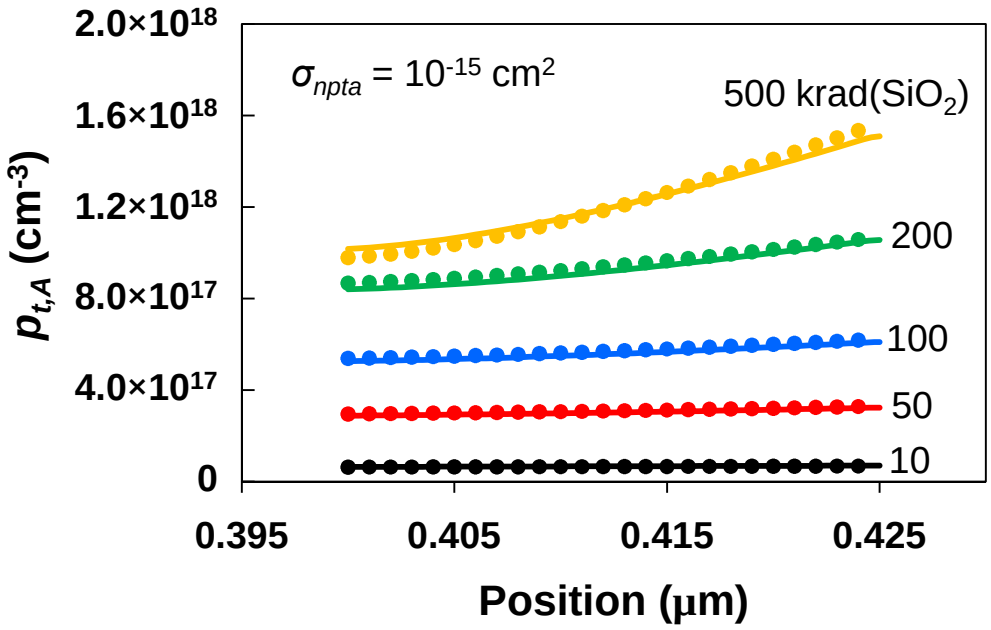

Fig. 2.7. Trapped hole density vs. position for N_{TA} = 9.8×10^{18} cm^{-3} within 25 nm of the Si-SiO$_2$ interface. Solid lines are calculations using the presented model and circles are TCAD solutions. σ_{npta} = 10^{-15} cm^2 for these calculations.

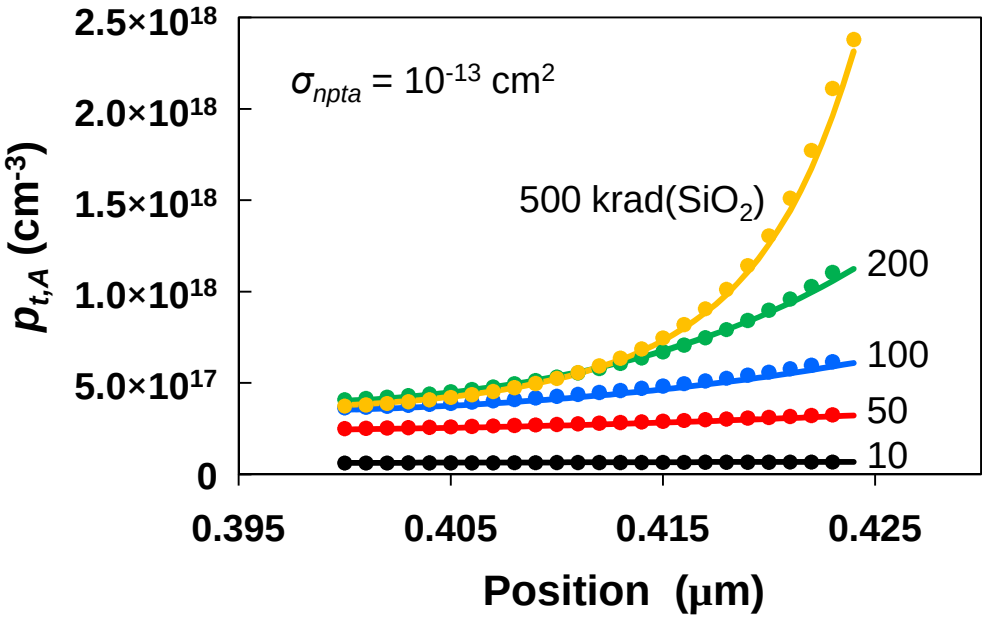

Fig. 2.8. Trapped hole density vs. position for N_{TA} = 9.8×10^{18} cm^{-3} within 25 nm of the Si-SiO$_2$ interface. Solid lines are calculations using the presented model and circles are TCAD solutions. σ_{npta} = 10^{-13} cm^2 for these calculations.

An important parameter to analyze is the effective oxide sheet-charge density (N_{ot}) with units of [cm^{-2}]. This areal density accounts for the total mid-gap voltage shift (V_{mg}) in *I-V* and *C-V* characteristics of MOS devices. N_{ot} can be obtained from an arbitrary distribution of trapped holes $p_{t,A}$ by integrating as [104]

$$N_{ot} = \int_0^{t_{ox}} \frac{x}{t_{ox}} p_{t,A}(x)\, dx. \tag{2.38}$$

Shown in Fig. 2.9 is a plot of N_{ot} as a function of dose for two different values of σ_{npta}. These calculations are for the same conditions and parameters used in the calculations of $p_{t,A}$ plotted in Fig. 2.7 and Fig. 2.8 respectively. These results show that by increasing σ_{npta}, a reduction in N_{ot} is occurs at the higher dose levels as electron compensation mechanisms become significant. At lower dose levels, σ_{npta} has a negligible effect on the buildup of N_{ot} since at these dose levels $p_{t,A}$ (and therefore R_{pt1}) is negligible. In Fig. 2.9 solid lines are calculations obtained using the analytical model and symbols are from TCAD. Another important mechanism of radiation-induced oxide charging is Coulomb confinement. At high levels of radiation dose, the Coulomb potential from the positive charges (i.e. $p_{t,A}$ and positively charged mobile species) confines electrons deep within the oxide. These electrons can recombine at positively charged defects as described by reactions (2.2) and (2.5), whereas electrons near the interfaces can exit the material. Therefore, positive charge accumulates near the Si-SiO_2 interface [92, 105]. Shown in Fig. 2.10 is a plot of the electron density (*n*) vs. position at a total dose of 500 krad(SiO_2) for two different dose rates, 100 rad(SiO_2)/s and 1 rad(SiO_2)/s. Also plotted in Fig. 2.10 is the trapped hole density

as a function of position for a total dose of 500 krad(SiO_2) and for a dose rate of 100 rad(SiO_2)/s. The trapped hole density obtained using a dose rate of 1 rad(SiO_2)/s gives very similar results and is not shown here. These calculations are for a uniform density of hole traps throughout the oxide with a density of N_{TA} = 5×10^{17} cm^{-3}. Other simulation parameters are σ_{pta} = 10^{-14} cm^2, σ_{npta} = 10^{-13} cm^2 and a gate bias of V_g = 1 V. The results in Fig. 2.10 demonstrate the greater buildup of trapped hole density near the interface and the resulting confinement of electrons in the oxide bulk for high dose rates. The effects of Coulomb confinement on the dose-rate dependent buildup of N_{it} are discussed in the following section.

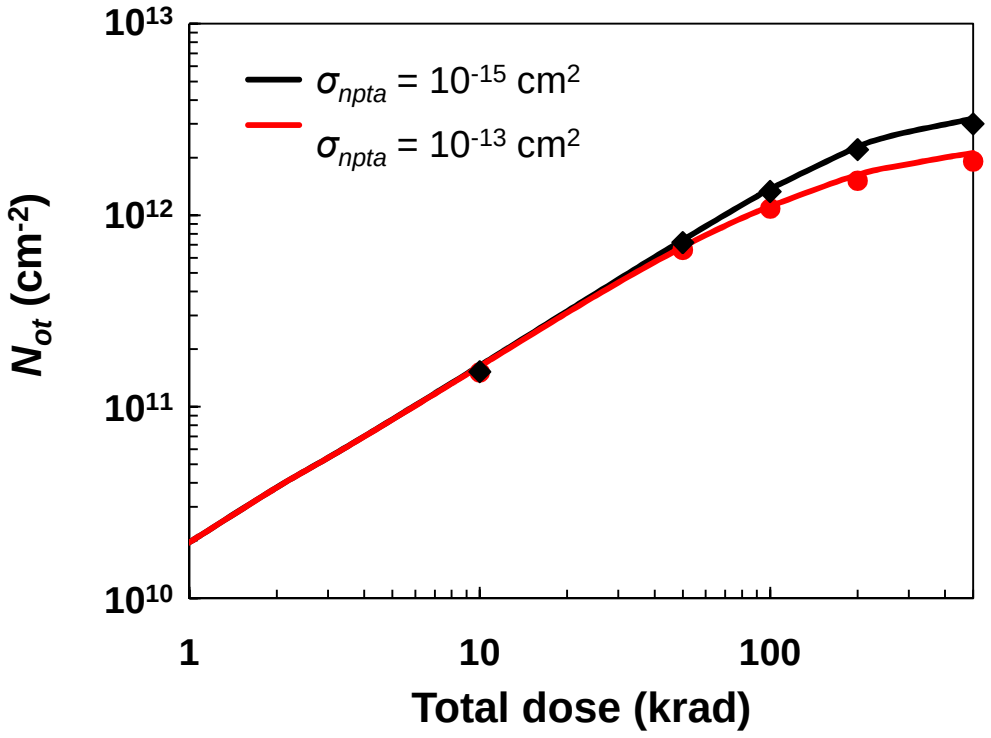

Fig. 2.9. Trapped hole density vs. position for N_{TA} = 9.8×10^{18} cm^{-3} within 25 nm of the Si-SiO_2 interface. Solid lines are calculations using the presented model and circles are TCAD solutions.

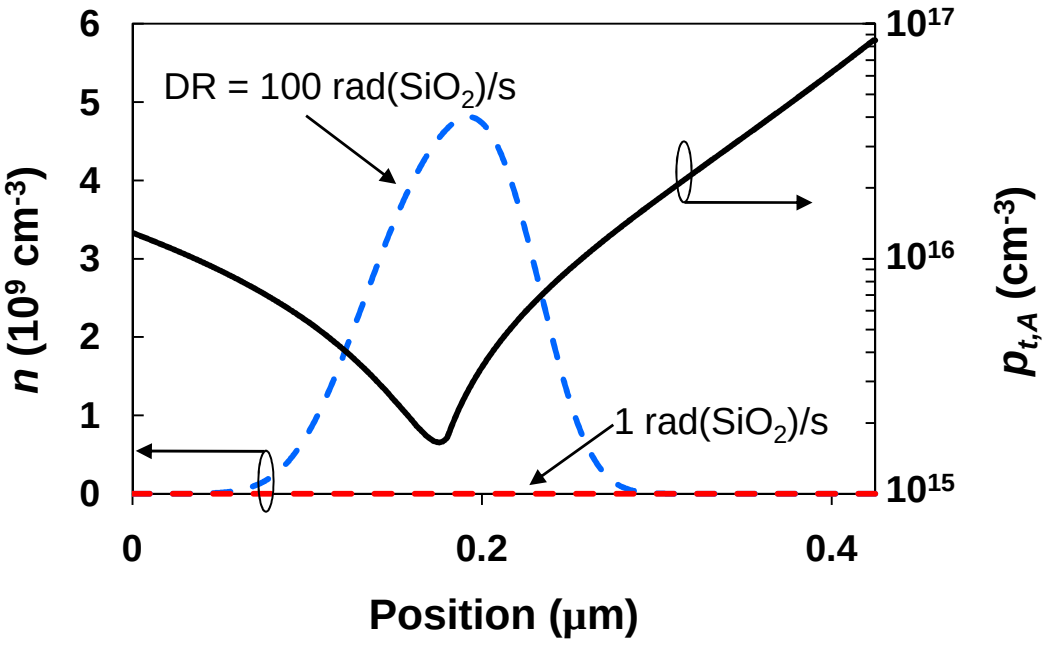

Fig. 2.10. Electron density (n) vs. position at a total dose of 500 krad(SiO_2) for two different dose rates, DR = 100 rad(SiO_2)/s and 1 rad(SiO_2)/s, and the trapped hole density as a function of position at 500 krad(SiO_2) for DR = 100 rad(SiO_2)/s.

2.4 Numerical Calculations of Interface Trap Density

Calculations for the time-dependent buildup of interface traps are presented in this section of the dissertation. These calculations incorporate reactions (2.3) – (2.5) describing proton release and transport stages as well as reaction (2.6) describing the de-passivation reaction at the Si-SiO_2 interface resulting in the formation of interface traps. These calculations are done for the same 1-D SiO_2 structure shown schematically in Fig. 2.6 and using the same material parameters listed in Table 2.3. Shown in Fig. 2.11 is a plot of the interface trap density as a function of total dose for three different values of r_{pth} (i.e., proton release coefficient for positively charged hydrogenated defects). These calculations are for a fixed density of hydrogenated defects, i.e. $N_{TB} = 1\times10^{16}$ cm^{-3}, distributed

uniformly throughout the oxide and for a dose-rate of 10^{-5} rad(SiO_2)/s. Other model parameters used for these calculations are listed in Table 2.4. The results plotted in Fig. 2.11 show that increasing r_{pth} results in higher densities of interface traps. This is true since increasing r_{pth} will result in more proton generation, and therefore, more contribution to the creation of interface traps. Also seen in Fig. 2.11 is that r_{pth} has a greater effect on N_{it} at lower dose levels. This may be true since at higher dose levels, the generation rate for N_{it} might be limited by other mechanisms such as recombination at positively charged hydrogenated defects and space-charge effects retarding the proton transport towards the interface. A uniform density of hole traps (N_{TA} = 5×10^{19} cm^{-3}) was included in these calculations within 25 nm of the Si-SiO_2 interface. Positive charge accumulating in this region can contribute to the aforementioned space-charge effects in these calculations.

The dose rate dependent buildup of interface traps is investigated through calculations of N_{it} as a function of dose rate. Shown in Fig. 2.12, are solutions for N_{it} plotted as a function of dose rate for three different values of electron capture cross section at positively charged hydrogenated defects (σ_{nptb}). As mentioned above, dose-rate effects arise from the competition between reactions (2.4) and (2.5). At higher dose rates, the higher concentration of electrons will enhance recombination at positively charged hydrogenated defects as described by reaction (2.5). Therefore, a reduced number of protons will be released from the remaining defects, as described by reaction (2.4). Since, σ_{nptb} determines the rate of electrons recombining at the positively charged hydrogenated defects,

increasing σ_{nptb} results in a greater enhancement in the buildup of N_{it} between HDR and LDR. These calculations are for a total dose of 50 krad(SiO_2).

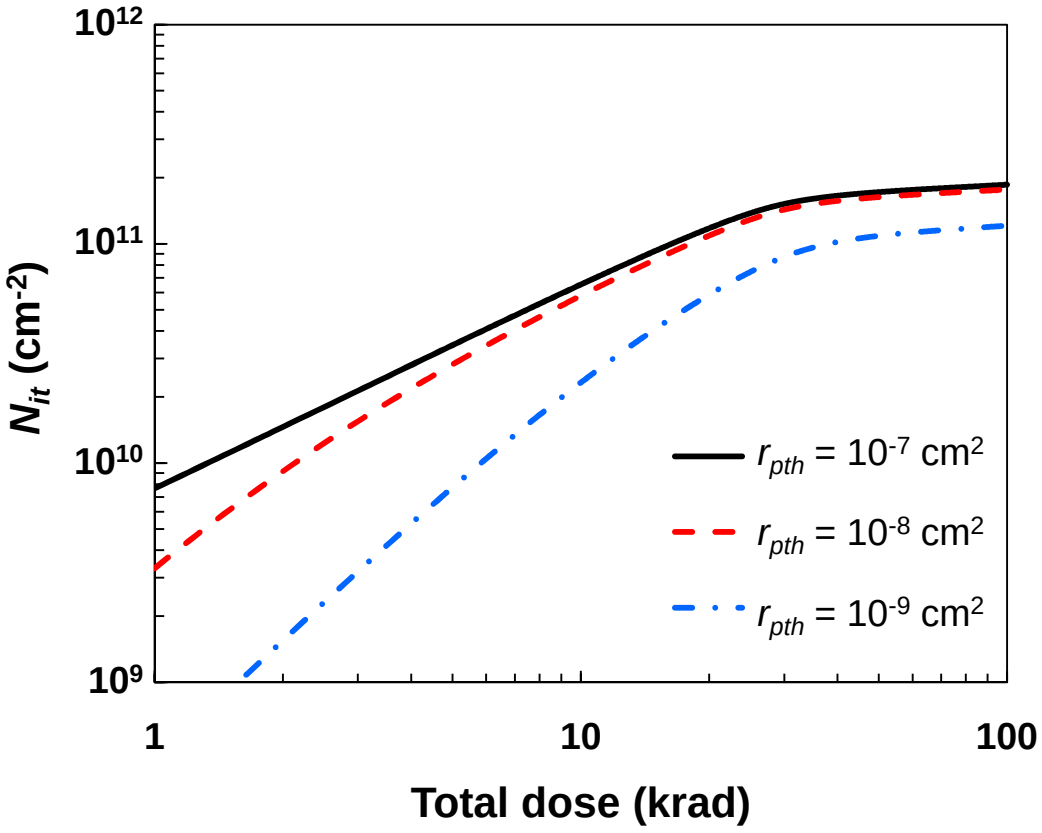

Fig. 2.11. Calculations of interface trap density as a function of total dose using three different values for the proton release coefficient (r_{pth}). These calculations are for a dose rate of 10^{-5} rad(SiO_2)/s.

TABLE 2.4
SUMMARY OF MODEL PARAMETERS USED IN SIMULATIONS FOR N_{it}

Parameter	Symbol	Value	Units
Capture cross-sections for holes at hole traps	σ_{pta}	10^{-14}	cm^2
Capture cross-sections for holes at hydrogenated defects	σ_{ptb}	10^{-14}	cm^2
Capture cross-sections for electrons at positively charged defects	σ_{npta}	10^{-13}	cm^2
Capture cross-sections for electrons at positively charged hydrogenated defects	σ_{nptb}	10^{-11}	cm^2
Capture cross-sections for protons at passivated P_b-centers	σ_{it}	10^{-11}	cm^2
Coefficient for hole emission	r_{ptd}	10^{-11}	s^{-1}
Coefficient for proton release	r_{pth}	10^{-7}	s^{-1}

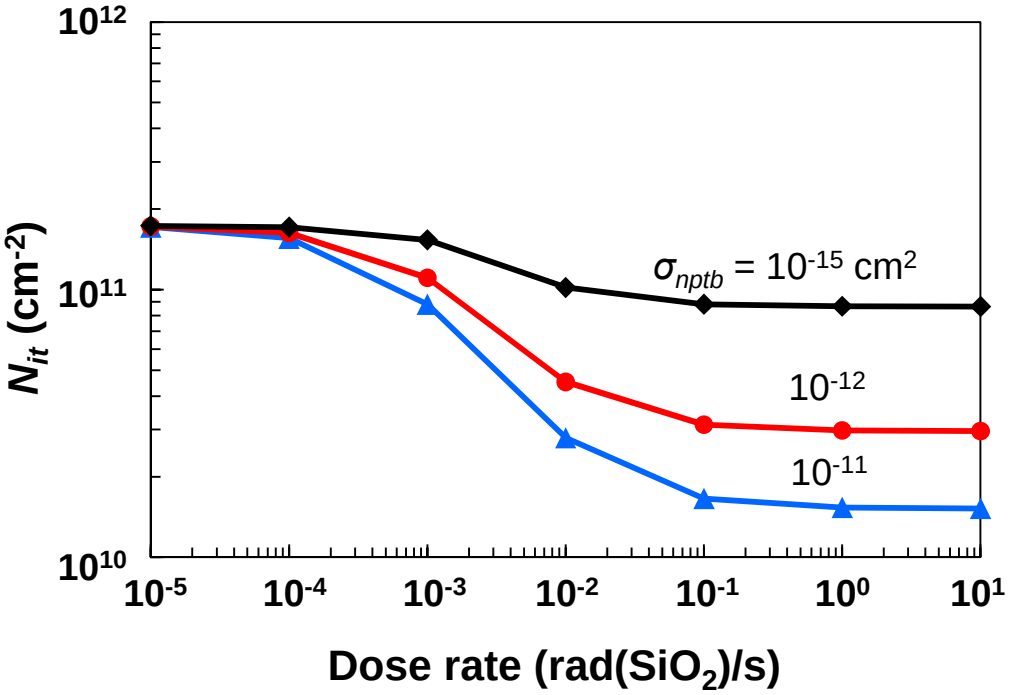

Fig. 2.12. Interface trap density plotted as a function of dose rate for three different values of electron capture cross section at positively charged hydrogenated defects.

Shown in Fig. 2.13 is a plot of the LDR to HDR enhancement factor obtained by the ratio of N_{it} at a total dose of 50 krad(SiO_2) for dose rates of 10^{-5} rad(SiO_2)/s and 100 rad(SiO_2)/s. The enhancement factor is plotted as a function of the electron capture cross section at positively charged hydrogenated defects and for two different densities of hole traps, $N_{TA} = 10^{19}$ cm^{-3} and 10^{20} cm^{-3}, located within 25 nm of the Si-SiO_2 interface. For the lower values of σ_{nptb}, electron compensation at positively charged hydrogenated defects, i.e., reaction (2.5) is not significant. Consequently, the enhancement factor is independent of σ_{nptb} for values below 10^{-13} cm^2. For these values of σ_{nptb}, the simulated enhancement factor is a result of a space charge effect that arises from buildup of fixed positive charge at hole traps near the Si-SiO_2 interface. At $\sigma_{nptb} = 10^{-15}$ cm^2 the enhancement factor is ~1 for $N_{TA} = 10^{19}$ $cm^{-3}$and ~3.9 for $N_{TA} = 10^{20}$ cm^{-3}. N_{TA} has another effect that is evident in the calculations shown in Fig. 2.13 for $\sigma_{nptb} > 10^{-13}$ cm^2. As σ_{nptb} increases, electron compensation becomes significant and the enhancement factor increases since more recombination occurs at higher dose rates (see Fig. 2.12). However, the enhancement is greater for the case of $N_{TA} = 10^{20}$ cm^{-3} since space charge confines electrons in the oxide bulk, allowing more recombination to occur (see Fig. 2.10). A higher N_{TA} results in more fixed positive charge near the Si-SiO_2 interface and therefore more confinement of electrons in the oxide bulk.

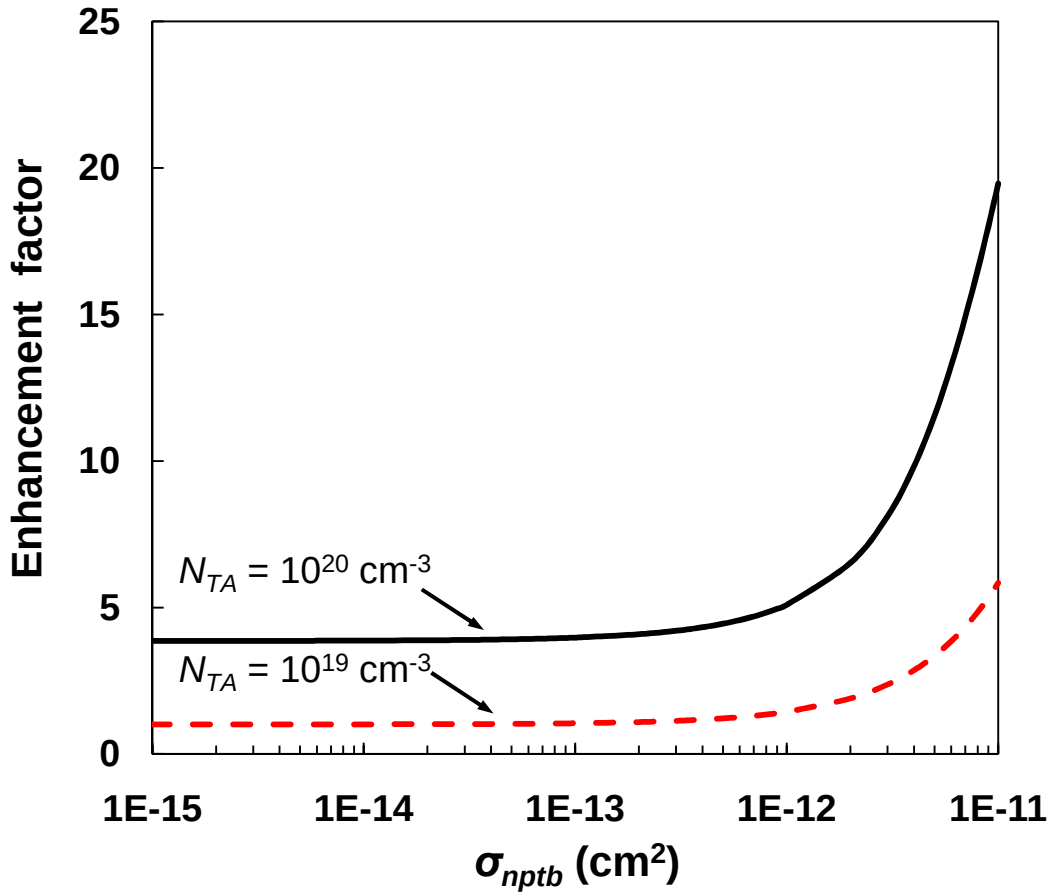

Fig. 2.13. LDR to HDR enhancement factor obtained by the ratio of N_{it} for dose rates of 10^{-5} rad(SiO_2)/s and 100 rad(SiO_2)/s for two different densities of hole traps, N_{TA} = 10^{19} cm^{-3} and 10^{20} cm^{-3}, located within 25 nm of the Si-SiO_2 interface. For these calculations N_{TB} = 10^{16} cm^{-3} and is uniformly distributed in the oxide.

2.5 Modeling the Effects of Hydrogen

This section of the dissertation discusses the effects of molecular hydrogen on the dose rate response of irradiated MOS systems. As described in [105-107], H_2 can diffuse into the oxide and react at defect centers to generate shallow level hydrogen defects (i.e., DH centers). The presented model follows the approach by Hjalmarson *et al.* described in [92] which adopts most of the formalisms

presented by Stahlbush *et al*. and Mrstik *et al*. in [93-95]. In this model, hydrogen cracking occurs only at positively charged defects. Therefore, H_2 disassociates to form DH centers by releasing a proton only after the trapping of a hole (i.e. the positive charging of a defect). The H_2 cracking mechanisms are described by the following set of reactions [92]:

a) Hydrogen cracking:

$$D_C + p \rightleftarrows D_C^+ \tag{2.39}$$

$$D_C^+ + H_2 \rightleftarrows D_C H + H^+ \tag{2.40}$$

$$D_C H + p \rightarrow D_C H^+ \tag{2.41}$$

$$D_C H^+ \rightleftarrows D_C + H^+ \tag{2.42}$$

In reactions (2.39) – (2.42), a third kind of hole trapping defect is introduced, i.e., D_C. In the hydrogen cracking process, (2.39) describes hole trapping resulting in positive charging of D_C. Reaction (2.40) describes the cracking of H_2 at the positively charged defect creating a DH center ($D_C H$) and releasing a proton. The resulting DH center can release additional protons following the two-stage model as described by (2.41) and (2.42). In this case, dose rate dependence results from the competition of (2.40) and electron recombination at D_C^+. By introducing the hydrogen cracking mechanisms into the calculations it is possible to describe the effect of molecular hydrogen on the buildup of interface traps and on the dose rate response of MOS systems. Show in Fig. 2.14 are the model calculations of N_{it} plotted as a function of dose rate for three different concentrations of H_2

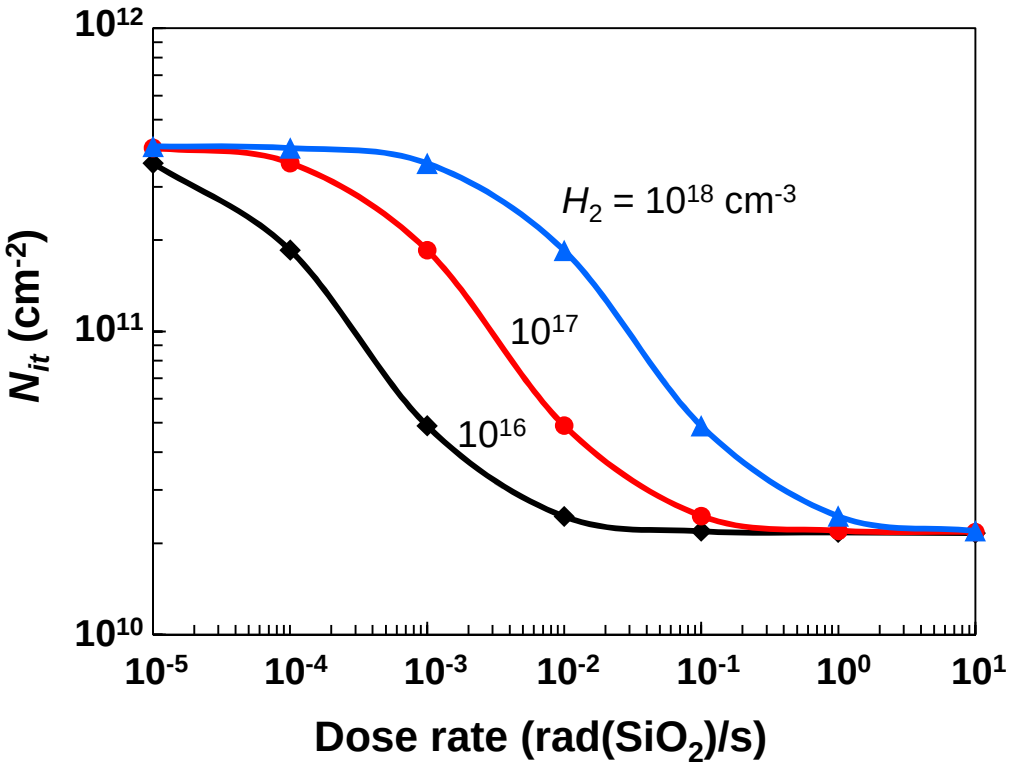

Fig. 2.14. Interface trap density plotted as a function of dose rate for three different concentrations of H_2.

CHAPTER 3. EXPERIMENTAL DETAILS AND RESULTS

3.1 FOXFET Total Dose Experiments

Experimental results obtained from total ionizing dose experiments performed on different test structures are presented in this section of the dissertation. Degradation of the *I-V* characteristics of FOXFET devices uniquely designed to analyze defect buildup and the general susceptibility of STI oxides to ionizing radiation are first presented. These test structures are typically used to analyze the susceptibility of a given technology to inter-device leakage. However, as explained in Chapter 2, they also allow characterizing the time-dependent buildup of radiation-induced defects in STI oxides without having the effects of the non-uniformities at the trench sidewalls and corners, therefore, supporting the parameterization of the physical model presented in Chapter 2. The experimental results reported in this dissertation are from FOXFET devices fabricated in a 90 nm commercial bulk CMOS low-standby power (LSP) technology using STI oxides with a thickness of $t_{ox} \approx 425$ nm. The radiation response of these devices is characterized by step stress irradiation and room temperature anneals for different dose-rates and biasing conditions. Additionally, the radiation-induced degradation of MOS capacitors with thermally grown oxides is also investigated. These devices allow characterizing TID and dose-rate effects in thermally grown SiO_2 and provide a comparison for the radiation response of STI oxides. This comparison provides insight and aids in distinguishing technological parameters related to processing that are of interest in modeling radiation response.

N-well-to-n-well (NW) FOXFET devices were fabricated with two 100 µm fingers (effective width is W = 200 µm) with gate lengths of L = 1.5 µm and L = 0.9 µm and using poly-Si gates. Shown in Figs. 3.1 and 3.2 are the cross-sectional diagram of the NW FOXFET test structure with doping concentrations and dimensions labels and the scanning electron microscope (SEM) image obtained using the focused ion beam (FIB) at Arizona State University [28]. The FOXFET test structures were irradiated in a ^{60}Co gamma irradiation chamber at a dose rate of approximately 20 rad(SiO_2)/s. A gate voltage of V_g = 1 V with all other terminals grounded was used during irradiations. Electrical measurements (I_d-V_{gs} characteristics) were obtained prior to irradiation and after step-stress irradiations up to 20 krad(SiO_2), 100 krad(SiO_2), 200 krad(SiO_2) and 1 Mrad(SiO_2). The electrical measurements consisted of obtaining drain current (I_d) vs. gate-to-source voltage (V_{gs}) characteristics for drain biases of V_d = 100 mV and V_d = 1 V. Plots of the I_d-V_{gs} response pre-irradiation and after several levels of TID using a drain bias of V_d = 100 mV are shown in Figs. 3.3 and 3.4 for devices with L = 0.9 µm and L = 1.5 µm, respectively. Similarly, Figs. 3.5 and 3.6 are plots of the I_d-V_{gs} radiation response using a drain bias of V_d = 1 V for devices with L = 0.9 µm and L = 1.5 µm, respectively.

The buildup of N_{ot} and N_{it} as a function of dose are respectively manifested in the electrical measurements shown in Figs. 3.3 – 3.6 by the negative shifts and the stretch-out of the I_d-V_{gs} characteristics. Both devices (i.e., L = 0.9 µm and L = 1.5 µm) appear to have a similar formation rate for N_{ot} and N_{it}. The buildup of the radiation-induced defect densities are extracted from the data using the

McWhorter-Winokur charge separation technique, where shifts in the I_d-V_{gs} characteristics are separated into shifts due to the positive trapped oxide charge and shifts due to interface states [108]. The densities of N_{ot} and N_{it} extracted from the experimental data are plotted as a function of total dose in Fig. 3.7.

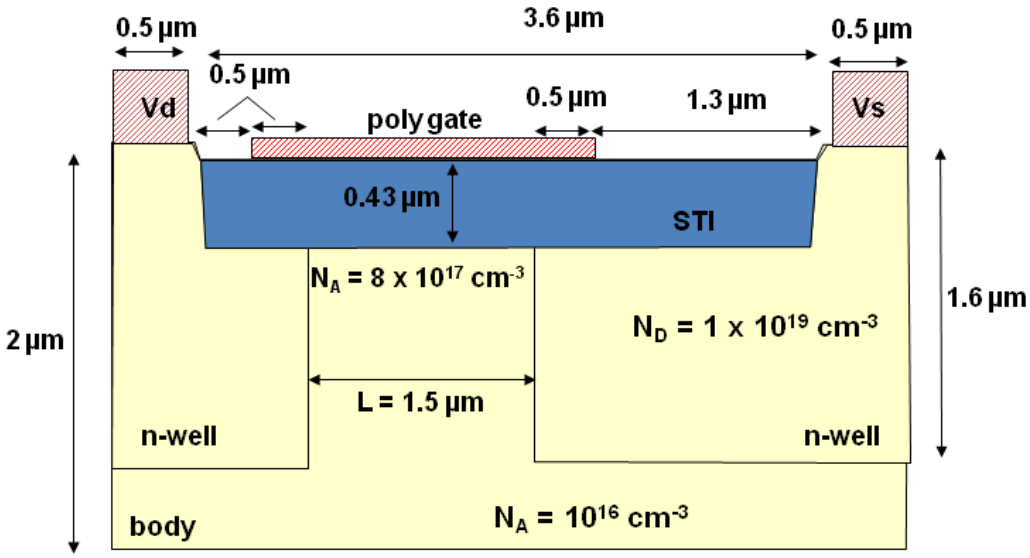

Fig. 3.1. Cross-section of the LSP 90 nm poly gate NW FOXFET (W = 200 µm, L = 1.5 µm) with doping concentration and dimension labels [28].

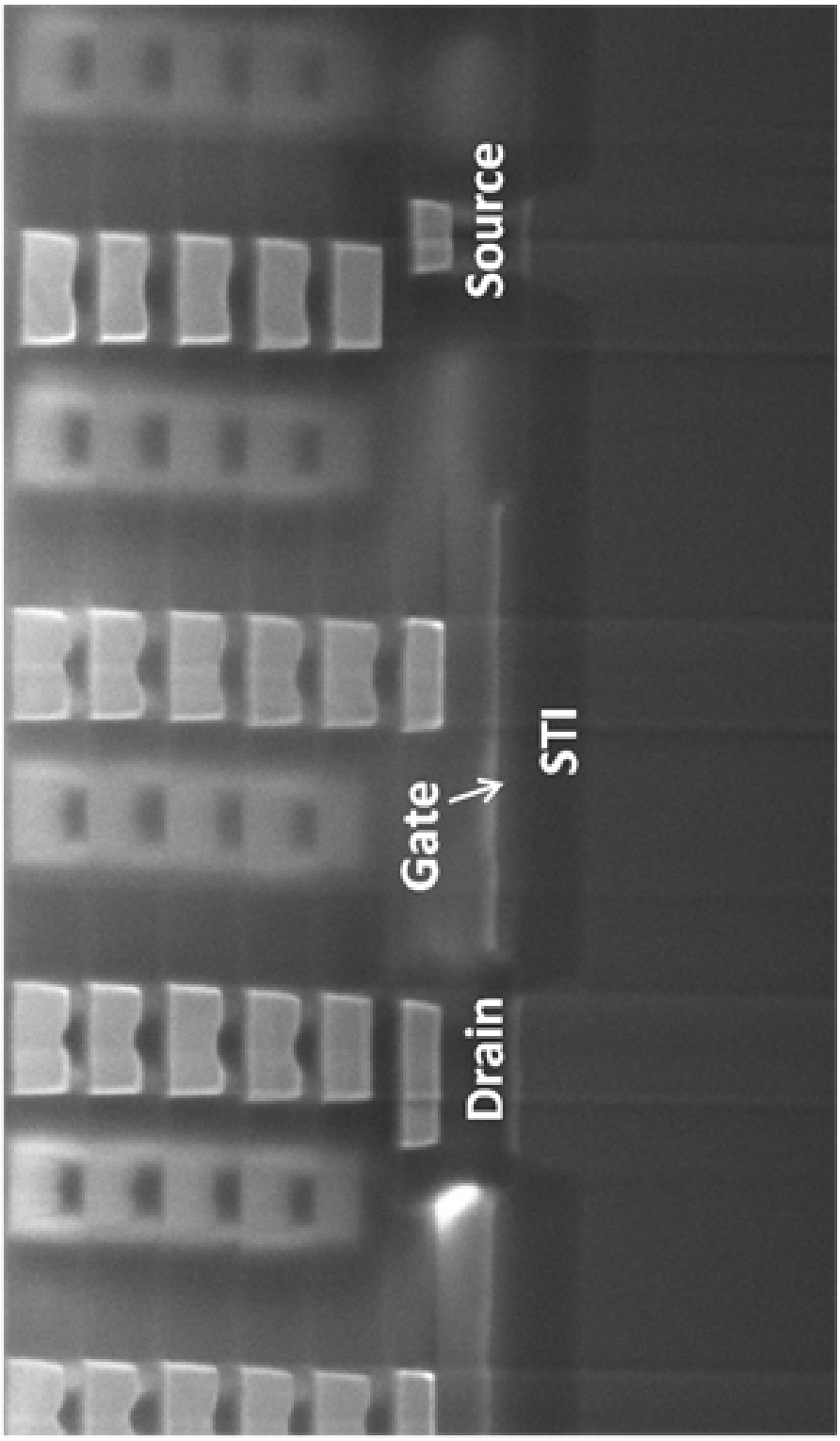

Fig. 3.2. SEM image of the NW FOXFET obtained using the FIB at Arizona State University [28].

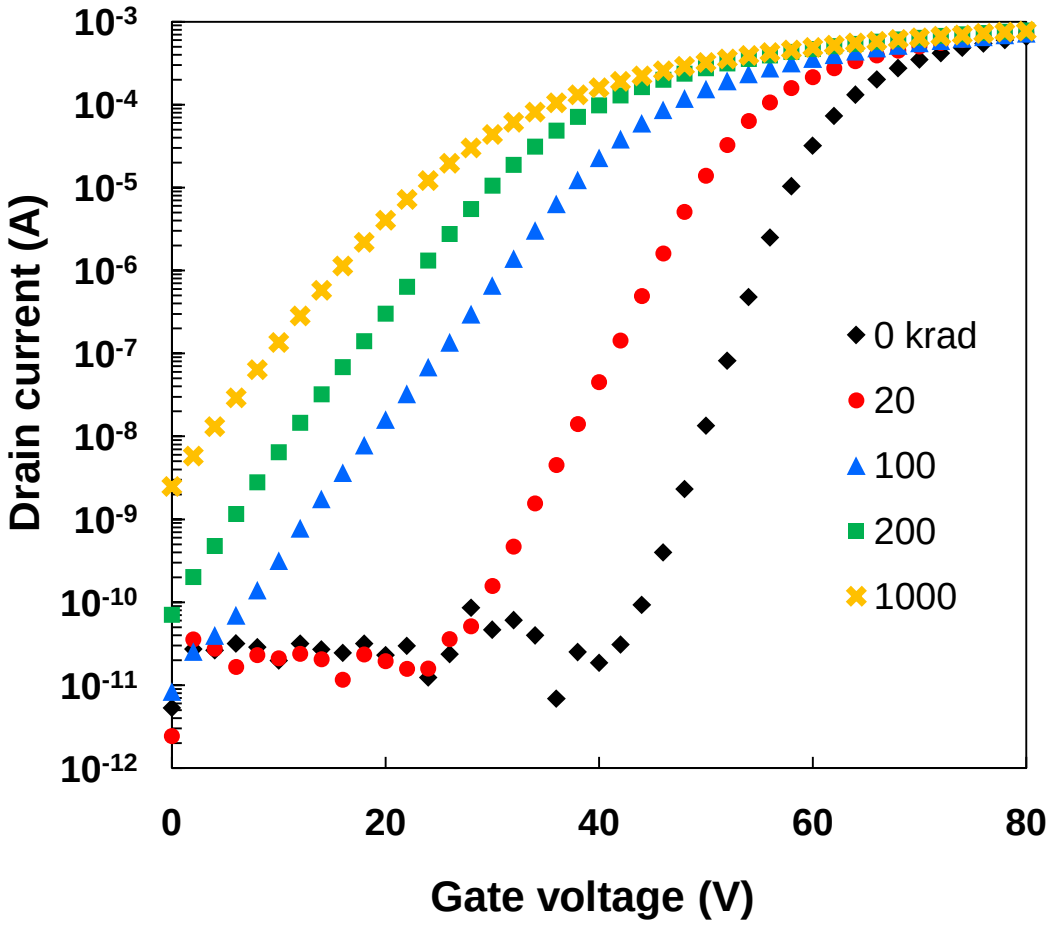

Fig. 3.3. I_d-V_{gs} characteristics before irradiation and after 20, 100, 200 and 1000 krad(SiO_2) of TID for NW FOXFET with W = 200 μm, L = 0.9 μm, V_d = 0.1 V, V_s = V_b = 0 V.

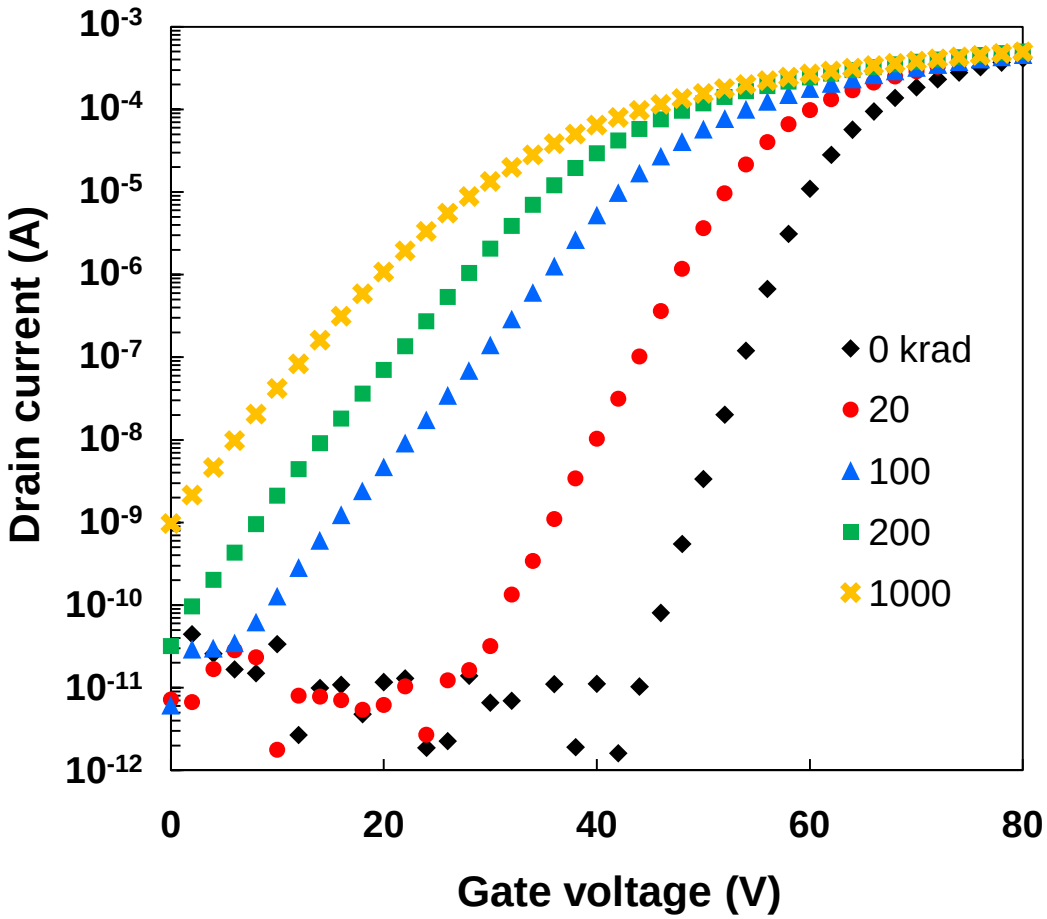

Fig. 3.4. I_d-V_{gs} characteristics before irradiation and after 20, 100, 200 and 1000 krad(SiO_2) of TID for NW FOXFET with W = 200 μm, L = 1.5 μm, V_d = 0.1 V, V_s = V_b = 0 V.

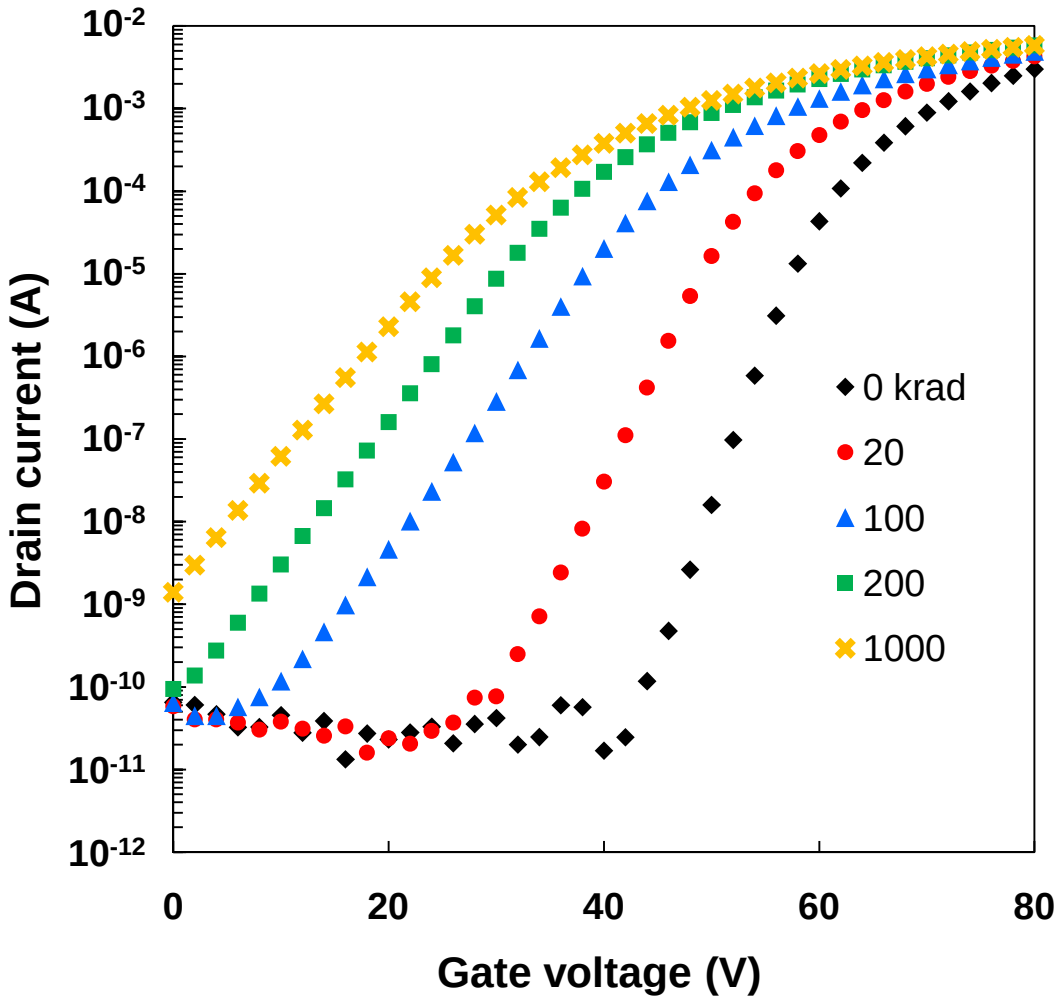

Fig. 3.5. I_d-V_{gs} characteristics before irradiation and after 20, 100, 200 and 1000 krad(SiO_2) of TID for NW FOXFET with W = 200 μm, L = 0.9 μm, V_d = 1 V, V_s = V_b = 0 V.

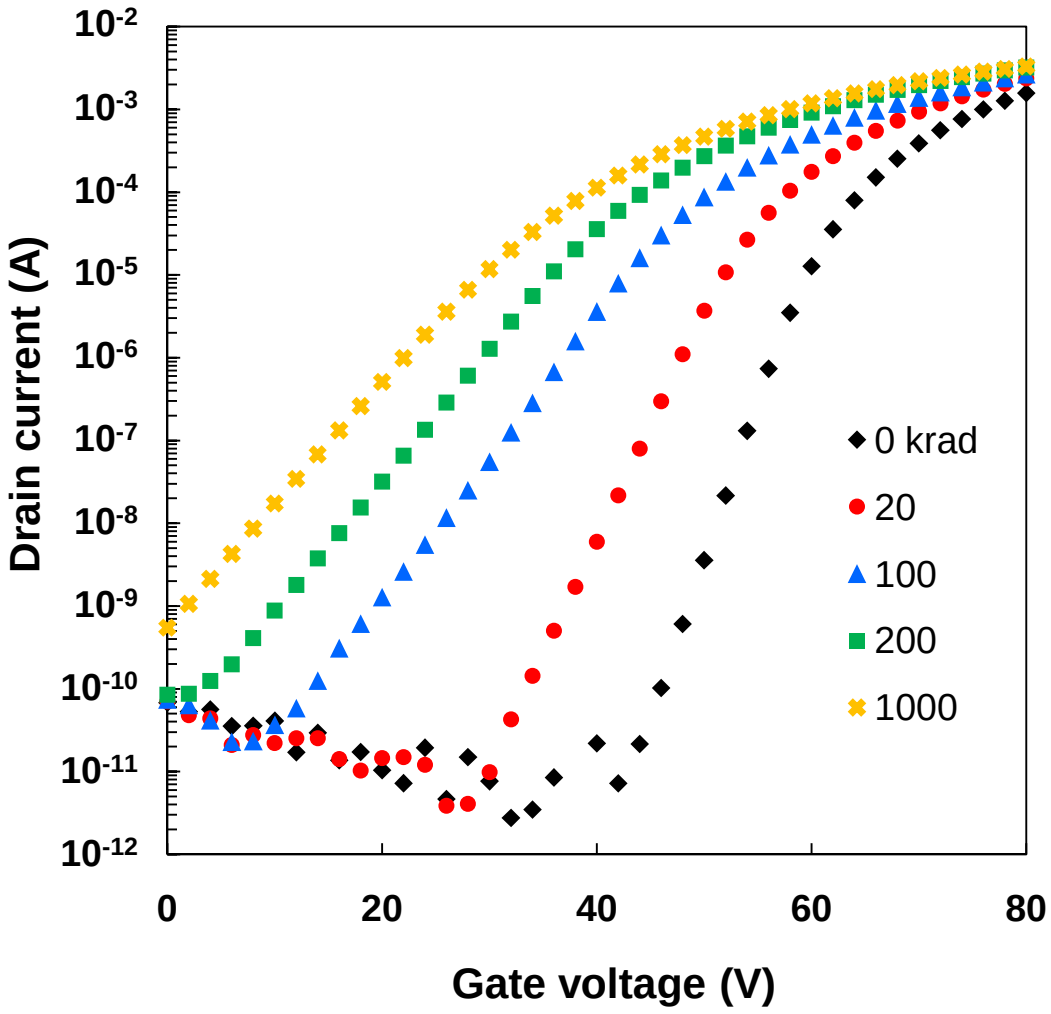

Fig. 3.6. I_d-V_{gs} characteristics before irradiation and after 20, 100, 200 and 1000 krad(SiO_2) of TID for NW FOXFET with W = 200 μm, L = 1.5 μm, V_d = 1 V, V_s = V_b = 0 V.

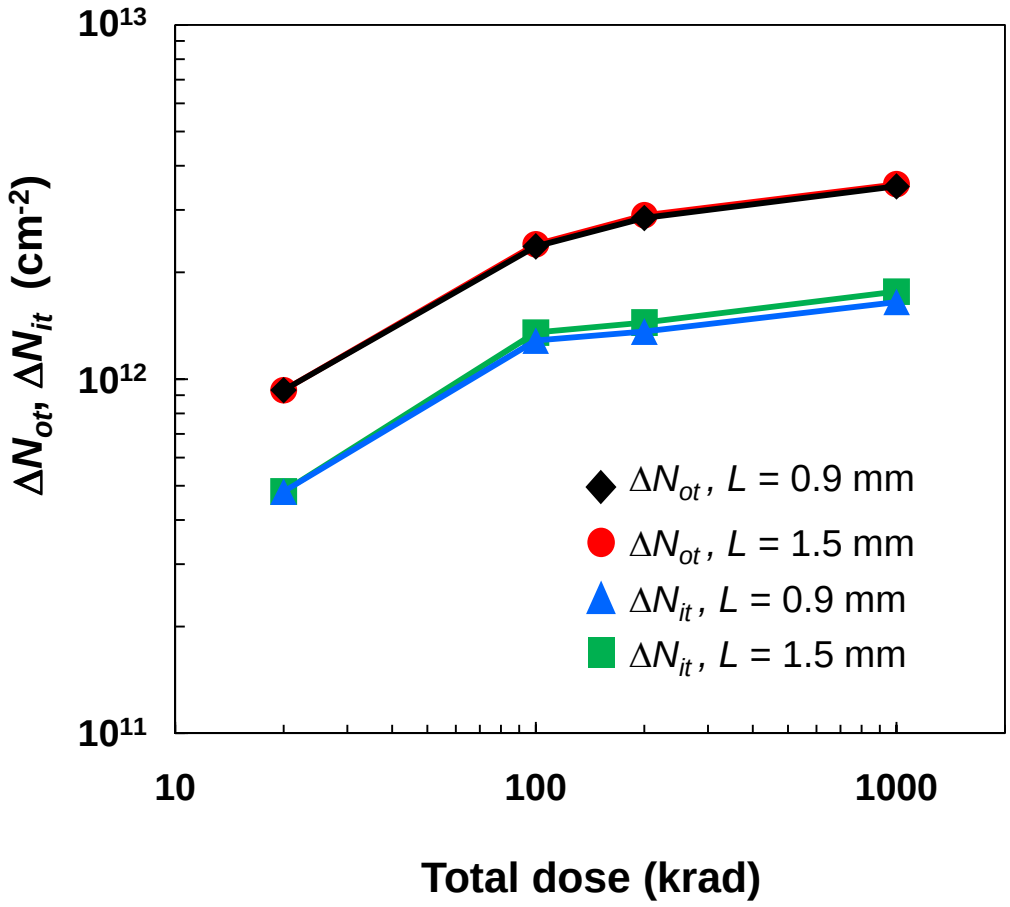

Fig. 3.7. N_{ot} and N_{it} extracted from the experimental data are plotted as a function of total dose for NW FOXFETS with L = 1.5 µm and L = 0.9 µm.

These results in Fig. 3.7 shows a similar buildup of N_{ot} and N_{it} as a function of dose for both devices (i.e., NW FOXFETs with L = 1.5 µm and L = 0.9 µm). These results also show that the rate of N_{ot} and N_{it} formation decreases as a function of dose as observed from the reduction in the slope. Several mechanisms can contribute to the behavior observed in the buildup of N_{ot} and N_{it}. For example, the density of trapped holes and interface traps becoming significant as compared to the number of defect precursors (i.e., hole traps in the oxide and passivated P_b centers at the Si-SiO_2 interface), and therefore, ΔN_{ot} and ΔN_{it} are reaching

saturation. Another mechanism that could contribute to this behavior is a space-charge effect that could retard (or invert) the flux of holes towards the interface where most precursors are located [21]. A third mechanism that could contribute to the reduction in the buildup rate for N_{ot} and N_{it} buildup rate is an enhancement in recombination of positively charged defects that occurs due to the confinement of electrons in the SiO_2 bulk at high dose levels [92, 105]. Following ionizing radiation exposure, the test structures were annealed at room temperature under the same biasing conditions (V_g = 1 V, with all other terminals grounded). I_d-V_{gs} characterization and defect density extractions were done after 2.5×10^5 s and 1.3×10^6 s of anneal time. The extractions of N_{ot} and N_{it} during irradiation and after room temperature anneal are plotted as a function of time in Fig. 3.8. The results in Fig. 3.8 show a measureable reduction in N_{ot} after room-temperature annealing, while N_{it} remains unchanged.

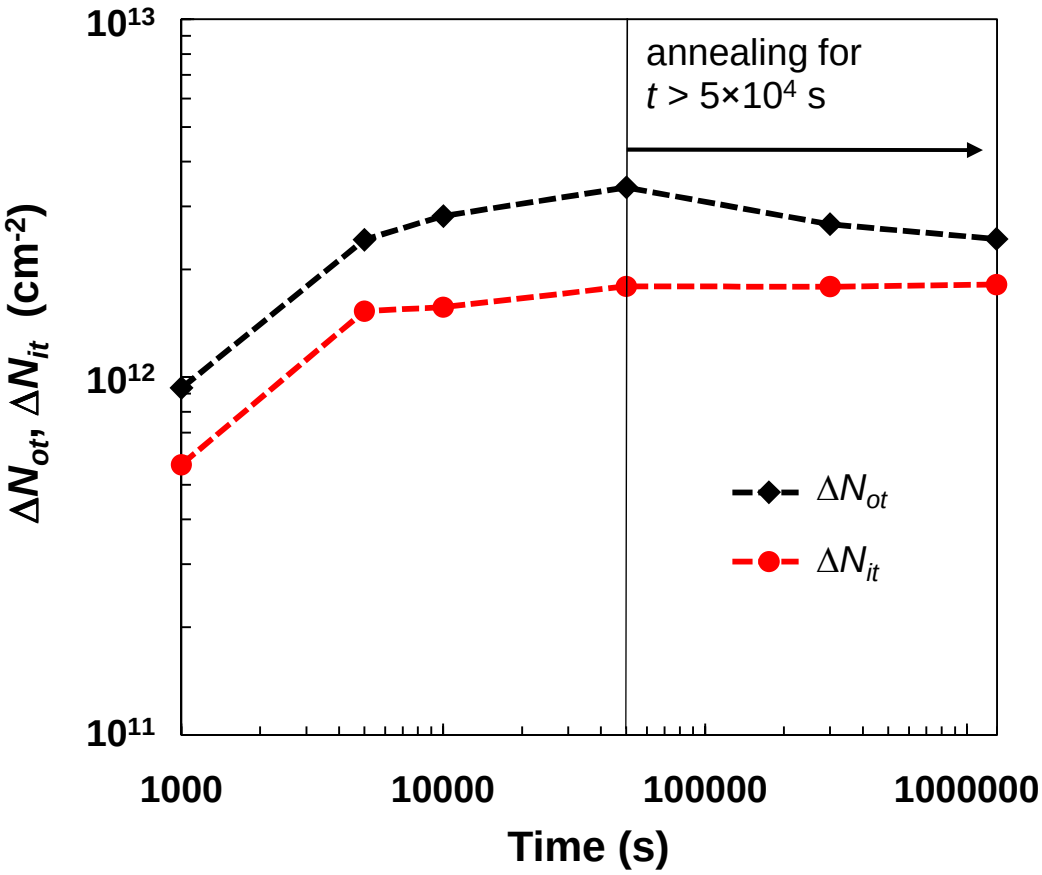

Fig. 3.8. N_{ot} and N_{it} during irradiation and following room temperature anneal plotted as a function of time dose for NW FOXFETS with L = 1.5 µm.

3.2 FOXFET Dose Rate Experiments

The enhanced low dose rate sensitivity (ELDRS) of bipolar junction transistors and linear bipolar circuits has been studied extensively since the phenomenon was first reported by Enlow *et al*. in 1991 [109]. The mechanisms governing ELDRS are reduced to three basic processes: space charge effects [110], carrier recombination and trapping, and proton release [111, 112]. It is commonly held that CMOS technologies are immune to enhanced degradation at low dose rates. However, the basis for this contention is questionable given that

none of the above processes are necessarily specific to bipolar technologies. In fact, two recent studies of dose rate effects in advanced CMOS technologies demonstrated an enhancement in the degradation at LDR as indicated by higher levels of edge leakage in n-channel devices [90, 91]. In [91], Johnston *et al.* described the implication of non-uniform field lines along the sidewall of STI oxides on specific mechanisms that contribute to the enhancement in edge leakage observed at low dose rates. The considered mechanisms are charge yield, hole transport and hole trapping. However, interface traps were not considered. As explained in Chapter 2 of this dissertation, it is possible to analyze the mechanisms contributing to the time-dependent buildup of N_{ot} and N_{it} in STI oxides without a significant effect from these non-uniformities at the trench sidewall and corner. This is possible by characterizing the time-dependent buildup of radiation-induced defects in FOXFET devices. This section of the dissertation reports experimental data from LDR and HDR experiments on the 90nm LSP NW FOXFET devices.

The FOXFET test structures were irradiated with ^{60}Co gamma rays at two different dose rates, 0.005 rad(SiO_2)/s and 100 rad(SiO_2)/s. During irradiation, the FOXFETs were biased with either 1 V at the gate or with the gate grounded. All other terminals were grounded for both configurations. The thickness of the FOXFET oxide is greater than 400 nm, thus the field in the dielectric is still relatively low (<25 kV/cm) even with the 1 V bias on the gate. Electrical measurements were performed prior to irradiation and following step-stress exposures up to total dose levels 3, 5, 10, 13.7 and 22.2 krad(SiO_2) for the LDR

and up to 10 and 20 krad(SiO_2) for the HDR. The electrical measurements consisted of measuring I_d vs. V_{gs} characteristics for a drain bias of V_d = 100 mV. The results for the LDR exposures are shown respectively in Figs. 3.9 and 3.10. The results in Fig. 3.9 are for the FOXFET with L = 1.5 µm and using a gate bias of 1 V during irradiation. On the other hand, the results in Fig. 3.10 are for a FOXFET with L = 0.9 µm but with a grounded gate during irradiation. Comparing the results in Figs. 3.8 and 3.9 indicate a similar buildup rate for N_{ot} and N_{it} between the devices exposed with V_g = 1 V and the devices exposed with a grounded gate, as evident from the similar response of the *I-V* characteristics. This is to be expected since, as mentioned above, the initial electric field of ~25 kV/cm when using V_g = 1 V is still relatively small to have an effect on prompt recombination mechanisms and therefore on the hole yield (see Fig. 1.4). Moreover, since these results are for a LDR exposure, sufficient time has been allowed to reach the final dose levels, therefore allowing transport of mobile species to be completed without a significant effect from the magnitude of the electric field.

The buildup of the effective oxide sheet-charge density (ΔN_{ot}) and interface trap density (ΔN_{it}) are extracted from the degraded *I-V* characteristics using the charge separation technique. Shown in Fig. 3.11 are the extractions of ΔN_{ot} and ΔN_{it} plotted as a function of dose for the LDR and the HDR experiments. The results in Fig. 3.11 are extracted from devices with L = 1.5 µm and exposed with a radiation bias of V_g = 1 V with all other terminals grounded. The extractions for

the case of a LDR are obtained from an average of 2 devices, while the HDR extractions are from a single device. Following HDR exposure, devices were annealed at room temperature with the same biasing configuration (i.e., V_g = 1 V with all other terminals grounded). The annealing time is determined by the time required to reach the total dose level (20 krad in this case) if devices were irradiated at the LDR. This way, the same amount of time is allowed for the transport of mobile species in both the LDR and HDR cases and "true" dose rate effects that depend on other mechanisms are revealed. True dose rate effects are determined by comparison between the radiation response of devices exposed at a LDR and devices exposed at a HDR and following room temperature anneal. The results in Fig. 3.11 show a greater buildup in both N_{ot} and N_{it} following the LDR exposures than following HDR exposure with the corresponding room temperature anneal. These results indicate that there is a LDR to HDR enhancement factor of approximately 1.40 for N_{ot} and approximately 1.85 for the case of N_{it}. These values are lower than the enhancement factor in damage for bipolar technologies which can be ~ 2 for N_{ot} and up to 10 for N_{it} [91, 105].

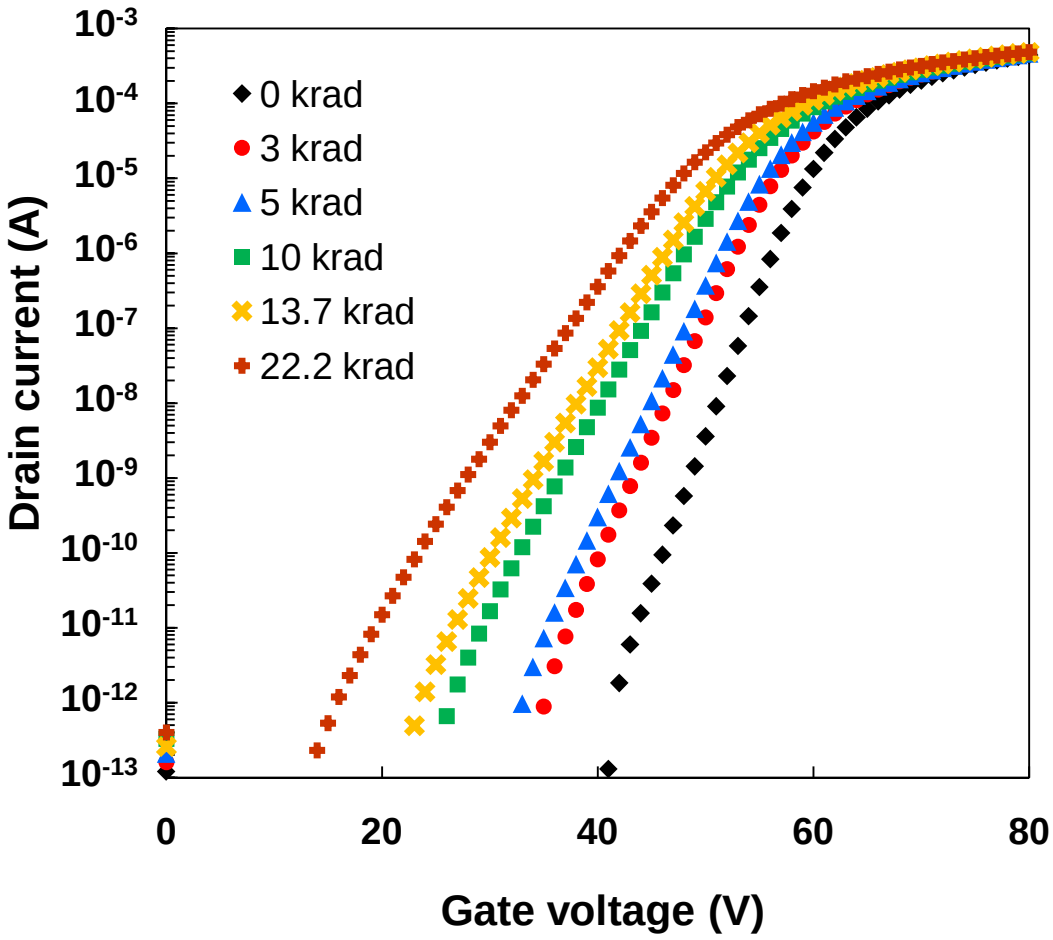

Fig. 3.9. I_d-V_{gs} characteristics before irradiation and after levels 3, 5, 10, 13.7 and 22.2 krad(SiO_2) of TID for NW FOXFET with W = 200 μm, L = 1.5 μm, V_d = 0.1 V, V_s = V_b = 0 V. Radiation bias was V_g = 1 V with all other terminals grounded. These results are for exposure at a LDR of 0.005 rad(SiO_2)/s.

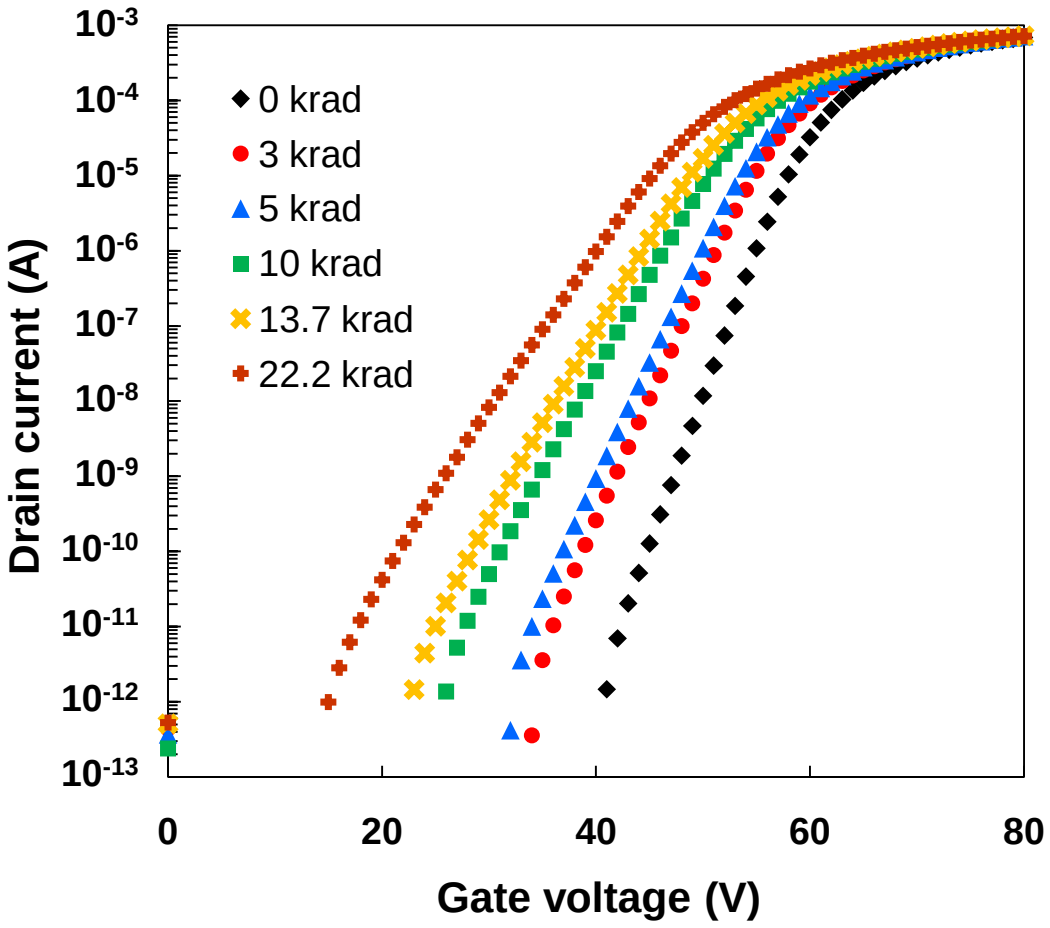

Fig. 3.10. I_d-V_{gs} characteristics before irradiation and after levels 3, 5, 10, 13.7 and 22.2 krad(SiO_2) of TID for NW FOXFET with W = 200 μm, L = 0.9 μm, V_d = 0.1 V, V_s = V_b = 0 V. All terminals were grounded during irradiation. These results are for exposure at a LDR of 0.005 rad(SiO_2)/s.

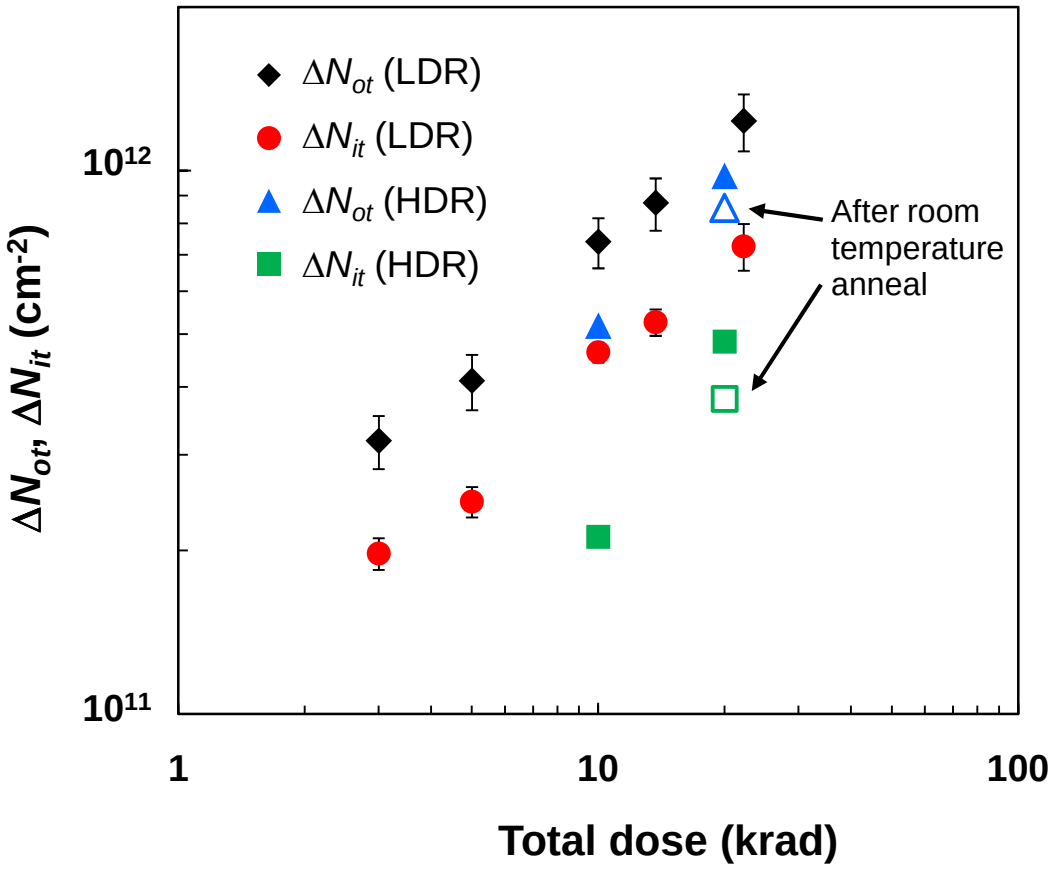

Fig. 3.11. ΔN_{ot} and ΔN_{it} plotted as a function of dose extracted from FOXFETs with W = 200 μm and L = 1.5 μm exposed at for 0.005 rad(SiO_2)/s (LDR) and at 100 rad(SiO_2)/s (HDR) using a 1 V bias on the gate during irradiation.

3.3 Experimental Results for MOS Capacitors

MOS capacitors were fabricated at Arizona State University with 200 nm thermal oxides grown on n-type Si wafers through a wet oxidation process at 1050 ˚C. The capacitors were exposed to several total dose levels of gamma rays using a stepped stress approach at three different dose rates, 20 rad(SiO_2)/s, 13.4 rad(SiO_2)/s and 0.017 rad(SiO_2)/s. Capacitance vs. voltage (*C*-*V*) in-situ characterization was performed immediately after irradiating to each TID level

with the devices kept at room temperature. The bias condition during irradiation was a gate voltage (V_g) of 5 V, 1 V or 0 V, with a grounded substrate. Shown in Fig. 3.12 are the normalized capacitances (average of seven MOS capacitors) obtained as a function of gate voltage (V_g) before irradiation and after exposure to 23, 113 and 279 krad(SiO_2). These results are for MOS capacitors exposed at a dose rate of 20 rad(SiO_2)/s with a 5 V bias at the gate. The results in Fig. 3.12 are obtained by sweeping the gate voltage from the most negative voltage to 0 V (e.g., –30 – 0 V) using a ramp rate of 5 V/s and a 100 mV ac signal at a frequency of 1 MHz. This gate voltage sweep will change the condition at the semiconductor surface from strong inversion to accumulation. An increase in N_{ot} is manifested in the measurements through the negative shifts of the *C*-*V* curves. The stretch-out observed in the *C*-*V* curves at higher dose levels is evidence of an increase in the interface trap density.

Interface traps do not contribute additional capacitance since they cannot follow the high frequency ac signal. However, there is still a stretch-out in the *C*-*V* characteristics since they can follow the slowly varying dc bias and can contribute additional gate charge. The distortion of the post-irradiation *C*-*V* curves in Fig. 3.12 is therefore not the result of excess capacitance due to interface traps, but rather the result of a stretch-out along the gate voltage axis [103]. Extractions of ΔN_{it} and ΔN_{ot} are performed by comparing theoretical and actual deep-depletion *C*-*V* curves [108, 113]. As described in [113], the comparison yields an energy distribution which represents the increase of the interface trap density and is denoted by $\Delta D_{it}(E)$ [$cm^{-2}eV^{-1}$]. The increase in the total number of interface

states that contribute charge (i.e., ΔN_{it}) can then be obtained by integrating these distributions over the appropriate energy range as

$$\Delta N_{it} = \int \Delta D_{it}(E)dE\,. \tag{3.1}$$

Alternatively, the distribution of interface states can be expressed as a function of the surface potential (ψ_s) as $\Delta D_{it}(\psi_s)$ with units of [$cm^{-2}V^{-1}$], and ΔN_{it} is given by

$$\Delta N_{it} = \int \Delta D_{it}(\psi_s)d\psi_s\,. \tag{3.2}$$

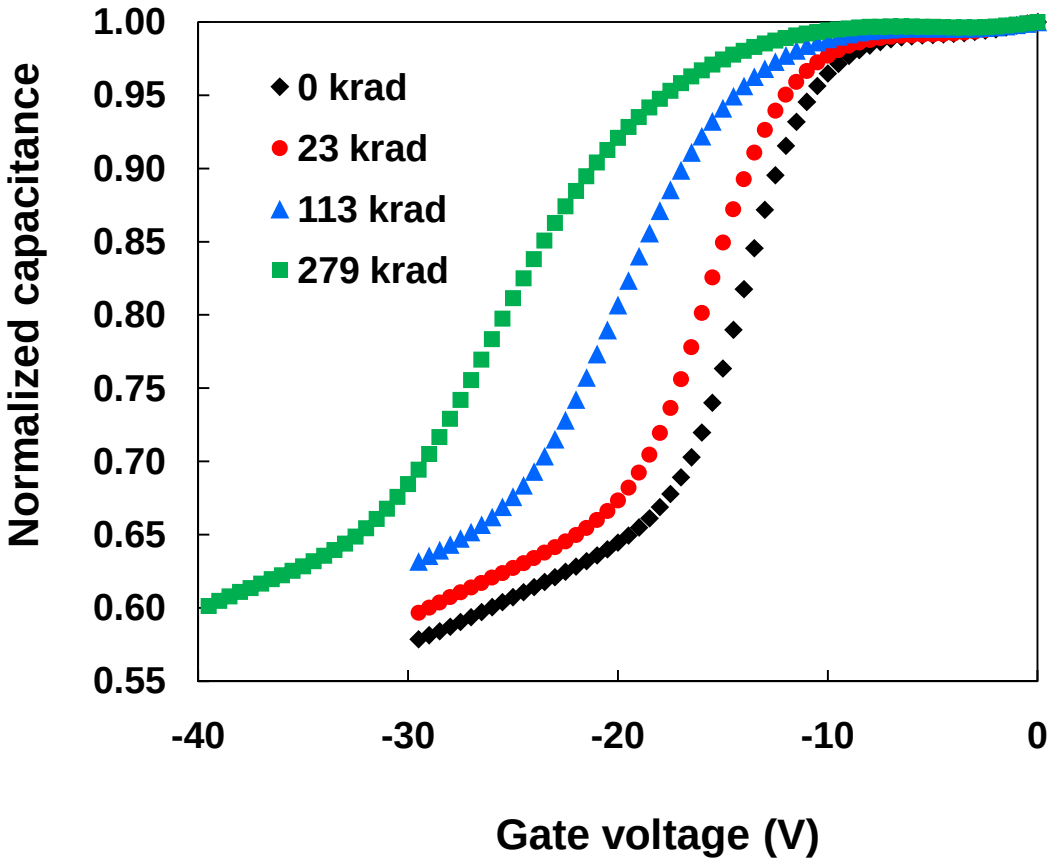

Fig. 3.12. Normalized capacitances plotted as a function of gate voltage (V_g) before irradiation and after exposure to 23, 113 and 279 krad(SiO_2) for a dose rate of 20 rad(SiO_2)/s with a 5 V bias at the gate during irradiation.

The charge-separation technique [108] allows quantifying the contribution of interface traps to the net threshold voltage shifts as measured from the stretch-out of the *I-V* characteristics of irradiated transistors (or from the stretch-out of the *C-V* characteristics of irradiated MOS capacitors) between mid-gap and inversion. Extractions of ΔN_{it} and ΔN_{ot} using the charge-separation technique are given in this section of the dissertation. These extractions will provide a good estimate of $\Delta D_{it}(\psi_s)$ integrated within the mid-gap and inversion voltage range, but will not provide information on the distribution itself. As described in several other studies, the distribution of radiation-induced interface traps is non-uniform within the Si bandgap [114-116]. Therefore, an analytical description of the radiation response of *C-V* and *I-V* characteristics requires modeling the $V_g(\psi_s)$ dependence for the case of non-uniform $D_{it}(\psi_s)$. The derivation that leads to obtaining such dependence for the different distributions of $D_{it}(\psi_s)$ is presented in Chapter 4.

Shown in Fig. 3.13 are the extracted values for ΔN_{it} and ΔN_{ot} plotted as a function of total dose. These results are obtained from the degraded *C-V* curves plotted in Fig. 3.12. The extractions are the average of 8 measurements, and error bars show a standard deviation in the extractions of ΔN_{ot} and ΔN_{it}. The results in Fig. 3.14 reveal an approximately linear dependence in the buildup of ΔN_{ot} and ΔN_{it} with dose. Additional experiments at a LDR provide information on dose-rate effects in the buildup of radiation-induced defects in thermally grown oxides. Shown in Fig. 3.14 is a plot of ΔN_{ot} and ΔN_{it} plotted as a function of total dose obtained from the degraded *C-V* characteristics of MOS capacitors exposed at

dose rates of 13.4 rad(SiO_2)/s and 0.017 rad(SiO_2)/s. True dose rate effects are observed by following the HDR exposures with room temperature anneal. The results in Fig. 3.14 show a clear enhancement in the buildup of interface traps following LDR exposure up to 40 krad(SiO_2) with respect to ΔN_{it} after HDR exposure up to 50 krad(SiO_2) plus room temperature anneal. The enhancement factor at 50 krad(SiO_2) would be ~5 if ΔN_{it} continues increasing at a similar rate. For the case of N_{ot}, the enhancement would be approximately between 1 and 2.

In the experimental data presented in this chapter of the dissertation, an enhanced degradation following LDR irradiation has been observed for both FOXFETs and MOS capacitors (i.e., in STI and thermally grown oxides respectively). The total dose and dose rate characterization of these devices was performed using typical laboratory gamma ray sources (i.e., ^{60}Co for the FOXFET experiments and ^{137}Cs for the LDR MOS capacitor experiments). As described in [117], skepticism about ELDRS effect for actual space environments (electrons and protons) has been removed with a space experiment on board the microelectronics and photonics test bed (MPTB) [117-119]. In the MPTB ELDRS experiment, degradation of the input bias current for different bipolar linear circuits (e.g., the LM139 voltage comparator) has shown a significant enhancement compared to HDR ground tests on samples from the same lot. Shown in Fig. 3.15 are the MPTB experimental data for input bias current as a function of total dose compared to the ground data at several dose rates.

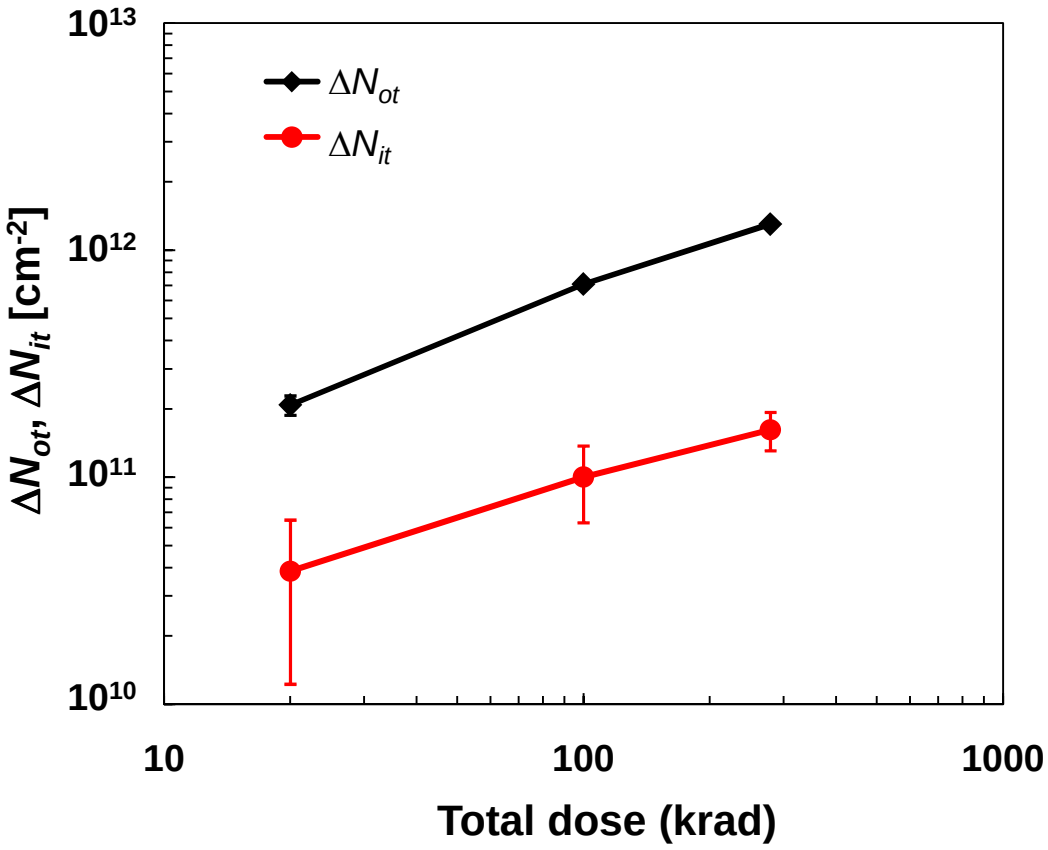

Fig. 3.13. ΔN_{it} and ΔN_{ot} plotted as a function of total dose. These results are obtained from the degraded *C*-*V* curves plotted in Fig. 3.12. The extractions are the average of 8 measurements, and error bars show one standard deviation.

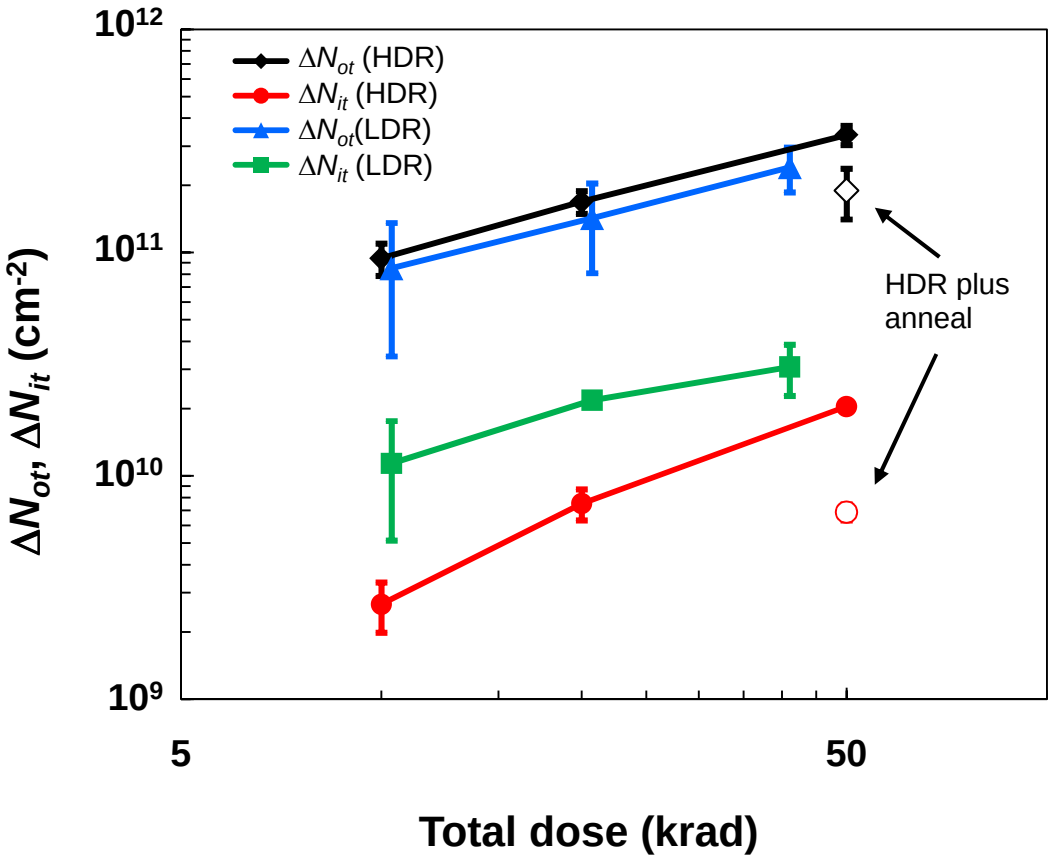

Fig. 3.14. ΔN_{ot} and ΔN_{it} plotted as a function of total dose obtained from the degraded *C-V* characteristics of MOS capacitors exposed at dose rates of 13.4 rad(SiO_2)/s and 0.017 rad(SiO_2)/s. Error bars show one standard deviation. Open symbols are for room temperature anneal following the HDR exposures.

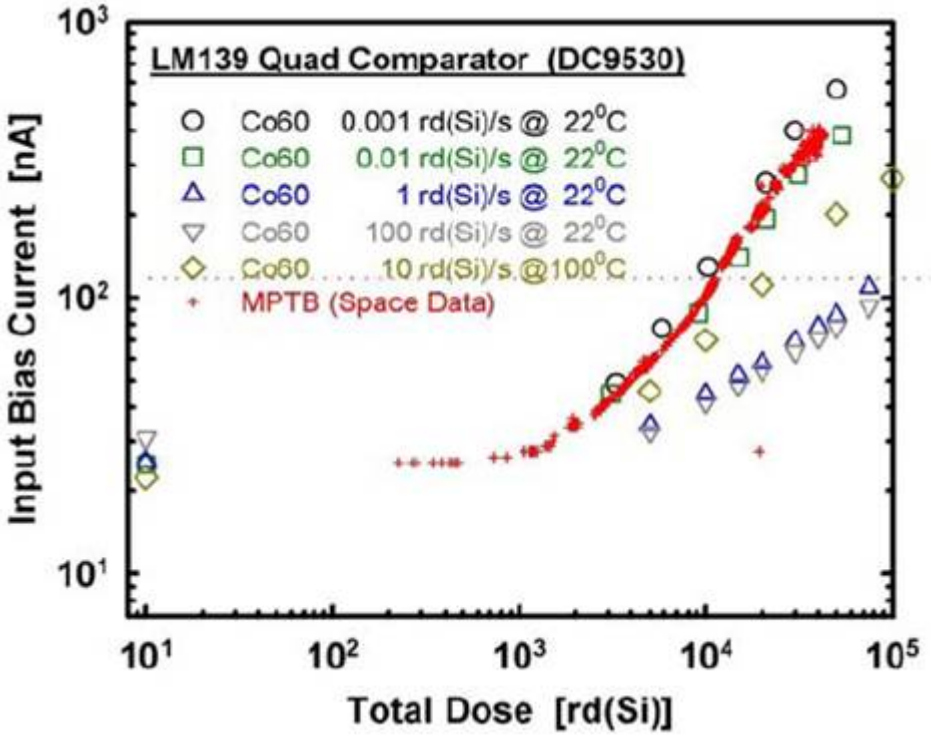

Fig. 3.15. LM139 quad comparator input bias current vs. total dose for MPTB experiment compared to ground test data at several fixed dose rates [117-119].

CHAPTER 4. MODELING IONIZING RADIATION EFFECTS

4.1 Modeling the Buildup of Radiation Induced Defects in STI Oxides

This section of the dissertation, discusses numerical calculations for the time-dependent buildup of N_{ot} and N_{it} in STI oxides of deep-submicron CMOS technologies. The calculations presented here are obtained through an experimental parameterization of the model and provide insight on key mechanisms impacting time-dependent buildup of N_{ot} and N_{it}. Because of its predictive nature, a proper parameterization of the model will allow extrapolating the calculations to higher doses and to different dose rates. Therefore, the results obtained from the physical model can support the formulation of analytical models for the buildup of N_{ot} and N_{it}. Derivations for the analytical descriptions of ΔN_{ot} and ΔN_{it} are also presented in this chapter of the dissertation. The analytical models for ΔN_{ot} and ΔN_{it} are obtained using general equations that describe the generation, transport and trapping of holes as well as the reaction of holes with hydrogenated defects resulting in the release of protons and subsequent formation of interface traps. When used in conjunction with closed-form expressions for surface potential, the analytical models enable an accurate description of radiation-induced degradation of transistor electrical characteristics. This chapter of the dissertation describes the incorporation of radiation-induced defect densities into surface potential calculations. These calculations allow modeling the $V_g(\psi_s)$ dependence for the case of non-uniform distributions of interface traps,

i.e., $D_{it}(\psi_s)$, and thus, modeling the radiation response of *C-V* and *I-V* device characteristics.

Prior to obtaining analytical models for the buildup of ΔN_{ot} and ΔN_{it}, the mechanisms contributing to the radiation-induced degradation of deep-submicron technologies are investigated through experimental parameterization of the physical model presented in Chapter 2. Model parameters are adjusted to simulate the buildup of ΔN_{ot} and ΔN_{it} in the STI oxides of the NW FOXFETs fabricated in a 90 nm commercial CMOS process for which experimental results are presented in Chapter 3. Shown in Fig. 4.1 is a plot comparing ΔN_{ot} and ΔN_{it} obtained experimentally for the NW FOXFET exposed at a LDR of 0.005 rad(Si)/s under a 1 V gate bias (symbols) with the model calculations (solid lines). These calculations are for a uniform density of hydrogenated defects, i.e. $N_{T2} = 5\times10^{16}$ cm^{-3}, distributed throughout the oxide and for a uniform density of hole traps located within 30 nm of the Si-SiO_2 interface, i.e., $N_{T1} = 5\times10^{16}$ cm^{-3}. Other model parameters used for these calculations are listed in Table. 4.1. As shown in the results plotted in Fig. 4.1, the model reasonably describes the buildup of N_{ot} and N_{it}. The calculations shown in Fig. 4.1 demonstrate that ΔN_{ot} and ΔN_{it} increase approximately linearly with dose followed by a reduction (or saturation) in the rate of increase. The experimental data shown in Fig. 4.1 for NW FOXFETs obtained up to 22 krad(SiO_2) falls in the linear range.

Additional model calculations are compared to the experimental data obtained from NW FOXFETs irradiated at HDR of 20 rad(SiO_2)/s up to higher

total dose levels and plotted in Fig. 4.2. In these results, saturation in the buildup of N_{ot} and N_{it} is better characterized. However, the buildup of N_{it} described by the model is rather lower than the actual values obtained experimentally for the HDR exposure and no annealing. The discrepancies in the simulated and measured ΔN_{it} may be due to a prompt buildup of interface traps that is not described by the slower two-stage process considered in the calculations. The prompt formation of interface traps is discussed in [66, 67], and is assumed related to a relatively fast field-dependent effect that correlates with the arrival of holes to the Si-SiO_2 interface. However, many of the experimental studies have confirmed that the largest effect accounting for ~ 90% of the total interface trap buildup is the two-stage process described in the McLean model [34, 46, 63-65]. Discrepancies in the simulated and experimentally extracted values for N_{it} could also be due to the fact that most traps accounted for as interface states may actually be border traps (i.e., switching oxide traps) located near the interface. Therefore, since border traps will most likely anneal at room temperature (and interface traps will not), the comparison should be done with the values of N_{it} extracted following room temperature anneal which should mostly account for true interface states.

Notice that for the calculations in Fig. 4.2, the solutions are obtained up to a total time required to reach a dose of 1 Mrad(SiO_2) at the HDR of 20 rad(SiO_2)/s, which does not allow for complete proton transport and interface trap formation. Moreover, the investigation of true dose rate effects in simulation (see Fig. 2.12) is achieved by advancing the numerical solutions for HDR to larger times (i.e. the time required to reach the same total dose in the lowest dose rate calculation)

allowing the transport of protons and contribution to the formation of N_{it} to be complete. For example, the calculations in Fig. 2.12 for all dose rates are done up to the same time required to reach a 50 krad(SiO_2) for the a dose rate of 10^{-5} rad(SiO_2)/s. However, the radiation-induced generation of ehps for each of the dose rate calculations is stopped after the total dose of 50 krad(SiO_2) is obtained (e.g., after 5000 seconds for a dose rate of 10 rad(SiO_2)/s).

Shown in Fig. 4.3 are the model calculations of ΔN_{it} as a function of dose rate for both the NW FOXFETs and the MOS capacitors compared to experimental results obtained at two different dose rates. These results are for a total dose of 22 krad(SiO_2) for FOXFETs and 40 krad(SiO_2) for the MOS capacitors (HDR results for capacitors are at 50 krad(SiO_2) plus room temperature anneal). The results in Fig. 4.3 show reasonable agreement between the physical model and the experimental results. These results also demonstrate that calculations of N_{it} at HDR allowing sufficient time for proton transport towards the interface results in better agreement with the experimental results even at a HDR of 100 rad(Si)/s. The robustness of the model is demonstrated by the proper description of the different dose rate response for FOXFETs and MOS capacitors. The model parameters used to obtain these calculations are summarized in Table 4.1 for both kinds of oxides (i.e. STI oxides in the FOXFETs and thermally grown oxides in the MOS capacitors). Model parameters listed in Table 4.1 are used to obtain the fits in Fig. 4.1, 4.2 and 4.3 for the FOXFET devices and suggest that hole traps are most likely located within 30 nm of the Si-SiO_2 interface, with densities in the order of 10^{19} cm^{-3}. The distribution of hydrogenated defects is unknown and the

model assumes a uniform distribution with concentrations in the order of 10^{16} cm^{-3} resulting in a reasonable agreement with the experimental data. These calculations also suggest that the densities of passivated dangling bonds at the Si-SiO_2 interface (i.e., N_{P_bH}) in STI oxides of deep-submicron technologies are in the order of 10^{13} cm^{-2}.

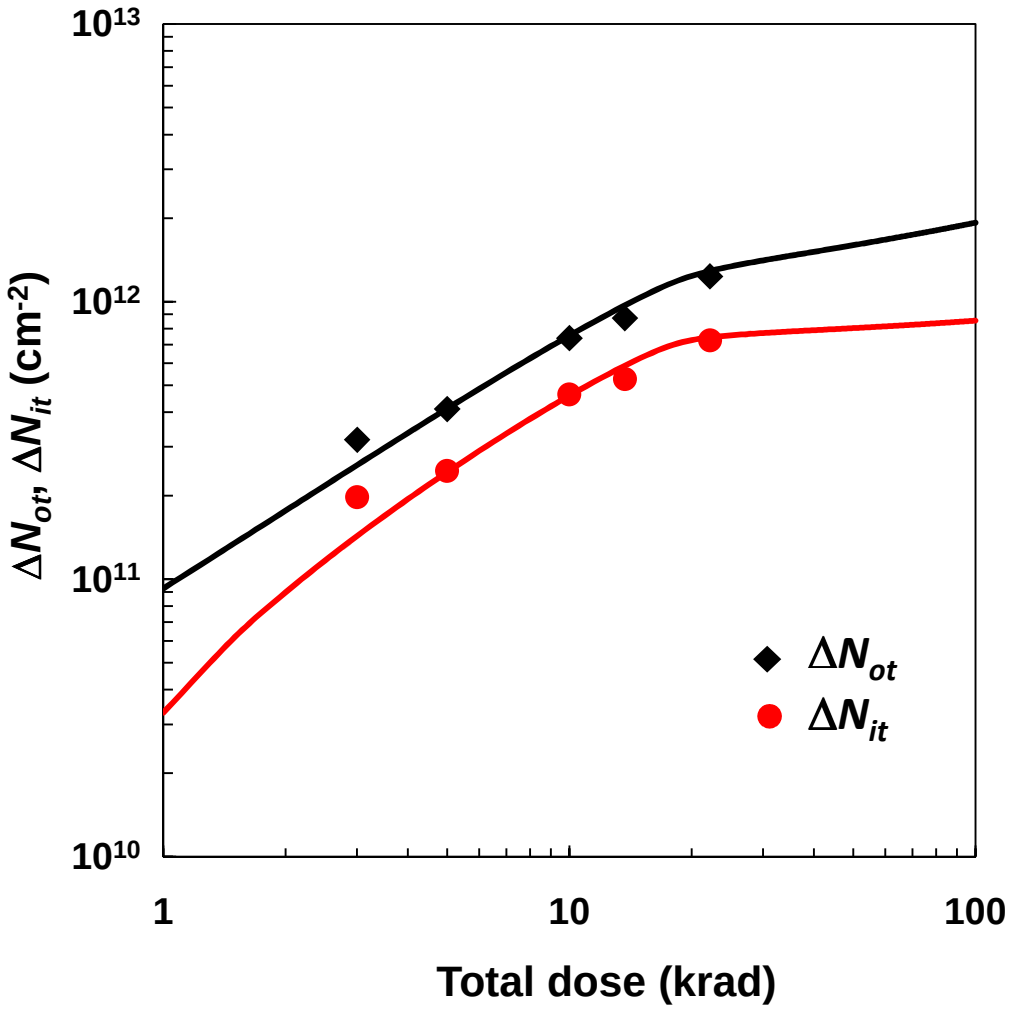

Fig. 4.1. Comparison of ΔN_{ot} and ΔN_{it} vs. total dose obtained experimentally for the NW FOXFET exposed at a LDR of 0.005 rad(Si)/s under a 1 V gate bias (symbols) with the model calculations (solid lines).

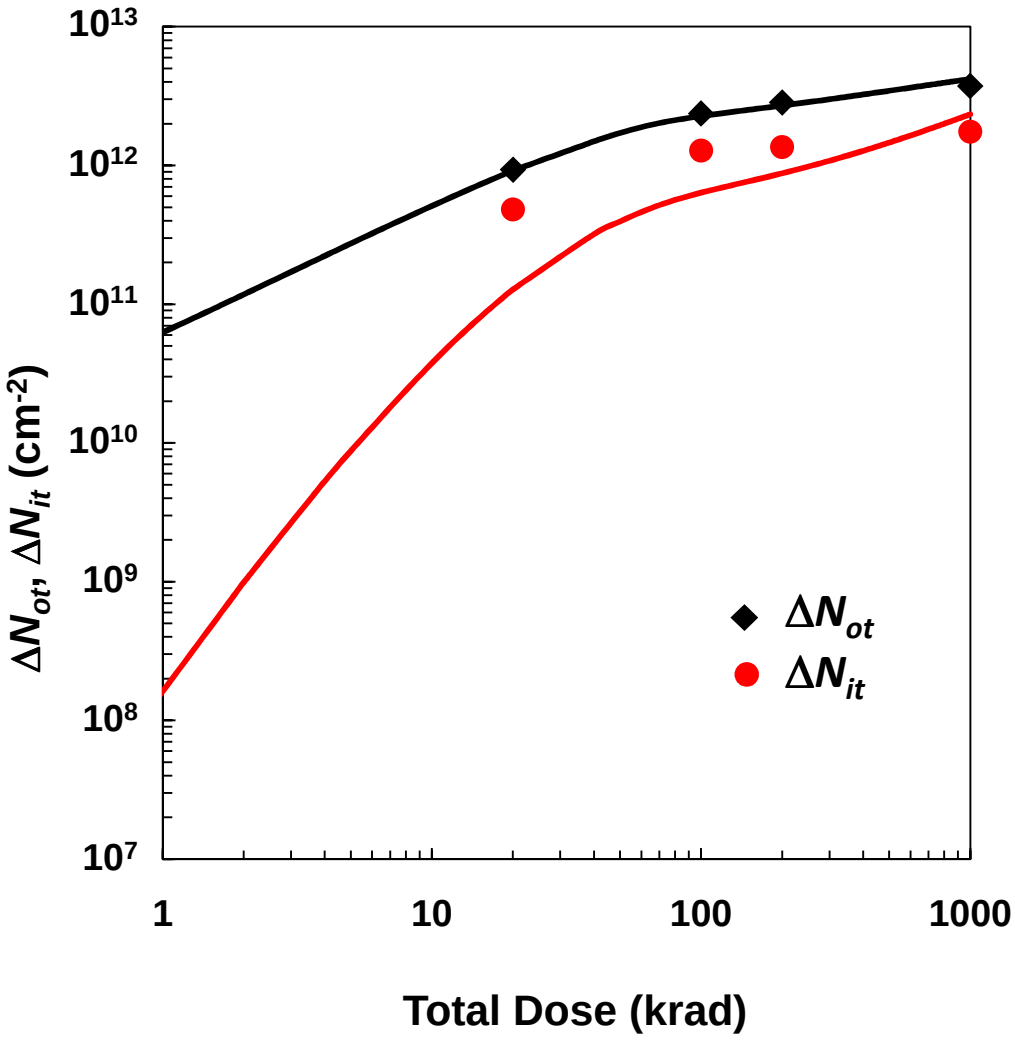

Fig. 4.2. Comparison of ΔN_{ot} and ΔN_{it} vs. total dose obtained experimentally for the NW FOXFET exposed at a HDR of 20 rad(SiO_2)/s under a 1 V gate bias (symbols) with the model calculations (solid lines).

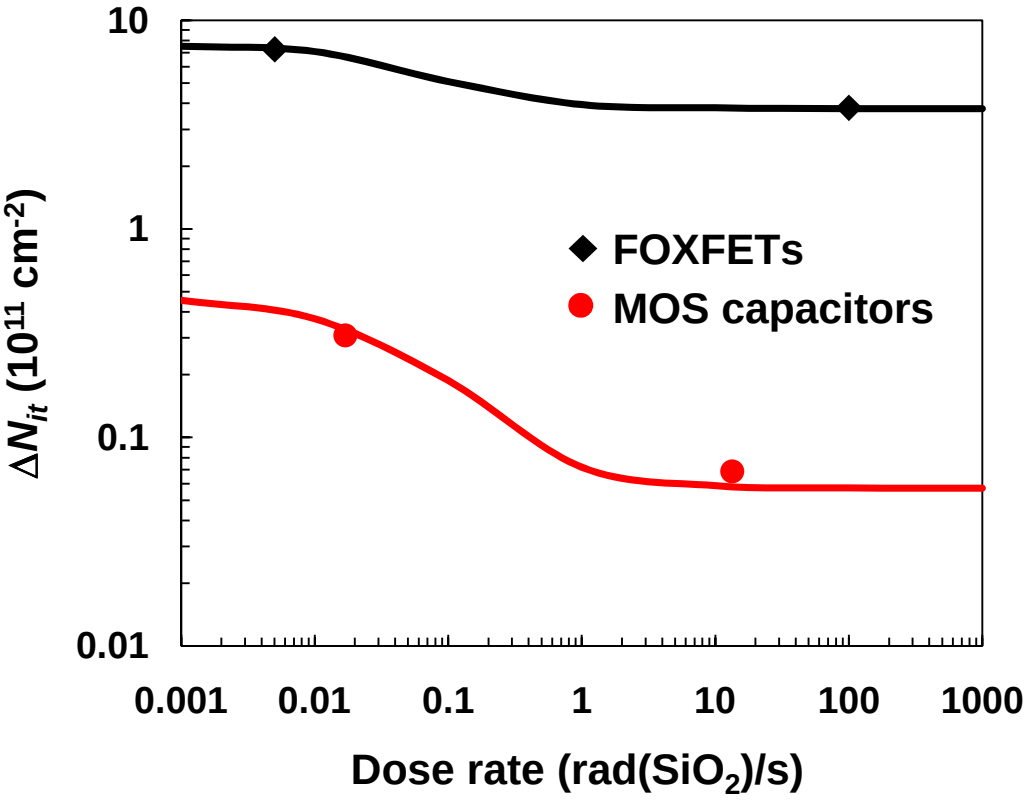

Fig. 4.3. Comparison of model calculations (solid lines) and experimental results (symbols) for ΔN_{it} vs. dose rate for NW FOXFET and for the MOS capacitors.

TABLE 4.1
SUMMARY OF MODEL PARAMETERS USED IN SIMULATIONS FOR ΔN_{it} AND ΔN_{ot} IN FIGS. 4.1, 4.2 AND 4.3

Parameter	Symbol	Value (FOXFET)	Value (Capacitor)	Units
Oxide thickness	t_{ox}	425	200	nm
Location of deep hole traps (measured from Si-SiO_2 interface)	x_2	25–30	25	nm
Hole trap density	N_{TA}	1.3×10^{19}	2.0×10^{18}	cm^{-3}
Hydrogenated defect density	N_{TB}	1.2×10^{16}	1.0×10^{15}	cm^{-3}
Densities of passivated dangling bonds at the Si-SiO_2 interface	N_{P_bH}	1.0×10^{13}	5.0×10^{12}	cm^{-3}
Capture cross-sections for holes at hole traps	σ_{pta}	5.5×10^{-14}	5.5×10^{-14}	cm^2
Capture cross-sections for holes at hydrogenated defects	σ_{ptb}	5.0×10^{-14}	5.0×10^{-14}	cm^2
Capture cross-sections for electrons at positively charged defects	σ_{npta}	5.0×10^{-13}	5.0×10^{-13}	cm^2
Capture cross-sections for electrons at positively charged hydrogenated defects	σ_{nptb}	2.0×10^{-12}	1.0×10^{-11}	cm^2
Capture cross-sections for protons at passivated P_b-centers	σ_{it}	1.0×10^{-11}	1.0×10^{-11}	cm^2
Coefficient for hole emission	r_{ptd}	1.0×10^{-11}	1.0×10^{-11}	s^{-1}
Coefficient for proton release	r_{pth}	1.0×10^{-5}	1.0×10^{-5}	s^{-1}

4.2 Surface Potential Calculations

The radiation-induced degradation on the *I-V* characteristics of transistors and the *C-V* characteristics of MOS capacitors is modeled using a surface potential based approach. In this approach, the effects of N_{ot} and N_{it} on ψ_s are modeled through an implicit equation for ψ_s which can be solved numerically as a

function of bias and the radiation-induced defect parameters. By Gauss' theorem of electrostatics, the semiconductor charge per unit area is given by

$$Q_s = -\epsilon_s E_s = -\text{sgn}(\psi_s) Q_0 \sqrt{H(\beta\psi_s)}, \tag{4.1}$$

where ϵ_s is the semiconductor permittivity, E_s is the surface electric field obtained from the integration of the Boltzmann-Poisson equation and

$$Q_0 = \sqrt{2q\epsilon_s \phi_t N_a}. \tag{4.2}$$

In (4.1) and (4.2), q is the electronic charge, ϵ_s is the semiconductor permittivity, ϕ_t is the thermal voltage, N_a is the doping concentration and $\beta = 1/\phi_t$. Function $H(\beta\psi_s)$ in (4.1) is given by [120, 121]

$$H(\beta\psi_s) = (e^{-\beta\psi_s} + \beta\psi_s - 1) + e^{-\beta(2\phi_b + \phi_n)}(e^{\beta\psi_s} - \beta\psi_s - 1), \tag{4.3}$$

where ϕ_n is the split in the quasi-Fermi potentials (or imref splitting), and $\phi_b = \phi_t \ln(N_a/n_i)$ is the bulk potential. The dependence of ψ_s on V_g is obtained through the surface electric field given by

$$E_s = \frac{\epsilon_{ox}}{\epsilon_s} E_{ox} = \frac{\epsilon_{ox}}{\epsilon_s t_{ox}} V_{ox} = \frac{\epsilon_{ox}}{\epsilon_s t_{ox}} (V_g - V_{fb} - \psi_s). \tag{4.4}$$

Solving for E_s from (4.1) and substituting back into (4.4) results in the following relation, which is referred to as the surface potential equation (SPE):

$$V_g - V_{fb} - \psi_s = \gamma\, \text{sgn}(\psi_s) \sqrt{\phi_t H(\beta\psi_s)}. \tag{4.5}$$

In (4.5), γ is the body factor and is given by

$$\gamma = \frac{\sqrt{2q\epsilon_s N_a}}{C_{ox}}. \tag{4.6}$$

The interface trap charge $Q_{it}(\psi_s) = -qN_{it}(\psi_s)\cdot\mathrm{sgn}(\psi_s - \phi_b)$ and oxide trapped charge $Q_{ot} = qN_{ot}$ will induce charge inside the semiconductor and will correspondingly alter the flat-band voltage through the relation [103]

$$V_{fb} = \Phi_{MS} - \frac{Q_{it}(\psi_s)}{C_{ox}} - \frac{Q_{ot}}{C_{ox}}, \tag{4.7}$$

where Φ_{MS} is the gate-to-semiconductor workfunction difference. Interface trap charge $Q_{it}(\psi_s)$ will be positive for $\psi_s < -\phi_b$ since empty donor-like interface states contribute positive charge and negative for $\psi_s > -\phi_b$ since filled acceptor-like interface traps contribute negative charge. By substituting (4.7) back into (4.5) we obtain the modified form of the SPE:

$$V_g - \Phi_{MS} + \frac{qN_{ot}}{C_{ox}} - \frac{qN_{it}(\psi_s)}{C_{ox}}\mathrm{sgn}(\psi_s + \phi_b) - \psi_s = \gamma\ \mathrm{sgn}(\psi_s)\sqrt{\phi_t H(\beta\psi_s)}. \tag{4.8}$$

Alternatively,

$$V_g - \Phi_{MS} + \phi_{nt} - \psi_s = \gamma\ \mathrm{sgn}(\psi_s)\sqrt{\phi_t H(\beta\psi_s)}. \tag{4.9}$$

In (4.9), the radiation-induced defect densities (i.e., N_{ot} and N_{it}) are integrated into the defect potential parameter (ϕ_{nt}) given by

$$\phi_{nt} = \frac{q}{C_{ox}}\left[N_{ot} - D_{it}(\psi_s - \phi_b)\right], \tag{4.10}$$

where $qD_{it} = N_{it}/\phi_b$ is the energy distribution of interface traps density with units of [$cm^{-2}eV^{-1}$]. However, (4.10) only applies for a uniform distribution of interface traps throughout the Si bandgap. It is convenient to express the modified SPE as

$$\left(V_g - \Phi_{MS} + \phi_{nt} - \psi_s\right)^2 = \gamma^2 \phi_t H(\beta\psi_s). \tag{4.11}$$

The surface potential can be calculated as a function of bias and the radiation-induced defect parameters by numerically solving (4.11). Shown in Fig. 4.4 are solutions to ψ_s as a function of V_g for values of N_{ot} and N_{it} extracted experimentally for the NW FOXFETs (see Fig. 3.7). The inset in Fig. 4.4 is a plot of ϕ_{nt} as a function of V_g for the same values of N_{ot} and N_{it}. Other device parameters used for these computations are $N_a = 7.4\times10^{17}$ cm^{-3}, $t_{ox} = 425$ nm, $\Phi_{MS} = -0.9985$ V, $V_d = 0.1$ V and $V_s = V_b = 0$ V.

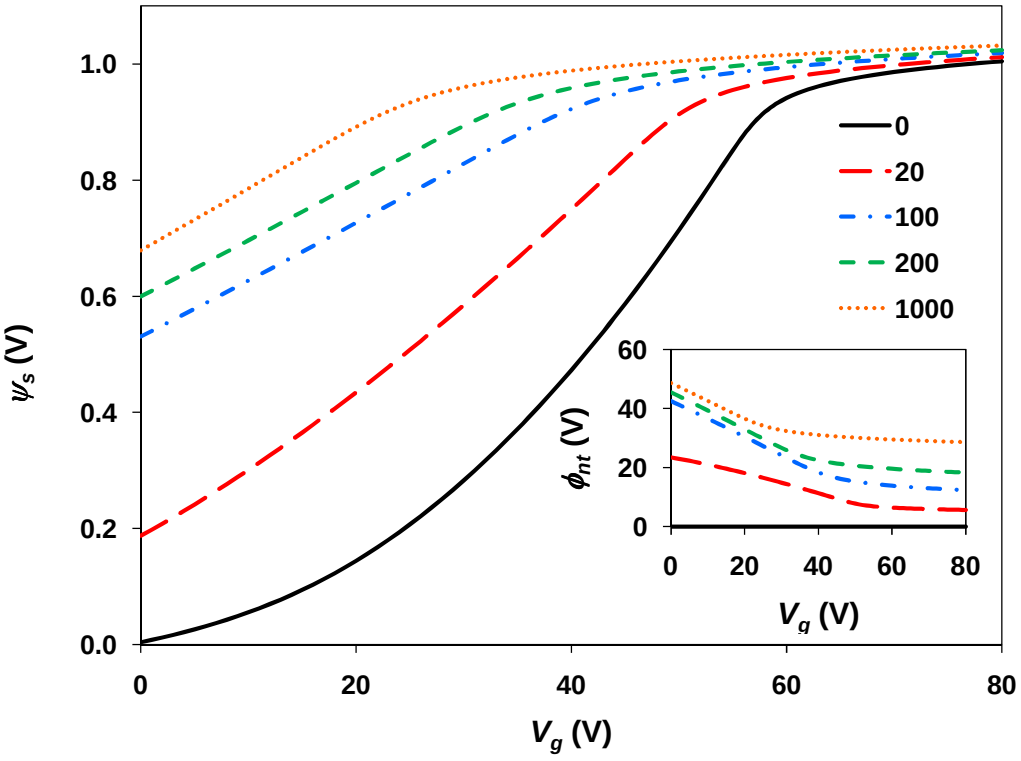

Fig. 4.4. Surface potential (ψ_s) plotted as a function of gate voltage (V_g) for different values of N_{ot} and N_{it} extracted from the data. Inset shows the defect potential (ϕ_{nt}) as a function of gate voltage for the same values of N_{ot} and N_{it}.

In some cases, an accurate analytical description of the radiation-response on *I-V* and *C-V* characteristics requires modeling the $V_g(\psi_s)$ dependence for the case of non-uniform D_{it}. The following derivation leads to obtaining such dependence for the case of three different distributions of $D_{it}(\psi_s)$: 1) uniform; 2) piecewise linear; and 3) piecewise quadratic. The derivation will be verified experimentally by comparison with the degraded *C-V* characteristics of the n-type MOS capacitors reported in Chapter 3. Shown in Fig. 4.5 are the three different distributions of $D_{it}(\psi_s)$ considered in the derivation plotted as a function of

surface potential and energy within the Si bandgap. The negative surface potentials indicate an n-type semiconductor.

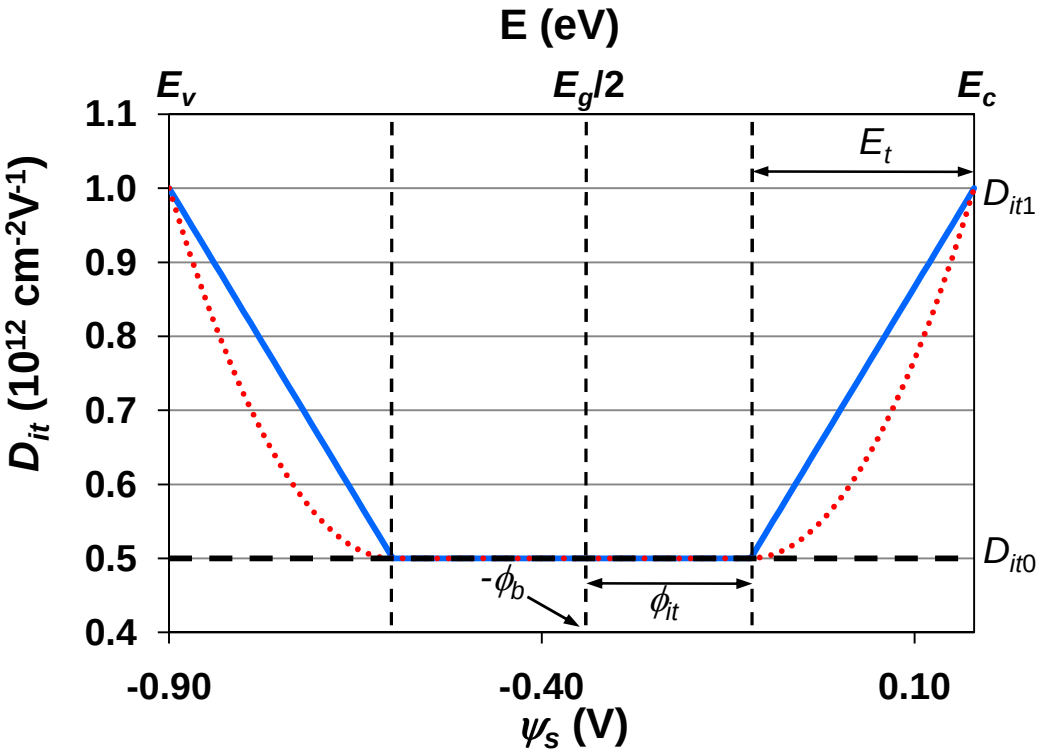

Fig. 4.5. Voltage-distribution (or energy-distribution) of interface traps density $D_{it}(\psi_s)$ plotted as function of surface potential (or energy) for three different cases. Dashed line is for uniform distribution, solid line is for piecewise linear distribution and dotted line is for the piecewise quadratic distribution.

Integrating $D_{it}(\psi_s)$ as given by (3.2) gives the total density of interface states that contribute charge, i.e., $N_{it}(\psi_s)$ as a function of surface potential. For a uniform distribution, $D_{it}(\psi_s) = D_{it0}$ throughout the Si bandgap, $N_{it}(\psi_s)$ is given by

$$N_{it}(\psi_s) = D_{it0}\left|\psi_s + \phi_b\right|. \tag{4.12}$$

The interface trap charge for a uniform distribution is then given by

$$Q_{it}(\psi_s) = -qD_{it0}|\psi_s + \phi_b|\mathrm{sgn}(\psi_s + \phi_b) = -qD_{it0}(\psi_s + \phi_b)\,. \tag{4.13}$$

The expression for the defect potential parameter given by (4.10) is in agreement with the derivation of Q_{it} given by (4.13) for the case of a uniform distribution of interface traps and for an n-type semiconductor. For a piecewise linear distribution $D_{it}(\psi_s)$ is given by

$$D_{it}(\psi_s) = h(|\psi_s + \phi_b| - \phi_{it})[m|\psi_s + \phi_b| + b] + D_{it0}, \tag{4.14}$$

where $h(x)$ is the Heaviside step function, $\phi_{it} = (E_g/2 - E_t)/q$, where E_g is the energy bandgap for Si and E_t is the distance from the bandgap edges where the trap density increase linearly (see Fig. 4.5). The slope inside the linear regions is given by $m = (D_{it1} - D_{it0})/E_t$, and the y-intercept is given by $b = -m\phi_{it}$. Integrating (4.14) gives

$$N_{it}(\psi_s) = h(|\psi_s + \phi_b| - \phi_{it})\left[m\frac{|\psi_s + \phi_b|^2 - \phi_{it}^2}{2} + b(|\psi_s + \phi_b| - \phi_{it})\right] + D_{it0}|\psi_s + \phi_b|. \tag{4.15}$$

For a piecewise quadratic distribution $D_{it}(\psi_s)$ is given by

$$D_{it}(\psi_s) = K\cdot(|\psi_s + \phi_b| - \phi_{it})^2\cdot h(|\psi_s + \phi_b| - \phi_{it}) + D_{it0}, \tag{4.16}$$

where $K = (D_{it1} - D_{it0})/(E_t)^2$. The total density of interface states contributing charge is obtained through integration and is given by

$$N_{it}(\psi_s) = K \cdot h\left(\left|\psi_s + \phi_b\right| - \phi_{it}\right)\left[\frac{\left|\psi_s + \phi_b\right|^3 - \phi_{it}^3}{3} - 2\phi_{it}\frac{\left|\psi_s + \phi_b\right|^2 - \phi_{it}^2}{2}\right.$$
$$\left. + \ \phi_{it}^2\left(\left|\psi_s + \phi_b\right| - \phi_{it}\right)\right] + D_{it0}\left|\psi_s + \phi_b\right|. \tag{4.17}$$

The density of interface traps contributing charge (i.e. N_{it}) obtained from (4.12), (4.15) and (4.17) are plotted as a function of surface potential and bandgap energy in Fig. 4.6.

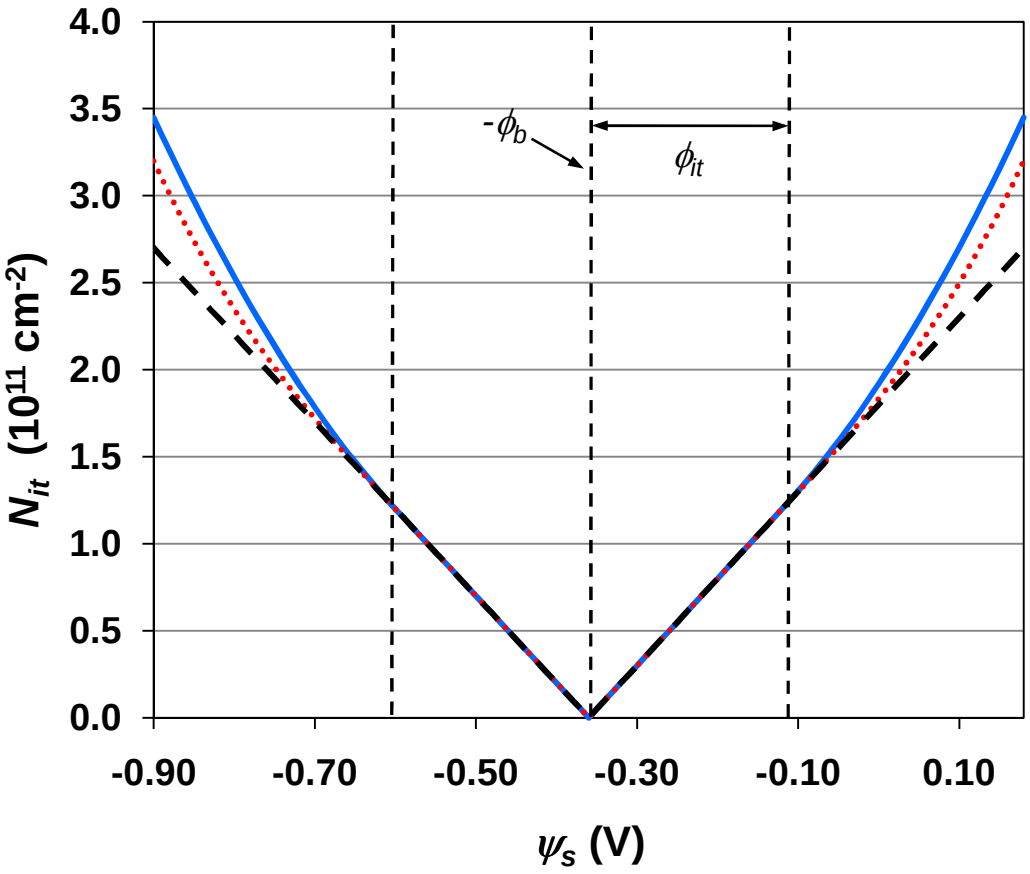

Fig. 4.6. Plot of interface traps contributing charge $N_{it}(\psi_s)$ as a function of surface potential. Dashed line is for uniform distribution, solid line is for piecewise linear distribution and dotted line is for the piecewise quadratic distribution.

Equations (4.12) – (4.17) are easily modified for modeling asymmetric distributions of $D_{it}(\psi_s)$ reported in [108, 122-124]. The asymmetric model requires separate D_{it1} and E_t parameters for acceptor-like ($D_{it1\text{-}acc}$, $E_{t\text{-}acc}$) and donor-like ($D_{it1\text{-}don}$, $E_{t\text{-}don}$) traps. The theoretical description of MOS capacitance is given by the series combination of the oxide capacitance $C_{ox} = \varepsilon_{ox}/t_{ox}$ with the semiconductor capacitance $C_s = dQ_g/d\psi_s$. The units for these capacitances are in Farads per unit area. The semiconductor capacitance per unit area is given by

$$C_s = \frac{dQ_g}{d\psi_s} = -\frac{dQ_s}{d\psi_s} = \frac{Q_0}{\phi_t}\frac{d}{du}\left[\text{sgn}(u)\sqrt{H(u)}\right] = \frac{Q_0}{2\phi_t}\frac{|dH(u)/du|}{\sqrt{H(u)}}, \tag{4.18}$$

where u is the normalized surface potential, i.e., $u = \psi_s/\phi_t$. The calculation of deep-depletion capacitance is obtained by neglecting the formation of an inversion layer and for $u \neq 0$ is given by

$$C_s = \frac{Q_0}{2\phi_t}\frac{\left|e^{-2u} + e^{u} - 1\right|}{\sqrt{e^{-2u_b}(u-1) + e^{u} - u - 1}}. \tag{4.19}$$

Shown in Fig. 4.7 is a comparison of the analytical description of the normalized capacitance and the experimental data. For the analytical calculations, ψ_s is obtained as a function of V_g by iteratively solving (4.8) for the case of a uniform distribution of interface states where $N_{it}(\psi_s)$ is given by (4.12). In the calculations, D_{it0} and N_{ot} are extracted experimentally using the charge-separation technique [108] where N_{ot} is extracted from the shifts in the midgap voltage V_{mg} and D_{it0} is extracted from the increase in stretch-out from midgap to inversion of the *C-V* curves. Also shown in Fig. 4.7 are the normalized *C* values corresponding

to flat-band (ψ_s = 0), midgap ($\psi_s = -\phi_b$) and inversion ($\psi_s = -2\phi_b$). The comparison between the analytical model and the actual *C*-*V* curves results in a reasonable fit for regions between the midgap capacitance (C_{mg}) and the inversion capacitance (C_{inv}). This is expected since the uniform density of interface traps used in the model (i.e., D_{it0}) is extracted from the increase in stretch-out of the *C*-*V* curves within this region. However, for values below inversion and above midgap, the model deviates from the data due to non-uniformities in $D_{it}(\psi_s)$. The fact that the model results in greater deviations from the data in regions between midgap and accumulation is in agreement with previous works that report an asymmetric distribution of $D_{it}(\psi_s)$ after radiation exposure with greater buildup of interface traps in the upper half of the Si bandgap [108, 122-126]. In fact, references [123, 127, 128] report a peak in $D_{it}(\psi_s)$ a few tenths of an eV above midgap which increases with radiation.

A comparison between the analytical model and the experimental data is shown in Fig. 4.8 for the case of a piecewise linear distribution of interface states where $N_{it}(\psi_s)$ is given by the asymmetric form of (4.15). The better agreement between the model and the experimental data demonstrates the advantage of using a surface-potential based modeling approach that allows a non-uniform and asymmetric distribution of $D_{it}(\psi_s)$. Shown in Fig. 4.9 are the corresponding $D_{it}(\psi_s)$ used to obtain the fits in Fig. 4.8.

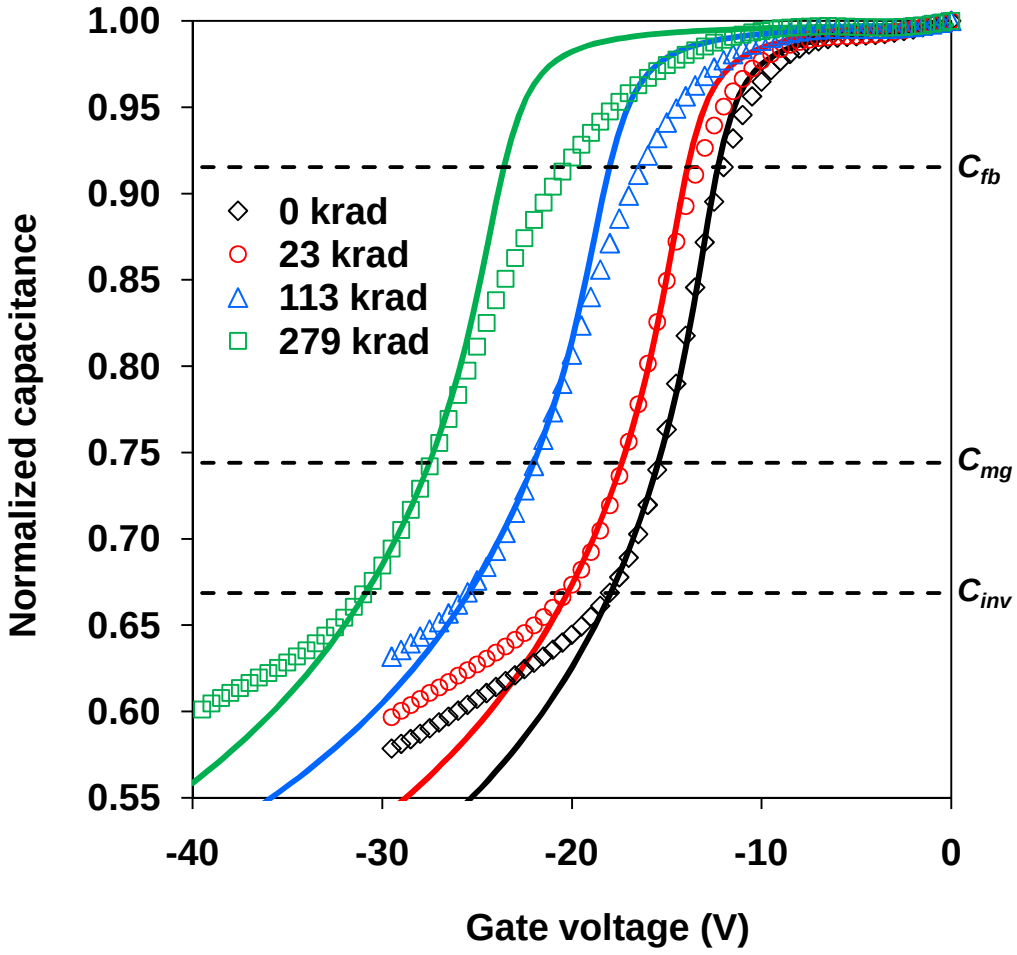

Fig. 4.7. Comparison of experimental data and the analytical calculations of normalized capacitance for the case of a uniform distribution of interface traps where $N_{it}(\psi_s)$ is given by (4.12).

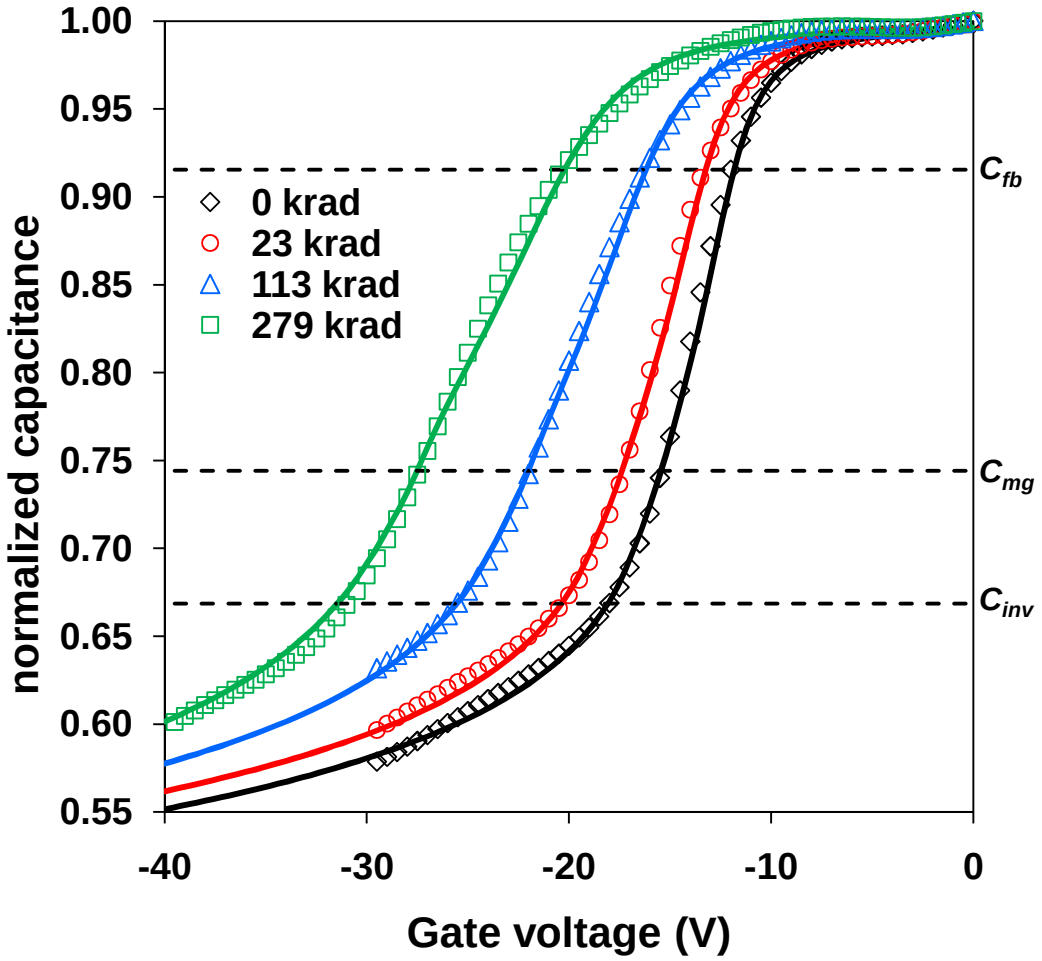

Fig. 4.8. Comparison of experimental data and the analytical calculations of normalized capacitance for the case of a piecewise linear distribution of interface traps where $N_{it}(\psi_s)$ is given by (4.15).

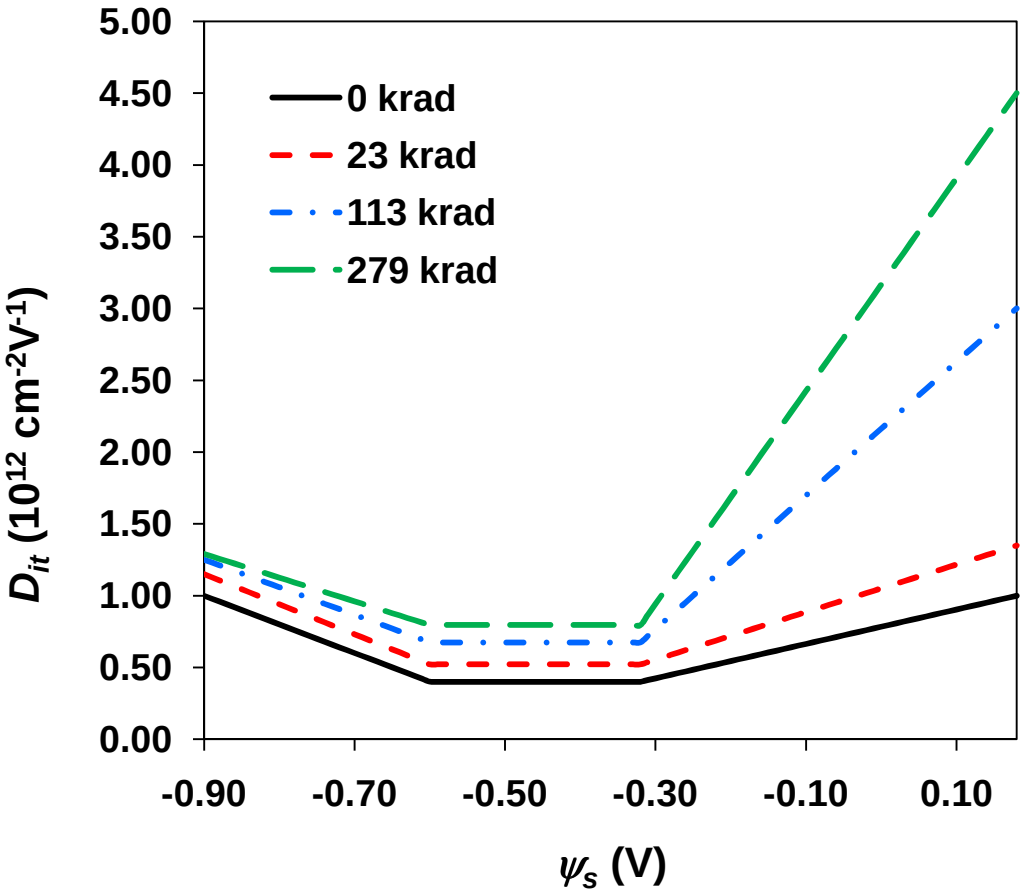

Fig. 4.9. Asymmetric piecewise linear distribution of $D_{it}(\psi_s)$ used to obtain the fits in Fig. 4.5.

4.3 Analytical Modeling Approach for Radiation-Induced Defects

An analytical model that describes the increase in trapped hole density (Δp_t) near the SiO_2-semiconductor interface in a simple 1D MOS system over discrete time intervals (Δt) is given by [21]

$$\Delta p_t = \dot{D}\Delta t g_0 \left[(N_t - p_t)\sigma_p f_{y,p} x_p - p_t \sigma_n f_{y,n} x_n \right] - \frac{p_t}{\tau_{ot}} \Delta t. \tag{4.20}$$

In (4.20), N_t is the density of hole trapping sites and it is assumed uniform within a specific distance from the Si-SiO_2 interface (i.e., $N_t(x) = N_{t0}$ for $x_t < x < t_{ox}$). $\dot{D}$ is the dose rate; g_0 is the generation conversion factor with units of [#ehp/cm^3-rad]; σ_p is the hole capture cross section for hole trapping sites; σ_n is the electron capture cross section for trapped holes; τ_{ot} is the annealing time constant for trapped holes; $f_{y,p}$ and $f_{y,n}$ are the yield functions for holes and electrons, respectively; and x_p and x_n are model parameters for the drift lengths of holes and electrons, respectively. Separate electron and hole yield functions are used in (4.20) since the regions where electrons and holes transport have different electric fields. The drift lengths represent the approximate distances over which holes and electrons transport before being trapped. In the model, x_p and x_n depend on the direction of the electric field inside the oxide and will change as [21]

$$x_p = \begin{Bmatrix} t_{ox} & \text{for } E_1 > 0 \\ (t_{ox} - x_t) & \text{for } E_1 < 0 \end{Bmatrix}, \tag{4.21}$$

and

$$x_n = \begin{Bmatrix} (t_{ox} - x_t) & \text{for } E_1 > 0 \\ t_{ox} & \text{for } E_1 < 0 \end{Bmatrix}, \tag{4.22}$$

where E_1 is the electric field in the region outside the range of the hole trapping sites (i.e., $E_1 = E(x)$ for $0 < x < x_t$). Shown in Fig. 4.10 is a schematic diagram illustrating the location of the hole traps and the distribution of the oxide electric field. E_1 is constant since there is no charge being trapped in this region, whereas $E(x)$ varies linearly for $x_t < x < t_{ox}$ based on the assumption that p_t is uniform inside this region.

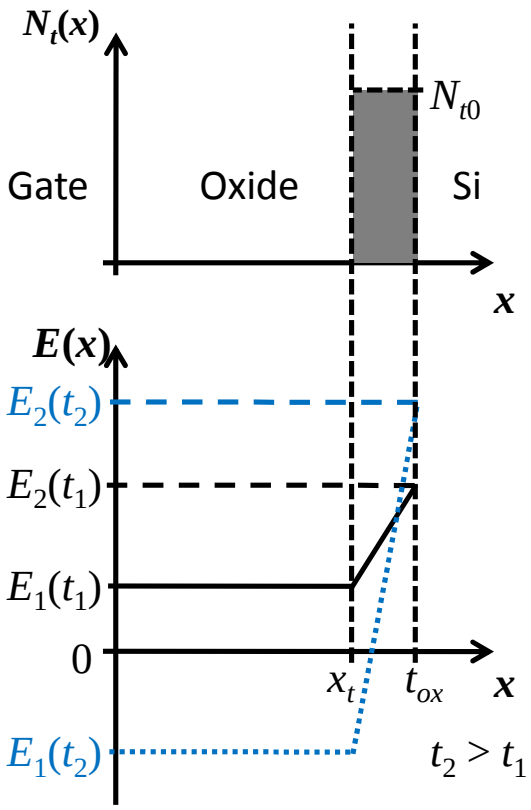

Fig. 4.10. I_d-V_{gs} characteristics before irradiation and after 20, 100, 200 and 1000 krad(SiO_2) of TID for NW FOXFET with W = 200 μm, L = 0.9 μm, V_d = 1 V, V_s = V_b = 0 V.

As charge accumulates in the region of the hole trapping sites (i.e., $x_t < x < t_{ox}$), the electric field distribution inside the oxide region is altered. As mentioned above, $p_t(x)$ is assumed to be uniform inside this region. Under this assumption, the electric field at the edges of this region can be approximated by [21]

$$E_2 = \frac{1}{t_{ox}}\left(V_g - \Phi_{MS} + \phi_{nt} - \psi_s\right), \tag{4.23}$$

and

$$E_1 = E_2 - q\frac{p_t}{\epsilon_{ox}}(t_{ox} - x_t)\,, \tag{4.24}$$

In (4.23) and (4.24), E_2 is the electric field at the SiO_2-Si interface (see Fig. 4.10), V_g is the gate voltage, Φ_{MS} is the gate-to-semiconductor workfunction difference, ϕ_{nt} is the defect potential, ψ_s is the surface potential and ϵ_{ox} is the permittivity of SiO_2. The defect potential parameter is given by (4.10) where N_{ot} has units of cm^{-2} and represents an effective sheet-charge density at the SiO_2-Si interface. Since $p_t(x)$ is assumed to be uniform within $x_t < x < t_{ox}$, the buildup of N_{ot} can be obtained by [104]

$$\Delta N_{ot} = \int_0^{t_{ox}} \frac{x}{t_{ox}} \Delta p_t(x) dx = \Delta p_t (t_{ox} - x_t) \left[1 - \frac{(t_{ox} - x_t)}{2 t_{ox}} \right]. \qquad (4.25)$$

ΔN_{ot} is obtained at every time step by iteratively solving (4.20) and (4.25) at every time step. Updates in surface potential are obtained at every time step from solutions to the modified SPE given by (4.11). The updated surface potential is then used to calculate E_2 and E_1 given by (4.23) and (4.24). The drift length and fractional yield for holes and electrons are then respectively calculated using (4.21) and (4.22) for the drift length and (2.12) for the fractional yield where

$$|\vec{E}| = \begin{Bmatrix} |E_1| & \text{for } E_1 > 0 \\ \dfrac{|E_1| + |E_2|}{2} & \text{for } E_1 < 0 \end{Bmatrix}, \qquad (4.26)$$

for the case of $f_{y,p}$, and

$$|\vec{E}| = \begin{Bmatrix} \dfrac{|E_1| + |E_2|}{2} & \text{for } E_1 > 0 \\ |E_1| & \text{for } E_1 < 0 \end{Bmatrix}, \qquad (4.27)$$

for the case of $f_{y,n}$. A noticeable transition should be expected in the analytical description of the time-dependent buildup of N_{ot} when the electric field for $0 < x <$

x_t is inverted. The transition is due to the adjustment in drift length and fractional yield for holes and electrons, and will result in a reduced buildup of N_{ot} as a function of time.

In the analytical models for the buildup of N_{ot} and N_{it} it assumed that carrier transport in SiO_2 is non-dispersive. Therefore, the hole current density can be obtained from the continuity equation using drift and diffusion mechanisms given by [111]

$$\frac{\partial p}{\partial t} = -\frac{1}{q}\frac{\partial J_p}{\partial x} + G_p - R_p, \tag{4.28}$$

where p is the hole concentrations, G_p is the hole generation rate and R_p is the hole delayed recombination rate. Assuming steady state and that the delayed recombination rates are negligible, the continuity equations become $\partial J_p/\partial x = qG_p$, where the radiation-induced generation rate is given by $G_p = \dot{D} g_0 f_{y,p}$. Integrating we obtain the magnitude of the hole current density inside the oxide as

$$J_p = \begin{Bmatrix} qG_p x & \text{for } E(x) > 0 \\ qG_p(t_{ox} - x) & \text{for } E(x) < 0 \end{Bmatrix}, \tag{4.29}$$

The first key reaction for the formation of interface traps occurs between transporting holes and hydrogen containing defects (DH centers) and results in the release of a proton (H^+) [58]. For the analytical model of N_{it}, the DH centers are assumed to be uniformly distributed inside the oxide [58, 105]. This reaction is coupled with proton transport and can be described by the proton continuity equation given by [111]

$$\frac{\partial n_{H^+}}{\partial t} = -\frac{1}{q}\frac{\partial J_{H^+}}{\partial x} + N_{DH}\sigma_{DH}f_p. \tag{4.30}$$

In (4.30), N_{DH} is the concentration of DH centers, σ_{DH} is the capture cross section for holes at DH centers, J_H^+ is the proton current density and n_{H+} is the proton concentration. The proton flux $f_H^+ = J_H^+/q$ can be obtained by integrating (4.30) assuming steady state condition and substituting (4.29) for the case of a positive electric field (holes directed towards the Si-SiO_2 interface) [129]:

$$f_{H^+} = N_{DH}\sigma_{DH}\dot{D}g_0 f_{y,p}\frac{x^2}{2}. \tag{4.31}$$

Using (4.31), ΔN_{it} over discrete time intervals is given by [129]

$$\Delta N_{it} = \dot{D}\Delta t g_0 f_{y,p}(N_{SiH} - N_{it})N_{DH}\sigma_{DH}\sigma_{it}\frac{x_H^2}{2} - \frac{N_{it}}{\tau_{it}}\Delta t, \tag{4.32}$$

where N_{SiH} is the density of passivated dangling bonds at the interface, σ_{it} is the capture cross section for protons at the passivated dangling bonds, τ_{it} is the annealing time constant for interface traps and x_H is the drift length for protons. Eq. (4.32) describes the reaction between transporting protons and hydrogen-passivated dangling bonds at the Si-SiO_2 interface described by [111]

$$SiH + H^+ \rightarrow Si^+ + H_2. \tag{4.33}$$

As described in [21], when sufficient charge is accumulated in the region of the hole trapping sites (i.e., $x_t < x < t_{ox}$), the electric field induced by the gate bias and work function difference are offset and can result in the inversion of E_1 (i.e., E_1 is now directed towards the gate). At this point in time, only the protons

generated in Region 2 (i.e., $x_t < x < t_{ox}$) can drift towards the interface and react with passivated SiH bonds to form interface traps. In the model, x_H captures this phenomenon and is given by

$$x_H = \begin{Bmatrix} t_{ox} & \text{for } E_1 > 0 \\ (t_{ox} - x_t) & \text{for } E_1 < 0 \end{Bmatrix}, \tag{4.34}$$

ΔN_{ot} and ΔN_{it} are obtained by iteratively solving (4.20), (4.25) and (4.32) at discrete time steps while updating the surface potential and the oxide electric field (i.e., E_1 and E_2). The defect potential parameter in (4.23) is obtained as a function of $N_{ot}(t)$ and $D_{it}(t, \psi_s) = qN_{it}(t)/E_g$ at every time step, where $N_{ot}(t) = N_{ot}(t - \Delta t) + \Delta N_{ot}$ and $N_{it}(t) = N_{it}(t - \Delta t) + \Delta N_{it}$.

The plot in Fig. 4.11 shows the comparison between ΔN_{ot} and ΔN_{it} as a function of dose obtained using the analytical model (solid line) and experimentally (symbols) for an NW FOXFET device with L = 0.9 µm. The analytical model parameters used for these calculations are summarized in Table 4.2. The densities of hole trapping sites and DH centers used in the model are similar to what is reported in [58] and [130]. Also, the location of N_t (i.e., x_t) is within the range of values used in [111]. The analytical model correctly describes the reduction in the formation rate of N_{ot} and N_{it} as a function of dose observed experimentally. In the results plotted in Fig. 4.11, the change in the slope for the analytical model descriptions of ΔN_{ot} and ΔN_{it} determines the point of inversion of E_{ox1}. At this point, only the holes generated within $x_t < x < t_{ox}$ can contribute to the

buildup of oxide trapped charge and interface traps resulting in the reduction of the formation rate (i.e., the slope in Fig. 4.11).

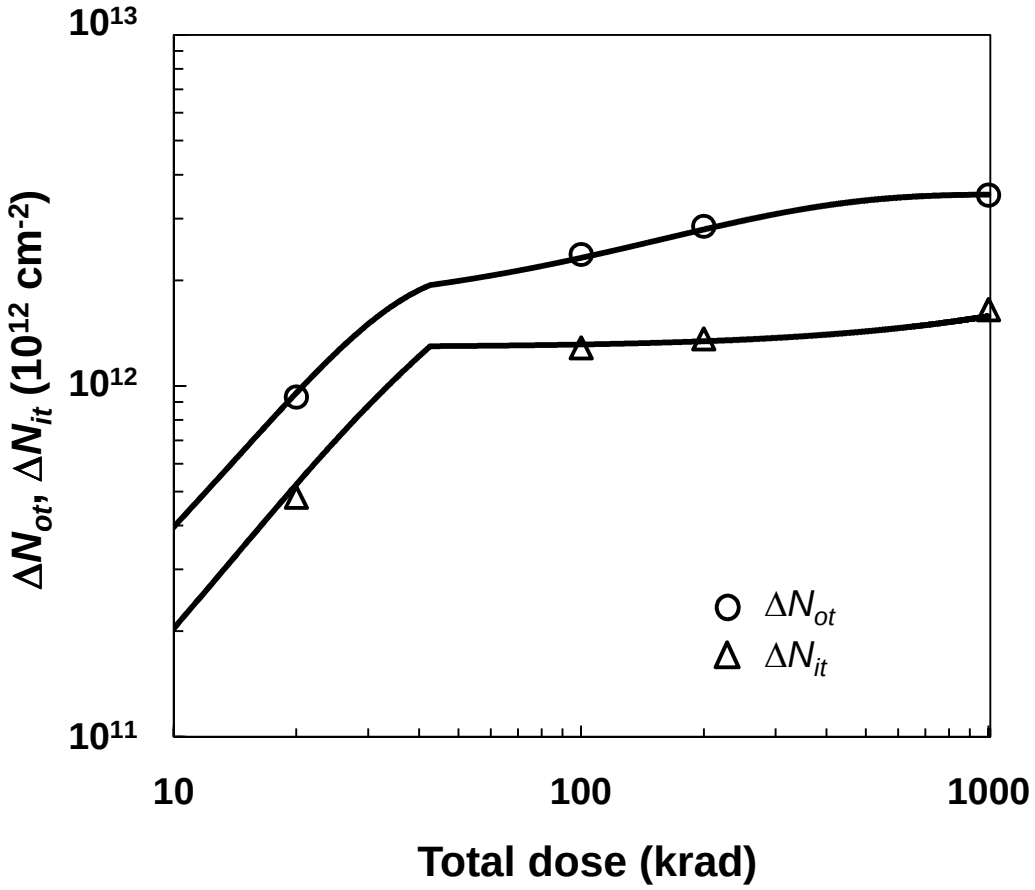

Fig. 4.11. Comparison between ΔN_{ot} and ΔN_{it} as a function of dose obtained through the analytical models (solid line) and experimentally (symbols) for NW FOXFET device with L = 0.9 μm, and using a dose rate of 20 rad(SiO_2)/s.

TABLE 4.2
SUMMARY OF MODEL PARAMETERS USED IN CALCULATIONS OF ΔN_{it} AND ΔN_{ot} SHOWN IN FIG. 4.11

Parameter	Symbol	Value	Units
Density of hole trapping sites	N_t	8.0×10^{19}	cm^{-3}
Capture cross section for holes at hole traps	σ_p	2.2×10^{-15}	cm^2
Capture cross section for electrons at trapped holes	σ_n	1.7×10^{-14}	cm^2
Density of hydrogenated defects (DH centers)	N_{DH}	7.3×10^{17}	cm^{-3}
Capture cross-sections for holes at DR centers	σ_{DH}	2.0×10^{-15}	cm^2
Density of passivated dangling bonds at the Si-SiO_2 interface	N_{SiH}	4.8×10^{12}	cm^{-2}
Capture cross section for protons at the passivated dangling bonds	σ_{it}	2.0×10^{-12}	cm^2
Location of hole trapping sites (measured from the Si-SiO_2 interface)	$(t_{ox}-x_t)$	35	nm

CHAPTER 5. MODELING RADIATION EFFECTS IN CMOS DEVICES

5.1 Incorporating Radiation Effects into Compact Models for CMOS Devices

This chapter of the dissertation describes the incorporation of TID effects into surface-potential-based compact models for advanced CMOS technologies. The incorporation is accomplished through modifications of the SPE, i.e., (4.11), which allow the inclusion of radiation-induced defect densities (i.e., N_{ot} and N_{it}) into the calculations of ψ_s. Verification of the compact modeling approach is achieved via comparison with experimental data for the degraded I_d-V_{gs} characteristics of devices from advanced CMOS technologies. The I_d-V_{gs} characteristics are modeled analytically using an adapted form of the charge-sheet model (CSM) which includes the effects of N_{ot} and N_{it} through calculations of ψ_s using the modified SPE. Additional verification is obtained from the comparison with radiation-induced degradation parameters, such as threshold voltage shifts, increase in off-state leakage current and changes in the subthreshold swing

The compact modeling approach presented in this dissertation is implemented into PSP, the industry standard surface-potential-based compact model for MOS devices. This is accomplished by the renormalization of the modified surface potential equation in order to make the PSP formulation applicable to irradiated devices. Initial verification is obtained through the reproduction of the degraded I_d-V_{gs} characteristics of the 90 nm LSP NW FOXFET devices. Radiation-induced degradation in the effective channel mobility due to enhanced Coulomb scattering at near-surface oxide and interfacial defects is determined through semi-empirical modeling within PSP [131], where

the Coulomb scattering parameter is obtained as a function of the radiation-induced defect densities N_{ot} and N_{it}. Additional verification for the incorporation of TID into PSP based on the renormalized SPE is obtained by establishing a specific relation between ΔV_{th} and the degradation of the inverse subthreshold slope (S).

5.2 Total Ionizing Dose and the Charge Sheet Model

The charge sheet model, originally presented by Brews in 1978 [132], is the first engineering surface-potential-based model and it forms the theoretical background for several modern surface potential based compact models [133]. The CSM follows all of the assumptions of the rigorous double integral Pao-Sah model for drain current [134]. These assumptions are: i) uniform doping, ii) gradual channel approximation, iii) long channel (no short channel effects) and iv) complete ionization of impurities. Additionally, the CSM makes the assumption that the inversion layer is of infinitesimal thickness. Under this assumption, drain current in the CSM can be expressed as

$$I_d = -W\mu_n \left(Q_i \frac{d\psi_s}{dy} - \phi_t \frac{dQ_i}{dy} \right), \tag{5.1}$$

where y represents the lateral direction in the channel (i.e., from source to drain), μ_n is the electron mobility and the inversion charge per unit area (Q_i) is given by

$$Q_i = -C_{ox} \left(V_g - \Phi_{MS} - \psi_s - \gamma \sqrt{\psi_s - \phi_t} \right). \tag{5.2}$$

Variable separation and integration of (5.1) yields drift and diffusion components of the drain current as given by

$$I_d = -\mu_n \frac{W}{L}\left[\int_{\psi_{ss}}^{\psi_{sd}} Q_i d\psi_s + \phi_t\left(Q_{is} - Q_{id}\right)\right], \tag{5.3}$$

In (5.3), ψ_{ss} and Q_{is} is the surface potential and inversion charge per unit area at the source and ψ_{sd} and Q_{id} is the surface potential and inversion charge per unit area at the drain. Total ionizing dose effects are incorporated into the CSM using the defect potential parameter in Q_i. The inversion charge per unit area becomes

$$Q_i = -C_{ox}\left(V_g - \Phi_{MS} + \phi_{nt} - \psi_s - \gamma\sqrt{\psi_s - \phi_t}\right). \tag{5.4}$$

Substituting (5.4) back into (5.3) and performing the integration yields

$$I_d = -\mu_n \frac{W}{L} C_{ox}(I_1 + I_2), \tag{5.5}$$

where I_1 is the drift current component and is given by [129]

$$\begin{aligned} I_1 = &\left[V_g - \Phi_{MS} + \frac{q}{C_{ox}}(N_{ot} + \phi_b D_{it})\right]\left(\psi_{sd} - \psi_{ss}\right) \\ &- \frac{1}{2}\left(1 + q\frac{D_{it}}{C_{ox}}\right)\left(\psi_{sd}^2 - \psi_{ss}^2\right) - \frac{2\gamma}{3}\left[\left(\psi_{sd} - \phi_t\right)^{3/2} - \left(\psi_{sd} - \phi_t\right)^{3/2}\right], \end{aligned} \tag{5.6}$$

and I_2 is the diffusion current component and is given by [129]

$$I_2 = \phi_t\left[\left(1 + q\frac{D_{it}}{C_{ox}}\right)\left(\psi_{sd} - \psi_{ss}\right) - \gamma\left(\sqrt{\psi_{sd} - \phi_t} - \sqrt{\psi_{ss} - \phi_t}\right)\right], \tag{5.7}$$

5.3 Modeling Ionizing Radiation Effects Using PSP

The implementation of TID into PSP is accomplished by the renormalization of the modified surface potential equation which can be expressed as

$$\left(V_g - V_{FB} - \xi\psi_s\right)^2 = \gamma^2 \phi_t H\left(\beta\psi_s\right). \tag{5.8}$$

In (4.11), V_{FB} is given by

$$\mathrm{V}_{FB} = \Phi_{MS} - \frac{q}{C_{ox}}(N_{ot} + D_{it}\phi_b). \tag{5.9}$$

where Φ_{MS} is the gate-to-semiconductor work-function difference and

$$\xi = 1 + \frac{q}{C_{ox}} D_{it}. \tag{5.10}$$

The standard SPE [120, 121] used in the PSP model is

$$\left(V_g - V_{FB} - \psi_s\right)^2 = \gamma^2 \phi_t H\left(\beta\psi_s\right). \tag{5.11}$$

Thus Eq. (5.8) extends the standard model through the addition of the interface trap variable, ξ. In order to incorporate TID effects into the existing PSP framework, the following renormalization is performed: $V_g^* = V_g/\xi$, $V_{FB}^* = V_{FB}/\xi$ and $\gamma^* = \gamma/\xi$. Consequently, [135]

$$\left(V_g^* - V_{FB}^* - \psi_s\right)^2 = \left(\gamma^*\right)^2 \phi_t H\left(\beta\psi_s\right). \tag{5.12}$$

The new equation therefore has the same form as (5.11) but with a modified gate bias, flat-band voltage and body factor. The advantage is that, unlike (5.8), (5.12) can be solved with respect to ψ_s using the same highly accurate analytical approximations that are used in PSP [131, 136]. Once the surface potentials at the source side (ψ_{ss}) and the drain side (ψ_{sd}) are available, the drain current can be readily obtained by using symmetric linearization method [131, 136, 137] as

$$I_{ds} = \frac{W}{L}\mu_{eff}C_{ox}\left(q_{im} + \alpha_m \phi_t\right)\Delta\psi. \tag{5.13}$$

where q_{im} is the inversion charge per unit area at the potential mid-point $\psi_{sm} = (\psi_{ss} + \psi_{sd})/2$, α_m is the linearization coefficient, $\Delta\psi = \psi_{sd} - \psi_{ss}$, and μ_{eff} is the effective channel mobility. The terminal charges (Q_j, j = D, G, S, B) can be obtained as well.

The degradation of effective channel mobility due to ionizing-radiation has been modeled empirically as a function of interface trapped charge in [138, 139]. Later studies observed the additional contribution from ΔN_{ot} to effective channel mobility degradation, which was modeled empirically using a linear combination of ΔN_{ot} and ΔN_{it} given by [140]:

$$\frac{\mu_{eff}}{\mu_0} = \frac{1}{1 + \alpha_{it}\Delta N_{it} + \alpha_{ot}\Delta N_{ot}}. \tag{5.14}$$

In (5.14), α_{it} and α_{ot} are the model parameters capturing the effects of interface and oxide trapped charge respectively. Experimental data presented in [140] revealed a more pronounced radiation-induced degradation of μ_{eff} at 77 K than at room-temperature, explained by an increase in the relative importance of Coulomb scattering from oxide and interface trapped charges [140]. Hence the accurate modeling of mobility degradation is particularly important for applications exposed to radiation in low temperature environments.

Deviations from the universal $\mu(E_{eff})$ dependence due to Coulomb scattering was demonstrated experimentally and modeled analytically as a function of temperature (T) in [141]. In [141], μ_{eff} is shown to be limited by Coulomb

scattering at low temperatures for low values of inversion charge (Q_i), and that it increases with Q_i (or E_{eff}). This is consistent with the results shown in [140].

The degradation of the effective channel mobility can be determined through the semi-empirical model used in PSP [131] given by,

$$\mu_{eff} = \frac{\mathrm{U0}}{1 + \left(\mathrm{MUE}\cdot E_{eff}\right)^{\mathrm{THEMU}} + \mathrm{CS}\cdot q_{bm}^2/\left(q_{bm} + q_{im}\right)^2}. \tag{5.15}$$

In (5.15), U0 is the low-field mobility, MUE and THEMU account for surface roughness and phonon scattering, $E_{eff} = (q_{bm} + \eta \cdot q_{im})/\varepsilon_{si}$ is the effective vertical field, q_{bm} is the bulk charge per unit area at the surface potential mid-point, η = 0.5, and the CS parameter accounts for coulomb scattering. The coulomb scattering parameter CS is obtained as a function of the radiation-induced defect densities N_{ot} and N_{it} and is given by

$$\mathrm{CS} = \alpha_{it}\Delta N_{it} + \alpha_{ot}\Delta N_{ot}. \tag{5.16}$$

Shown in Fig. 5.1 is a plot of μ_{eff} vs. E_{eff} given by (5.15) and (5.16) for several ionizing dose levels up to 1000 krad(SiO_2) using $\alpha_{it} = 2.4\times10^{-12}$ cm^2 and $\alpha_{ot} = 9\times10^{-13}$ cm^2. The deviation from the universal mobility curve (i.e., μ_{eff} for CS = 0) increases as a function of dose due to the more significant role of Coulomb scattering as ΔN_{ot} and ΔN_{it} increase. A comparison of experimental data with the CSM [132] description of the transconductance using μ_{eff} given by (5.15) and (5.16) is shown in Fig. 5.2 for several ionizing dose levels. The I_d-V_{gs} characteristics are also compared and plotted in Fig. 5.3. The agreement between

the experimental and the model curves serves to verify the model for radiation-induced degradation of effective channel mobility.

Degradation of channel mobility was not considered for the extractions of the radiation-induced defect densities (plotted in Fig. 3.7), which may lead to an underestimation for ΔN_{ot} and ΔN_{it}. The radiation-induced defect densities used to obtain the fits in Figs. 5.2 and 5.3 are therefore slightly adjusted from the extracted values.

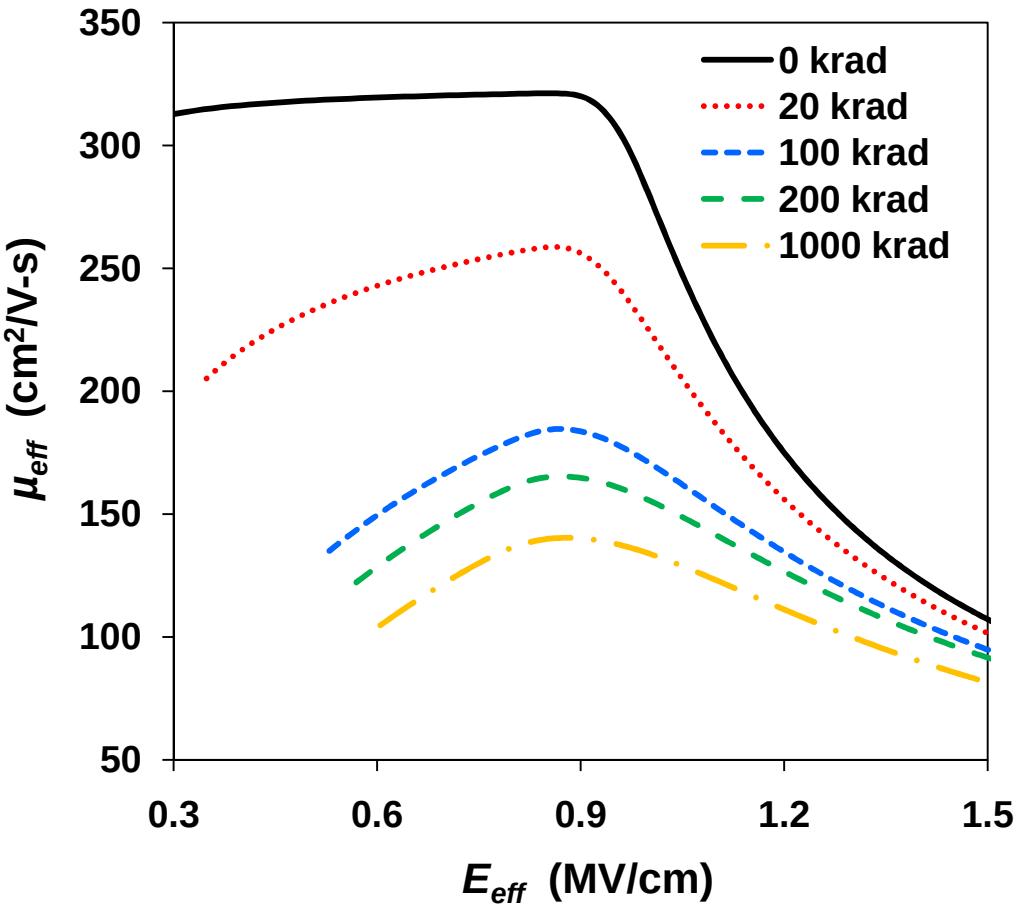

Fig. 5.1. Calculated effective channel mobility μ_{eff} vs. E_{eff} given by (5.15) and (5.16) for several TID levels up to 1000 krad(SiO_2).

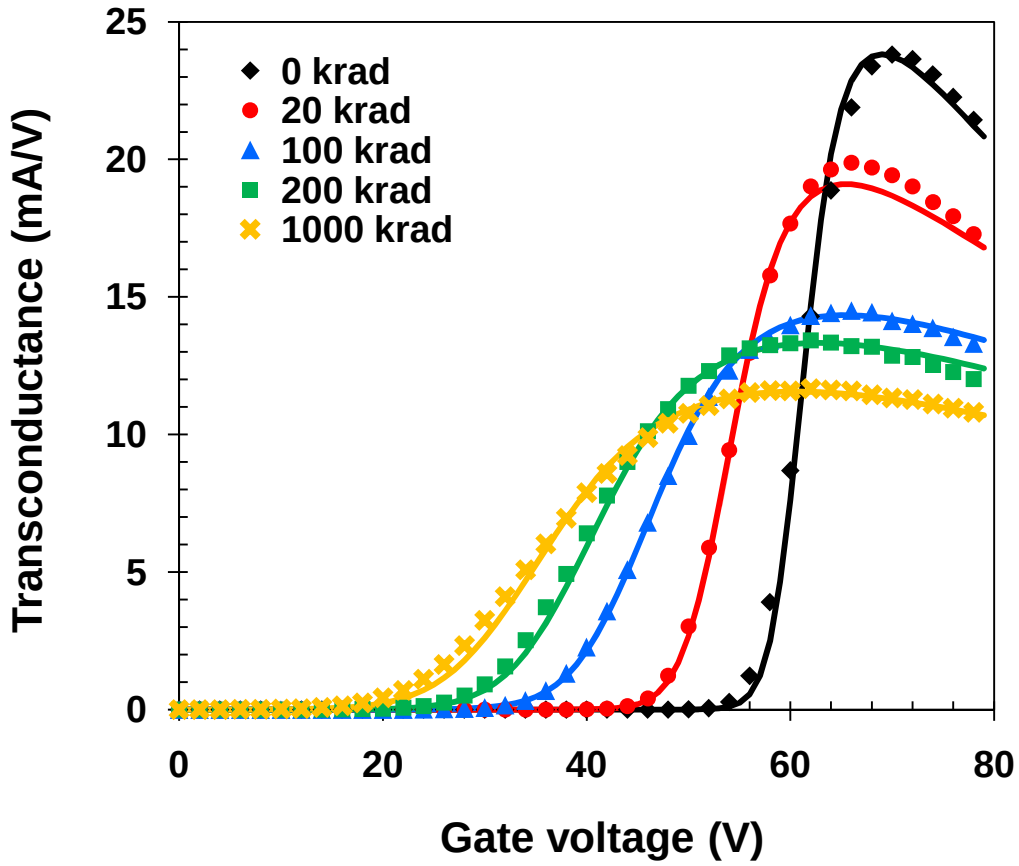

Fig. 5.2. Transconductance vs. gate voltage for several ionizing dose levels up to 1000 krad(SiO_2). Charge-sheet model description of the transconductance using μ_{eff} given by (5.15) and (5.16) is the solid line. Symbols represent the experimental data. W = 200 μm, L = 1.5 μm, V_d = 0.1 V, $V_s = V_b$ = 0 V.

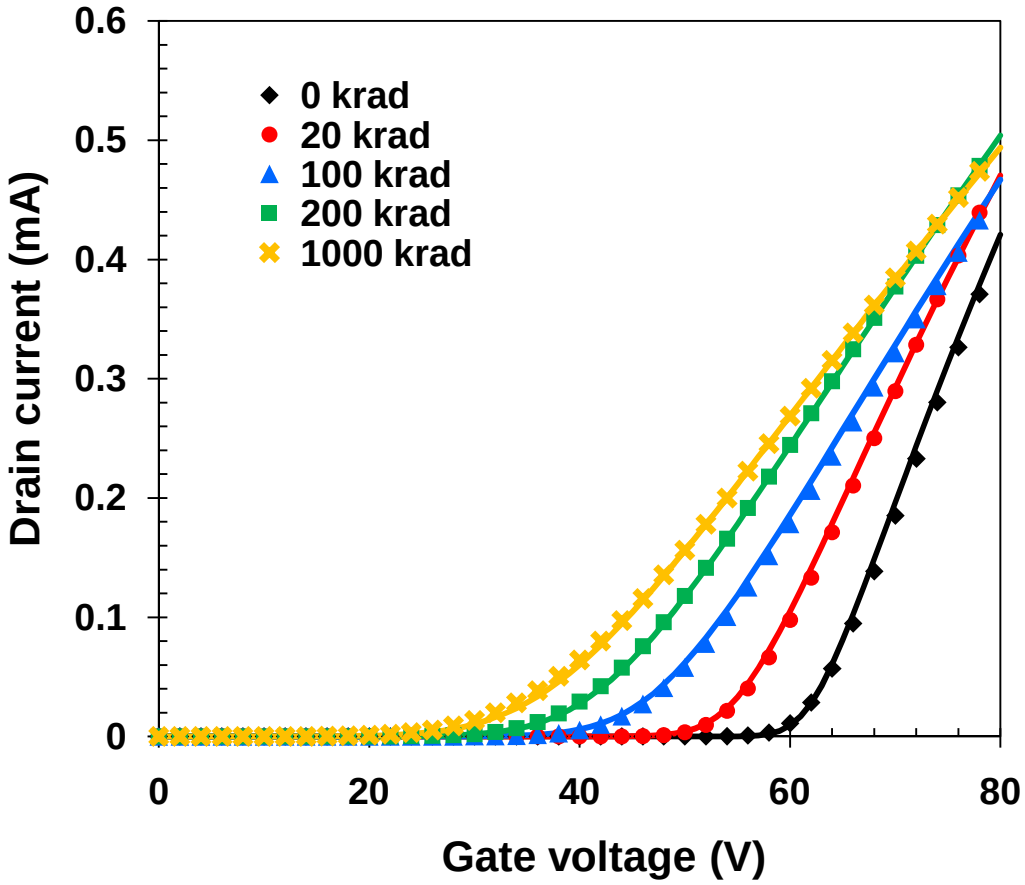

Fig. 5.3. I_d–V_{gs} characteristics for several ionizing dose levels up to 1000 krad(SiO_2). Charge-sheet model description of I_d using μ_{eff} given (5.15) and (5.16) is represented by the solid line. Symbols indicate the experimental data.

The complete model has been implemented in PSP, which includes all the secondary effects such as small-geometry effects, mobility degradation and various leakage components which are also essential in modeling the device characteristics. A comparison of experimental data (symbols) with the PSP model (solid lines) is given in Fig. 5.4. As shown in Fig. 5.4, there is a good agreement between the experimental I_d-V_{gs} characteristics and the compact model. Additional experimental verification of the modeling of TID effects based on the

renormalized SPE (5.12) can be obtained through the relation between ΔV_{th}, ΔN_{ot} and the degradation of the inverse subthreshold slope given by [142]

$$S = \frac{dV_g}{d\log_{10} I_d} \approx \ln(10)\phi_t \left(1 + \frac{C_s + C_i}{\mathrm{C_{ox}}}\right). \tag{5.17}$$

In (5.17), C_i is the interface trap capacitance given by $C_i = q^2 D_{it}$ and C_s is the semiconductor capacitance which under the depletion approximation (i.e., $3\phi_t < \psi_s < 2\phi_b$) is given by

$$C_s \approx C_b = \sqrt{\frac{q\epsilon_{si} N_a}{2\psi_s}}. \tag{5.18}$$

Using (5.17) and (5.18), the normalized inverse subthreshold slope becomes [135]

$$\frac{S}{S_0} = 1 + \frac{(\xi - 1)C_{ox}}{C_{ox} + C_b} \tag{5.19}$$

where ξ is given by (5.10) and

$$S_0 = \ln(10)\phi_t \left(1 + \frac{C_b}{C_{ox}}\right). \tag{5.20}$$

From (5.17) – (5.20), the relation between ΔV_{th} and the ratio S/S_0 is given by [135]

$$\Delta V_{th} + \frac{q\Delta N_{ot}}{C_{ox}} + \phi_b \left(1 + \frac{C_b}{C_{ox}}\right) = \phi_b \left(1 + \frac{C_b}{C_{ox}}\right)\frac{S}{S_0}. \tag{5.21}$$

Comparison with experimental data (Fig. 5.5) indicates the validity of (5.20) and hence further confirms (5.12). Note that experimental data shown in Fig. 5.5 correspond to the gate voltages at which I_d = 6 μA extracted from the I_d vs. (V_g –

$q\Delta N_{ot}/C_{ox}$) characteristics, where ΔN_{ot} is referenced to the 20 krad(SiO_2) dose level. The y-intercept of the solid line in Fig. 5.5 is therefore proportional to ΔN_{ot} at 20 krad. The slope for the theoretical description of ΔV_{th} as a function of S/S_0 in Fig. 5.5 (solid line) is proportional to $(1 + C_b/C_{ox})$ where C_b is given by (5.18) using $\psi_s = \phi_b + 5\phi_t$.

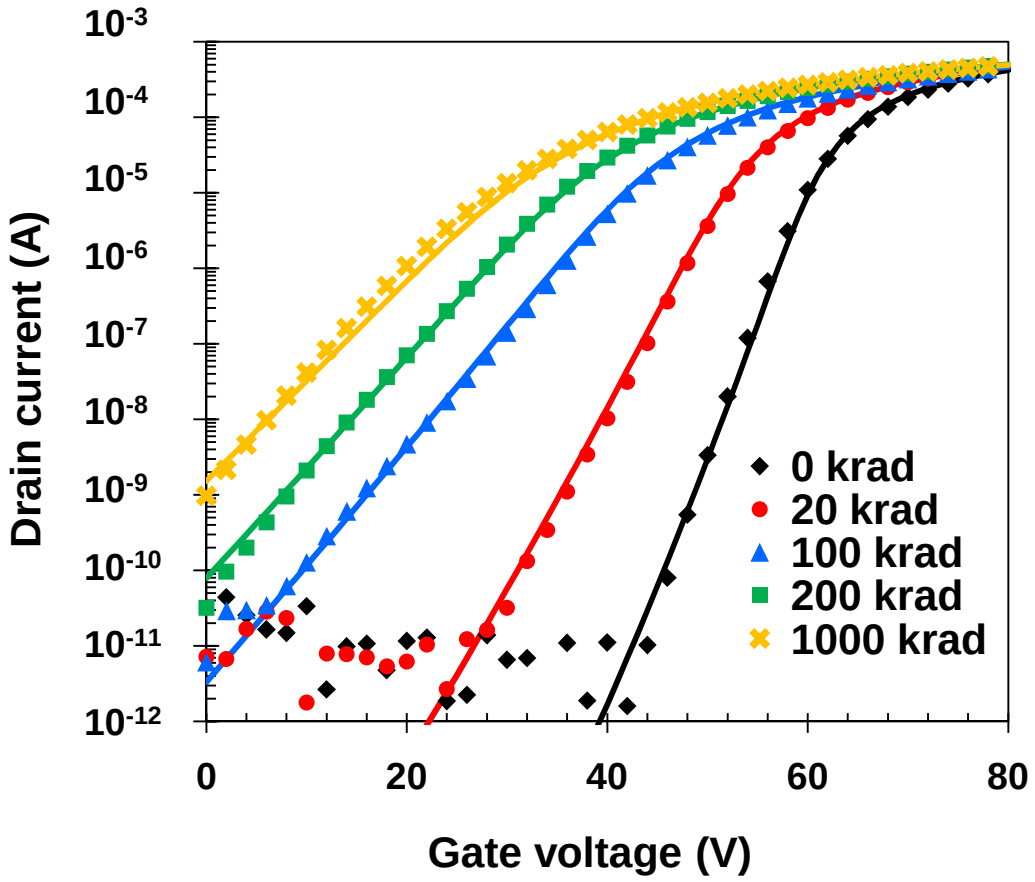

Fig. 5.4. Comparison of the I-V characteristics obtained using the PSP model against the experimental data for a drain bias of V_d = 100 mV at several levels of TID. W = 200 μm, L = 1.5 μm. t_{ox} = 425 nm.

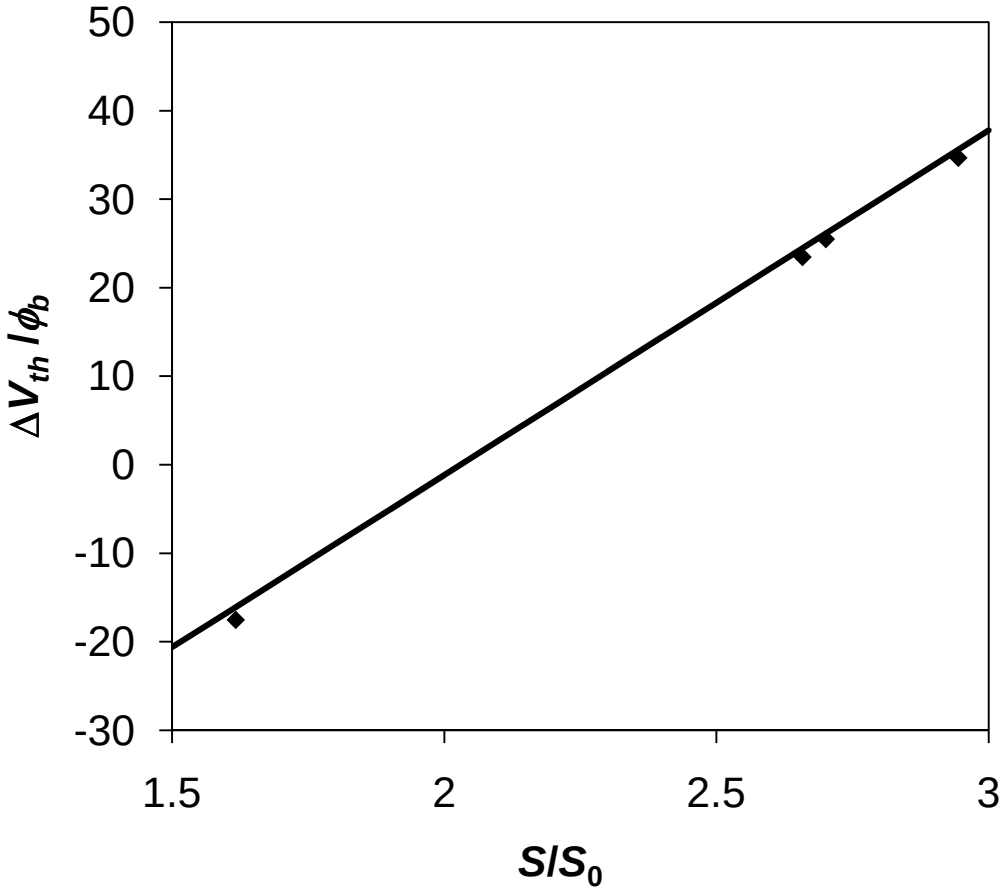

Fig. 5.5. Normalized shifts in the threshold voltage as a function of the normalized inverse subthreshold slope. Solid line represents theoretical results given by (5.21) and symbols represent the experimental data.

Through the incorporation of the TID effects into PSP, radiation-induced inter-device leakage paths created on advanced CMOS IC's exposed to ionizing radiation can be accurately modeled as parasitic FOXFET devices. In many cases of advanced CMOS IC designs, n-well-to-n^+ leakage paths (i.e., from the n-well of pull-up p-channel devices to the n+ source or drain of the pull-down n-channel devices) are the most significant contributors to radiation-induced inter-device leakage. For example, the SRAM array presented in [23]. For these leakage paths,

the parasitic structure is highly irregular with non-uniform oxide thickness and channel doping concentration. The buildup of radiation-induced defects is also impacted by the irregularity of the device [21]. However, it is possible to make reasonable approximations for oxide thickness, doping concentration and device geometry, which allow modeling inter-device leakage as a planar FOXFET parasitic device using the radiation-enabled compact model based on PSP [21]. Therefore, by making use of the presented model one can obtain the contribution to off-state leakage current $I_{off} = I_d(V_{gs} = 0\ \text{V})$ from specific inter-device leakage paths as a function of N_{ot} and D_{it}. Shown in Fig. 5.6 is a plot of I_{off} normalized to the width of the NW FOXFET width and plotted as a function of D_{it} for several values of N_{ot}. This plot demonstrates the well known reduction in I_{off} as a function of D_{it} due to a positive shift that results from the stretch-out of the I_d-V_{gs} characteristics. Modeling the reduction in I_{off} is critical in applications where sufficient time and energy allows for the formation of interface traps

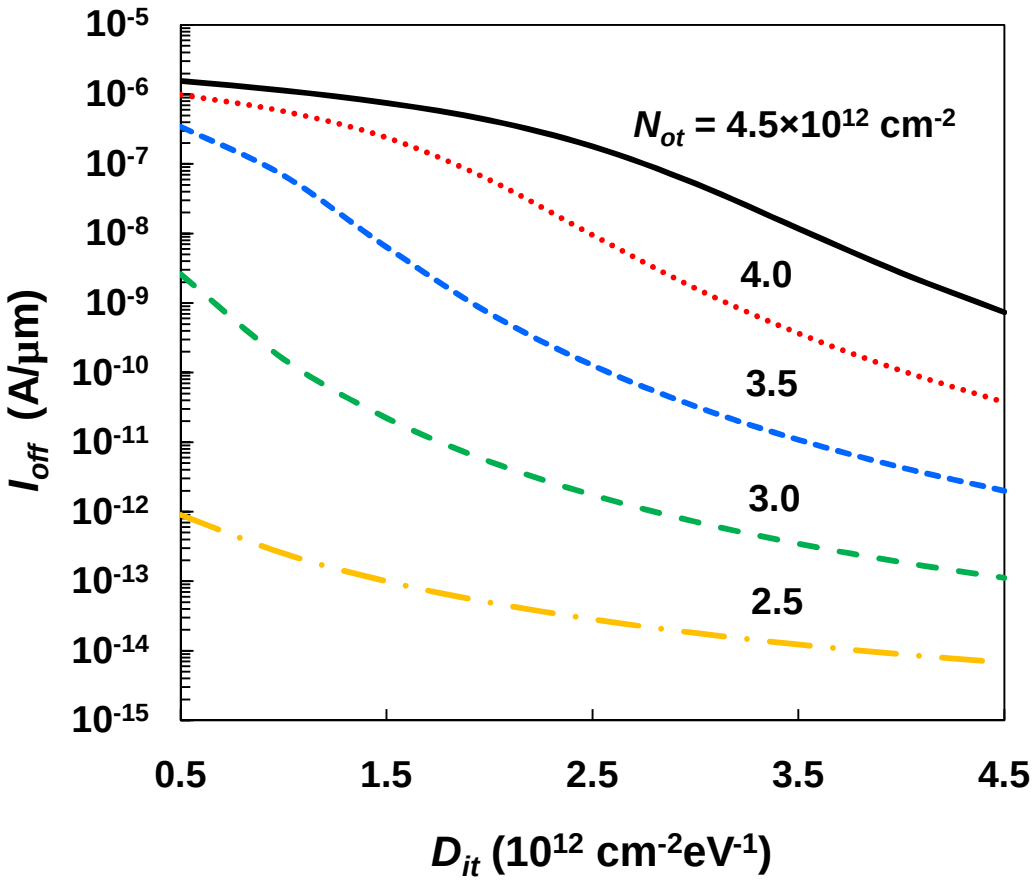

Fig. 5.6. Contribution to off-state leakage current (I_{off}) from inter-device leakage as a function of N_{ot} and D_{it} normalized to the width of the parasitic FOXFET device. L = 1.5 μm, V_d = 0.1 V, V_s = V_b = 0 V.

5.4 Modeling the Radiation Response of FD SOI n-Channel Transistors

MOSFETs fabricated in silicon-on-insulator (SOI) technologies can result in better control of short channel effects and achieve superior electrical response compared to their bulk counterparts in deep sub-micron nodes. Moreover, SOI MOSFETs have also been shown to improve hardness to transient radiation effects, since the buried oxide (BOX) layer dielectrically isolates the device from the substrate, which significantly reduces the sensitive volume for transient radiation-induced charge collection [143]. Despite their advantages, SOI

MOSFETs remain more susceptible to TID damage than bulk MOSFETs in technology nodes below 180 nm [143]. The susceptibility of SOI MOSFETs arises from the radiation-induced buildup of defects in the relatively thick BOX layer. Modeling TID effects using a surface-potential-based compact modeling approach presents considerable advantages for advanced fully depleted SOI MOSFETs (e.g., the coupling effect between charge buildup in the Si-BOX interface and the front surface can be modeled continuously for all regions of operation). This section of the dissertation describes a new approach for incorporating TID effects into surface-potential based compact models. This approach allows describing the transition between partial depletion (PD) and full depletion (FD) conditions as a function of radiation and bias. The model is verified by comparison with 2D TCAD simulations for the degradation of the drain current (I_d) vs. front gate voltage (V_{GF}) characteristics of SOI transistors.

The model is based on the first integration of the 1D Poisson equation given by [144, 145]

$$\frac{d^2\psi}{dx^2} = \frac{q}{\epsilon_{si}}\left[N_a + \frac{n_i^2}{N_a}e^{\beta(\psi+\phi_n)} - N_a e^{-\beta\psi}\right]. \tag{5.22}$$

In (5.22), x is in the vertical direction across the Si film (see Fig. 5.7), ψ is the electrostatic potential and ϕ_n is the split in the Fermi levels. Following the one-dimensional integration of (5.22) and applying Gauss' Law at the front and back interfaces results in an implicit equation relating the potential at the front surface (ψ_{sf}) and the back surface (ψ_{sb}) which in a normalized fashion is given by [145, 146]

$$\left(u_g - u_{sf}\right)^2 - \frac{t_{oxf}^2}{t_{oxb}^2}(u_e - u_{sb})^2 = G^2\left[e^{-(2u_b - u_n)}(e^{u_{sf}} - e^{u_{sb}}) + (e^{-u_{sf}} - e^{-u_{sb}}) + (u_{sf} - u_{sb})\right]. \tag{5.23}$$

Here, $u_g = (V_{GF} - V_{FBF0})/\phi_t$, $u_e = (V_{GB} - V_{FBB}^*)/\phi_t$, $u_{sf} = \psi_{sf}/\phi_t$, $u_{sb} = \psi_{sb}/\phi_t$, $u_b = \phi_b/\phi_t$, $u_n = \phi_n/\phi_t$, where $\phi_b = \phi_t \ln(N_a/n_i)$ is the bulk potential. In (5.23), $G^2 = \gamma^2/\phi_t$, where γ is the body coefficient given by

$$\gamma = \frac{\sqrt{2q\epsilon_{si}N_a}}{C_{oxf}}, \tag{5.24}$$

and $C_{oxf} = \epsilon_{ox}/t_{oxf}$ is the front gate capacitance per unit area. V_{FBF0} and V_{FBB0} are the metal-to-semiconductor work function differences for the front and back gates, respectively. The back gate flatband voltage is given by $V_{FBB}^* = V_{FBB0} - \phi_{nt}$, where ϕ_{nt} is the defect potential given by (4.10). Solving (5.23) requires a second coupling equation relating u_{sf} and u_{sb}. For FD condition of the Si film this relationship is approximated by neglecting the inversion charge when integrating Poisson's equation and is given by [146, 147]

$$u_{sb} = u_{sf} - \frac{qN_a t_{si}^2}{2\epsilon_{si}\phi_t} - E_{sb}t_{si}, \tag{5.25}$$

where E_{sb} is the normalized electric field at the back-side interface given by

$$E_{sb} = -\frac{C_{oxb}}{\epsilon_{si}}(u_e - u_{sb}). \tag{5.26}$$

Combining (5.25), (5.26) and (4.10) the coupling between u_{sf} and u_{sb} for FD condition of the Si film is given by [147]

$$u_{sb} = \frac{u_{sf} - u_{cs}}{1 + K(d_{it} + 1)}, \tag{5.27}$$

where

$$u_{cs} = \frac{qN_a t_{si}^2}{2\epsilon_{si}\phi_t} - K(u_{e0} + u_{nt}), \tag{5.28}$$

$$u_{nt} = \frac{q}{C_{oxb}} (\beta N_{ot} + D_{it} u_b), \tag{5.29}$$

and

$$u_{e0} = \frac{V_{GB} - V_{FBB0}}{\phi_t}. \tag{5.30}$$

In (5.27) and (5.28), $K = (\epsilon_{ox} t_{si})/(\epsilon_{si} t_{oxb})$ and $d_{it} = qD_{it}/C_{oxb}$. For partial depletion (PD) condition of the Si film, u_{sf} and u_{sb} are decoupled and (5.27) is no longer valid. In this case, u_{sb} is denoted u_{sb0} and is obtained from [148]

$$\frac{t_{oxf}^2}{t_{oxb}^2}(u_e - u_{sb0})^2 = G^2(e^{-u_{sb0}} + u_{sb0} - 1). \tag{5.31}$$

The transition between PD and FD condition is then described by the following smoothing function [144, 145, 147]:

$$u_{sb} = u_{sb0} + \ln\left[1 + \exp\left(\frac{u_{sf} - u_{cs}}{1 + K(d_{it} + 1)} - u_{sb0}\right)\right]. \tag{5.32}$$

For $u_{sf} < u_{cs} + u_{sb0}(1+K(d_{it}+1)) - 3$, the Si film is partially depleted and the exponential term in (5.32) is negligible, therefore $u_{sb} \approx u_{sb0}$. However, when $u_{sf} > u_{cs} + u_{sb0}(1+K(d_{it}+1)) + 3$, the exponential term in (5.32) is much greater than 1. In this case the device operates in FD condition and (5.32) converges to the condition determined by (5.27).

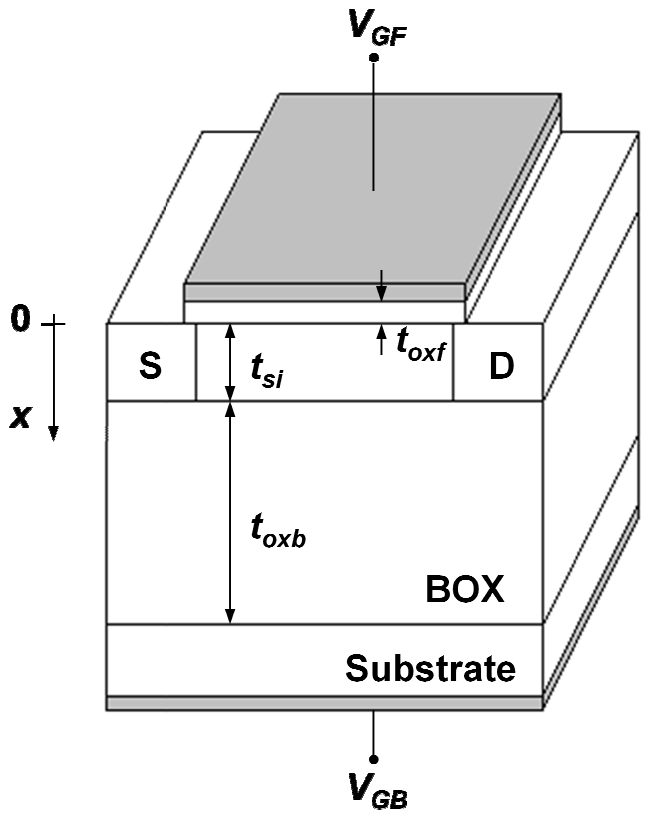

Fig. 5.7. Schematic representation of an SOI MOSFET structure.

The front- and back-side surface potentials at the source (ψ_{sf0} and ψ_{sb0}) and at the drain (ψ_{sfL} and ψ_{sbL}) ends are obtained by simultaneously solving (5.23) and (5.32). From the solutions to ψ_{sf} and ψ_{sb}, the drain current (I_d) can be calculated through the Pao-Sah double integral [134] or from charge-sheet model (CSM) approximations as described in [149]. A comparison of the surface potentials (i.e., ψ_{sf} and ψ_{sb}) computed through the model by solving (5.23) and (5.32) with 2D TCAD simulations using Silvaco ATLAS is given in Fig. 5.8. For the simulations, a uniform distribution of fixed charge and interface states at the Si-BOX interface is used. A comparison of the I_d-V_{GF} characteristics computed from CSM

approximations with results from TCAD simulations is given in Fig. 5.9 for both a logarithmic and linear scale of the y-axis.

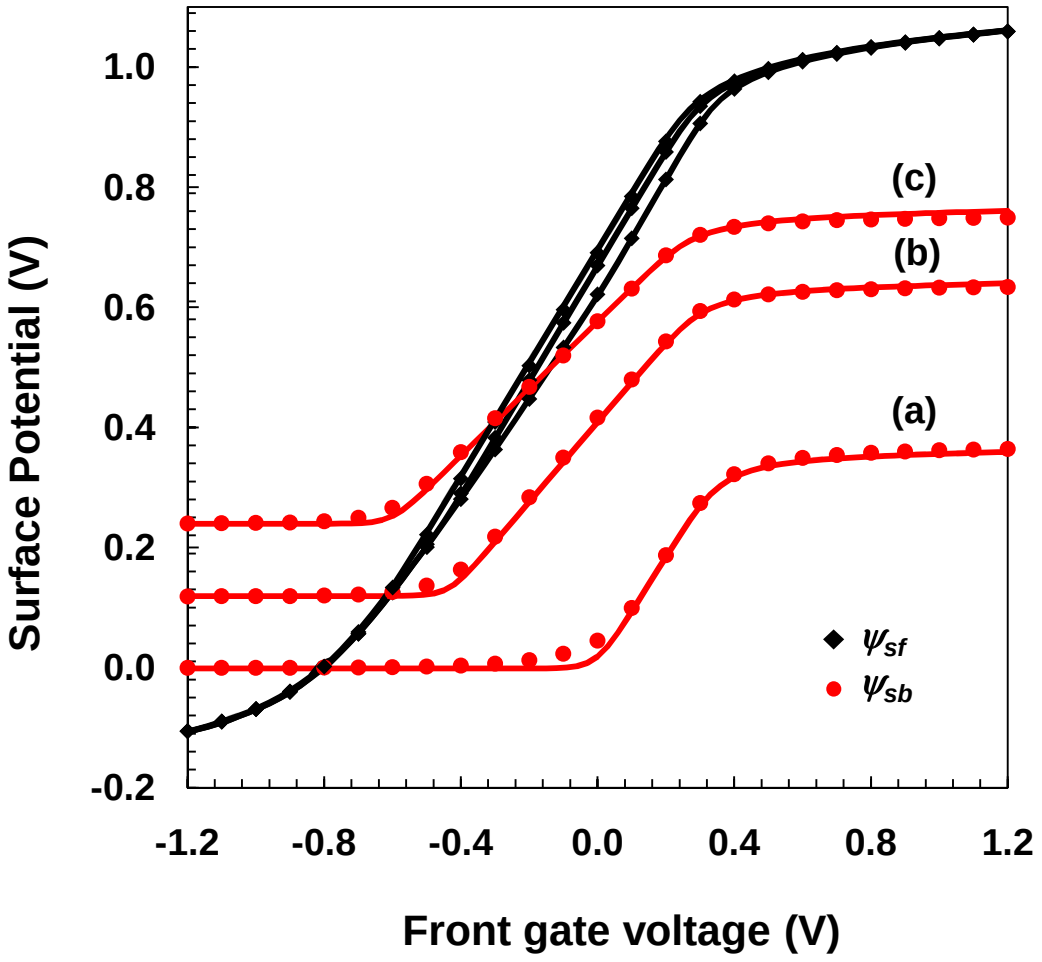

Fig. 5.8. ψ_{sf} and ψ_{sb} vs. V_{GF} at three different densities of N_{ot} and D_{it}: a) N_{ot} = 0, D_{it} = 0; b) N_{ot} = 6×10^{11} cm^{-2}, D_{it} = 6×10^{11} cm^{-2}eV^{-1}; and c) N_{ot} = 1×10^{12} cm^{-2}, D_{it} = 1×10^{12} cm^{-2}eV^{-1}. Symbols are 2D TCAD simulations and solid lines are numerical calculations using (5.23) and (5.32). For these results t_{si} = 40 nm, t_{oxf} = 2 nm, t_{oxb} = 200 nm, V_{FBF0} = –0.8 V, L = 1 μm, W = 20 μm, V_{GB} = 0 V and V_{ds} = 50 mV.

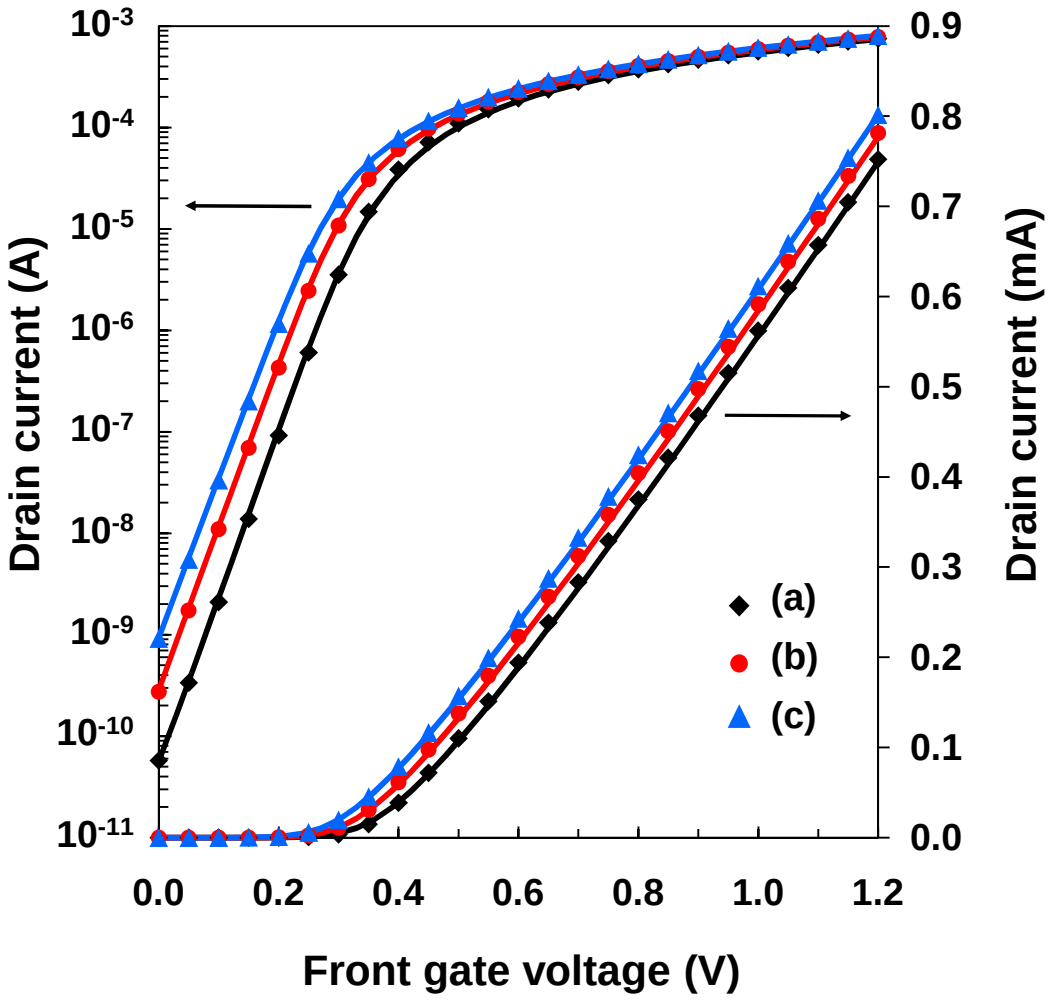

Fig. 5.9. Drain current (I_d) vs. V_{GF} at three different densities of N_{ot} and D_{it}: a) N_{ot} = 0, D_{it} = 0; b) N_{ot} = 4×10^{11} cm^{-2}, D_{it} = 4×10^{11} cm^{-2}eV^{-1}; and c) N_{ot} = 8×10^{11} cm^{-2}, D_{it} = 8×10^{11} cm^{-2}eV^{-1}. Symbols are obtained from 2D TCAD simulations and solid lines are obtained numerically through CSM calculations using solutions for ψ_{sf} and ψ_{sb} given by (5.23) and (5.32). Same parameters as in Fig. 5.8.

Additional verification is obtained through the comparison of I_{off} given by the model with TCAD simulations as a function of radiation-induced defect densities N_{ot} and D_{it}, for different values of t_{si} as shown in Fig. 5.10. These results demonstrate the accurate modeling of I_{off} as well as the correct description of the transition between PD and FD of the Si film as a function of radiation-induced

charge buildup at the Si-BOX interface. For t_{si} below 40 nm, the Si film is in FD and any increase of charge buildup at the Si-BOX interface results in an increase in I_{off} due to the coupling of the front and back surfaces. However, for t_{si} above 40 nm, the Si film in initially in PD and requires a significant amount of charge buildup at the Si-BOX interface before the device operates in FD and a measurable increase in I_{off} is obtained as a result of vertical coupling. As shown in Fig. 5.10, for a t_{si} of 70 nm and above, radiation-induced defect densities up to N_{ot} = 10^{12} cm^{-2} and D_{it} = 10^{12} $cm^{-2}eV^{-1}$ are not sufficient to transition the device operation into FD and therefore have no effect in I_{off}.

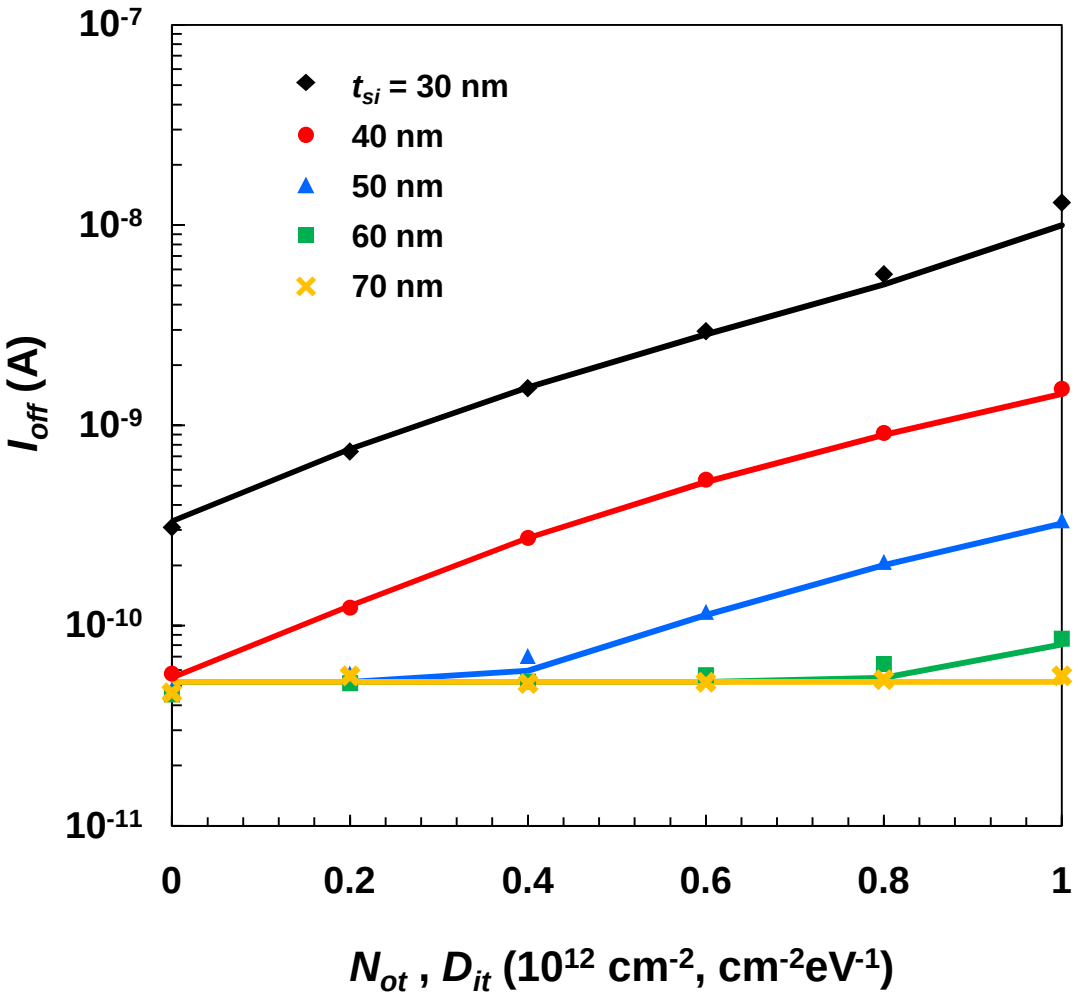

Fig. 5.10. Off-state leakage current (I_{off}) vs. N_{ot} and D_{it} (same density) for different Si-film thicknesses (t_{si}). Symbols are obtained from 2D TCAD simulations and solid lines are calculated analytically through the CSM using solutions for ψ_{sf} and ψ_{sb} given by (5.23) and (5.32). Same parameters as given in Fig. 5.8 except t_{si}.

CHAPTER 6. CONCLUSIONS

6.1 Summary and Contributions

As reported in this dissertation and in several recent studies, the radiation-induced degradation in advanced deep-submicron CMOS technologies has been significantly reduced by scaling. Nonetheless, damage to isolating field oxides, specifically STI oxides, remains a significant threat with existent implications on the response of IC fabricated in these technologies and operating in harsh radiation environments. Moreover, the experimental characterization and modeling of radiation effects in these technologies remains an important task as new discoveries of potential threats, radiation hardening challenges and radiation effects related to new technological aspects continue to appear. The incorporation of TID simulation capabilities into industry standard compact models is of great value to designers of integrated circuits (ICs) used in harsh radiation environment, as the use of commercial deep-submicron technologies has greatly increased for these applications. Radiation-enabled compact models represent *the* bridge between physics-based descriptions of basic TID effects mechanisms and the practical art of IC design.

This dissertation covers several topics related to the modeling of TID effects in advanced CMOS technologies. The topics discussed in this dissertation include different levels of modeling, covering from the basic physical mechanism of radiation damage in MOS structures to the incorporation of TID effects into PSP, the industry standard surface potential based compact model for modern MOSFET devices. An important contribution of this work is a comprehensive

study of the physical mechanisms contributing to the buildup of N_{ot} and N_{it} in STI oxides of advanced CMOS technologies by using a physical model based on time-dependent kinetic calculations for charge generation, transport and trapping in SiO_2 during exposure to ionizing radiation. Using this model it is possible to determine key mechanisms required to model the dependence of the buildup on external conditions (e.g., dose-rate, bias); and formulating analytical models that are suitable for incorporation into advanced surface-potential-based compact models.

Chapter 1 of this dissertation provided background information and an overview of radiation effects in MOS technologies. The remaining chapters present detailed description of modeling techniques for advanced CMOS devices. Chapter 2 focuses on the basic mechanisms of TID effects in advanced CMOS technologies and reviews a selection of experimental data characterizing the physical mechanisms contributing to radiation effects in STI oxides. Key reactions leading to the buildup of radiation-induced defects (N_{ot} and N_{it}) in STI oxides is presented in this chapter. This set of reactions is then formulated into a physical model that describes the time-dependent effects of ionizing radiation in the oxide regions of advanced CMOS technologies. Experimental data from FOXFET test structures fabricated in a low-standby power (LSP) high performance 90 nm commercial bulk CMOS technology are presented in this dissertation. The experimental results allow characterizing the radiation response of STI oxides and to investigate the basic mechanism of radiation damage by comparison and parameterization of the physical model. Analytical description for

the buildup of N_{ot} and N_{it} were presented in Chapter 4 of this dissertation. The time-dependent buildup of N_{ot} and N_{it} are analytically calculated using general equations that describe the generation, transport and trapping of holes as well as the reaction of holes with hydrogenated defects resulting in the release of protons and subsequent formation of interface traps. When used in conjunction with closed-form expressions for surface potential, the analytical models enable an accurate description of radiation-induced degradation of transistor electrical characteristics allowing the incorporation of TID effects into surface potential based compact models. The incorporation is accomplished through modifications of the surface potential equations (SPE), allowing the inclusion of radiation-induced defects (i.e., N_{ot} and N_{it}) into the calculations of surface potential. Verification of the compact modeling approach was achieved via comparison with experimental data for degraded current-voltage (I_d-V_{gs}) characteristics as well as radiation-induced degradation parameters, such as threshold voltage shifts, increase in off-state leakage current and changes in the subthreshold swing in advanced bulk and SOI CMOS technologies.

In summary, the primary contributions of the work presented in this dissertation are: (i) a comprehensive study of the physical mechanisms contributing to the radiation response of advanced CMOS technologies by means a physical model based on kinetic equations for charge generation, transport and trapping in SiO_2, (ii) the introduction of a new analytical model that describes the buildup of N_{it} in STI oxides of advanced CMOS technologies, (iii) introduction of a new approach for the incorporation of TID effects into advanced surface

potential based compact model for advanced bulk and SOI CMOS technologies, and (iv) demonstration of the compact modeling approach by comparison with experimental data and TCAD simulations.

6.2 Recommendations for Future Work

I have several recommendations for future work on this subject. First, I recommend that a detailed study of prompt interface trap formation in STI oxides of deep-submicron CMOS technologies should be done. Previous studies have shown that these fast interface trap formation mechanisms contribute only a small percentage of the total density of radiation-induced interface traps; however, this might not be true for advanced technologies with deposited STI oxides. Additionally, TID experiments on the FOXFETs using charge pumping techniques should provide useful information on the formation of border traps near the Si-SiO_2 interface of STI oxides in deep-submicron CMOS technologies. Also, an investigation of the effects of hydrogen in the radiation and dose rate response of STI oxides may also provide significant information on the physical mechanisms that contribute to the buildup of interface traps. In this investigation, FOXFETs can be irradiated at different dose rates in environments containing different concentrations of molecular hydrogen. With respect to the compact modeling approach, further validation of the analytical models for N_{ot} and N_{it} can be obtained by comparison with experimental result from different radiation experiments. Additionally, the demonstration of the compact modeling approach by reproduction of radiation-induced degradation in an IC application should serve as further validation.

REFERENCES

[1] T. P. Ma and P. V. Dressendorfer, *Ionizing Radiation Effects in MOS Devices and Circuits*. New York: Wiley, 1989.

[2] W. E. Johnson and K. L. Horovitz, "Neutron Irradiated Semiconductors," *Physical Review,* vol. 76, p. 442, 1949.

[3] H. L. Hughes and R. R. Giroux, "Space Radiation Affects MOSFET's," *Electronics,* vol. 37, no. 32, pp. 58-60, 1964.

[4] H. L. Hughes, "Surface Effects of Space Radiation on Silicon Devices," *IEEE Trans. Nucl. Sci.,* vol. 12, pp. 53-63, 1965.

[5] H. L. Hughes, "Radiation Effects on Evacuated and Gas Encapsulated Commercially Available Silicon Planar Transistors," *Bull. Am. Phys. Soc. ,* vol. 9, p. 655, 1965.

[6] E. Kooi, "Influence of X-ray Irradiations on the Charge Distribution of Metal-Oxide-Silicon Structures," *Philips Res. Rept.,* vol. 20, p. 306, 1965.

[7] E. Kooi, "Effects of Ionizing Irradiations on the Properties of Oxide-Covered Silicon Surfaces," *Philips J. Res.,* vol. 20, pp. 595-619, 1965.

[8] J. R. Szedon and J. E. Sandor, "The Effect Of Low-Energy Electron Irradiation of Metal-Oxide-Semiconductor Structures," *Appl. Phys. Letters,* vol. 6, p. 18, 1965.

[9] K. H. Zaininger, "Electron Bombardment of MOS Capacitors," *Applied Physics Letters,* vol. 8, pp. 140-142, 1966.

[10] J. F. Leavy and R. A. Poll, "Radiation-Induced Integrated Circuit Latchup," *IEEE Trans. Nucl. Sci.,* vol. 16, pp. 96-103, 1969.

[11] H. L. Hughes, "A Survey of Radiation-Induced Perturbations in Metal-Insulator-Semiconductor Structures," in *Reliability Physics Symposium, 1971. 9th Annual,* 1971, pp. 33-39.

[12] H. L. Hughes, "Radiation Effects in MOS VLSI Structures," in *The Physics and Technology of Amorphous SiO_2,* R. A. B. Devine, Ed., ed NY: Plenum Press, 1988, p. 455.

[13] G. E. Davis, H. L. Hughes, and T. I. Kamins, "Total Dose Radiation-Bias Effects in Laser-Recrystallized SOI MOSFET's," *IEEE Trans. Nucl. Sci.,* vol. 29, pp. 1685-1689, 1982.

[14] J. A. Appels, E. Kooi, M. M. Paffen, J. J. H. Schatorje, and W. H. Verkuylen, "Local Oxidation of Silicon and Its Application in Semiconductor Device Technology," *Phillips Res. Rep,* vol. 25, p. 118, 1970.

[15] N. S. Saks and M. G. Ancona, "Generation of interface states by ionizing radiation at 80K measured by charge pumping and subthreshold slope techniques," *IEEE Trans. Nucl. Sci.,* vol. 34, pp. 1348-1354, 1987.

[16] H. J. Barnaby, "Total-Ionizing-Dose Effects in Modern CMOS Technologies," *IEEE Trans. Nucl. Sci.,* vol. 53, pp. 3103-3121, 2006.

[17] H. J. Barnaby, M. L. McLain, and I. S. Esqueda, "Total-ionizing-dose effects on isolation oxides in modern CMOS technologies," *Nucl. Instr. and Meth in Phys. Res. Sect. B,* vol. 261, pp. 1142-1145, Aug. 2007.

[18] F. T. Brady, J. D. Maimon, and M. J. Hurt, "A scaleable, radiation hardened shallow trench isolation," *IEEE Trans. Nucl. Sci.,* vol. 46, no. 6, pp. 1836-1840, Dec. 1999.

[19] R. C. Lacoe, "CMOS scaling design principles and hardening by design methodology," *IEEE NSREC Short Course,* 2003.

[20] T. R. Oldham and F. B. McLean, "Total ionizing dose effects in MOS oxides and devices," *IEEE Trans. Nucl. Sci.,* vol. 50, no. 3, pp. 483-499, Dec. 2003.

[21] H. J. Barnaby, M. L. McLain, I. S. Esqueda, and C. Xiao Jie, "Modeling Ionizing Radiation Effects in Solid State Materials and CMOS Devices," *IEEE Transaction on Circuits and Systems I,* vol. 56, pp. 1870-1883, 2009.

[22] L. T. Clark, K. C. Mohr, K. E. Holbert, Y. Xiaoyin, J. Knudsen, and H. Shah, "Optimizing Radiation Hard by Design SRAM Cells," *IEEE Trans. Nucl. Sci.,* vol. 54, pp. 2028-2036, 2007.

[23] X. Yao, N. Hindman, L. T. Clark, K. E. Holbert, D. R. Alexander, and W. M. Shedd, "The Impact of Total Ionizing Dose on Unhardened SRAM Cell Margins," *IEEE Trans. Nucl. Sci.,* vol. 55, pp. 3280-3287, 2008.

[24] Y. Taur and T. H. Ning, *Fundamentals of VLSI Devices*: Cambridge University Press, 1998.

[25] H. J. Barnaby and I. S. Esqueda, "Modeling Ionizing Radiation Effects in Solid State Materials and CMOS Devices," *GOMAC conference,* 2010.

[26] R. Ladbury, "Radiation Hardening at the System Level," *IEEE NSREC Short Course,* 2007.

[27] K. A. LaBel, A. H. Johnston, J. L. Barth, R. A. Reed, and C. E. Barnes, "Emerging radiation hardness assurance (RHA) issues: a NASA approach for space flight programs," *IEEE Trans. Nucl. Sci.,* vol. 45, pp. 2727-2736, 1998.

[28] M. L. McLain, "Analysis and Modeling of Total Dose Effects in Advanced Bulk CMOS Technologies," Doctor of Philosophy, School of Electrical Computer and Energy Engineering, Arizona State University, 2009.

[29] J. R. Schwank, "Total Dose Effects in MOS Devices," *IEEE NSREC Short Course,* 2002.

[30] G. A. Ausman and F. B. McLean, "Electron-hole pair creation energy in SiO_2," *Appl. Phys. Lett.,* vol. 26, pp. 173-177, 1975.

[31] J. M. Benedetto and H. E. Boesch, "The Relationship between 60Co and 10-keV X-Ray Damage in MOS Devices," *IEEE Trans. Nucl. Sci.,* vol. 33, pp. 1317-1323, 1986.

[32] J. R. Schwank, "Basic mechanisms of radiation effects in the natural space environment," *IEEE NSREC Short Course,* 1994.

[33] R. C. Hughes, "Charge-Carrier Transport Phenomena in Amorphous SiO_2: Direct Measurement of the Drift Mobility and Lifetime," *Physical Review Letters,* vol. 30, p. 1333, 1973.

[34] H. E. Boesch, F. B. McLean, J. M. McGarrity, and G. A. Ausman, "Hole Transport and Charge Relaxation in Irradiated SiO_2 MOS Capacitors," *IEEE Trans. Nucl. Sci.,* vol. 22, pp. 2163-2167, 1975.

[35] T. R. Oldham, *Ionizing Radiation Effects in MOS Oxides*. NJ: World Scientific Publishing Co. Pte. Ltd., 1999.

[36] T. R. Oldham, "Recombination along the tracks of heavy charged particles in SiO_2 films," *Journal of Applied Physics,* vol. 57, pp. 2695-2702, 1985.

[37] T. R. Oldham, "Analysis of damage in MOS devices in several radiation environments," *IEEE Trans. Nucl. Sci.,* vol. 31, no. 6, pp. 1236-1241, Dec. 1984.

[38] T. R. Oldham and J. M. McGarrity, "Comparison of 60Co Response and 10 KeV X-Ray Response in MOS Capacitors," *IEEE Trans. Nucl. Sci.,* vol. 30, pp. 4377-4381, 1983.

[39] T. R. Oldham and J. M. McGarrity, "Ionization of SiO_2 by Heavy Charged Particles," *IEEE Trans. Nucl. Sci.,* vol. 28, pp. 3975-3980, 1981.

[40] H. E. Boesch and J. M. McGarrity, "Charge Yield and Dose Effects in MOS Capacitors at 80 K," *IEEE Trans. Nucl. Sci.,* vol. 23, pp. 1520-1525, 1976.

[41] O. L. Curtis, J. R. Srour, and K. Y. Chiu, "Hole and Electron Transport in SiO_2," *J. Appl. Phys.,* vol. 45, p. 4506, 1974.

[42] P. Paillet, J. R. Schwank, M. R. Shaneyfelt, V. Ferlet-Cavrois, R. L. Jones, O. Flarrient, and E. W. Blackmore, "Comparison of charge yield in MOS devices for different radiation sources," *IEEE Trans. Nucl. Sci.,* vol. 49, pp. 2656-2661, 2002.

[43] H. E. Boesch, F. B. McLean, J. M. McGarrity, and P. S. Winokur, "Enhanced Flatband Voltage Recovery in Hardened Thin MOS Capacitors," *IEEE Trans. Nucl. Sci.,* vol. 25, pp. 1239-1245, 1978.

[44] H. E. Boesch, J. M. McGarrity, and F. B. McLean, "Temperature- and Field-Dependent Charge Relaxation in SiO_2 Gate Insulators," *IEEE Trans. Nucl. Sci.,* vol. 25, pp. 1012-1016, 1978.

[45] F. B. McLean, H. E. Boesch, and J. M. McGarrity, "Dispersive Hole Transport in SiO_2," Harry Diamond Laboratories Adelphi, MD1987.

[46] F. B. McLean, H. E. Boesch, and J. M. McGarrity, "Field-Dependent Hoel Transport in Amorphous SiO_2," in *The Physics of SiO_2 and Its Interfaces*, S. T. Pantelides, Ed., ed NY: Pergamon Press, 1978, p. 19.

[47] E. W. Montroll and G. H. Weiss, "Random Walks on Lattices. II," *Journal of Mathematical Physics,* vol. 6, pp. 167-181, 1965.

[48] F. B. McLean, H. E. Boesch, and J. M. McGarrity, "Hole Transport and Recovery Characteristics of SiO_2 Gate Insulators," *IEEE Trans. Nucl. Sci.,* vol. 23, pp. 1506-1512, 1976.

[49] F. B. McLean, J. G. A. Ausman, J. H. E. Boesch, and J. M. McGarrity, "Application of stochastic hopping transport to hole conduction in amorphous SiO_2," *Journal of Applied Physics,* vol. 47, pp. 1529-1532, 1976.

[50] R. C. Hughes, "Hole mobility and transport in thin SiO_2 films," *Appl. Phys. Lett.*, vol. 26, pp. 436-438, 1975.

[51] R. C. Hughes, E. P. EerNisse, and H. J. Stein, "Hole Transport in MOS Oxides," *IEEE Trans. Nucl. Sci.*, vol. 22, pp. 2227-2233, 1975.

[52] H. J. Barnaby, "Total-dose effects in modern integrated circuits," *IEEE NSREC Short Course*, 2005.

[53] D. M. Fleetwood, "Emerging issues for total ionizing dose effects on microelectronics," *NSREC Short Course*, 2002.

[54] P. M. Lenahan and P. V. Dressendorfer, "Hole traps and trivalent silicon centers in metal/oxide/silicon devices," *Journal of Applied Physics*, vol. 55, pp. 3495-3499, 1984.

[55] F. J. Feigl, W. B. Fowler, and K. L. Yip, "Oxygen vacancy model for the E1' center in SiO_2," *Solid State Communications*, vol. 14, pp. 225-229, 1974.

[56] C. J. Nicklaw, Z. Y. Lu, D. M. Fleetwood, R. D. Schrimpf, and S. T. Pantelides, "The structure, properties, and dynamics of oxygen vacancies in amorphous SiO_2," *IEEE Trans. Nucl. Sci.*, vol. 49, pp. 2667-2673, 2002.

[57] P. J. McWhorter, S. L. Miller, and W. M. Miller, "Modeling the anneal of radiation-induced trapped holes in a varying thermal environment," *IEEE Trans. Nucl. Sci.*, vol. 37, pp. 1682-1689, 1990.

[58] F. B. McLean, "A Framework for Understanding Radiation-Induced Interface States in SiO_2 MOS Structures," *IEEE Trans. Nucl. Sci.*, vol. 27, pp. 1651-1657, 1980.

[59] D. B. Brown, "The Time Dependence of Interface State Production," *IEEE Trans. Nucl. Sci.*, vol. 32, pp. 3899-3904, 1985.

[60] D. L. Griscom, "Diffusion of radiolytic molecular hydrogen as a mechanism for the post-irradiation buildup of interface states in SiO_2-on-Si structures," *Journal of Applied Physics*, vol. 58, pp. 2524-2533, 1985.

[61] F. J. Grunthaner, P. J. Grunthaner, and J. Maserjian, "Radiation-Induced Defects in SiO_2 as Determined with XPS," *IEEE Trans. Nucl. Sci.*, vol. 29, pp. 1462-1466, 1982.

[62] F. J. Grunthaner, B. F. Lewis, N. Zamini, J. Maserjian, and A. Madhukar, "XPS Studies of Structure-Induced Radiation Effects at the Si/SiO_2 Interface," *IEEE Trans. Nucl. Sci.*, vol. 27, pp. 1640-1646, 1980.

[63] P. S. Winokur, J. H. E. Boesch, J. M. McGarrity, and F. B. McLean, "Two-stage process for buildup of radiation-induced interface states," *Journal of Applied Physics,* vol. 50, pp. 3492-3494, 1979.

[64] P. S. Winokur and M. M. Sokoloski, "Comparison of interface state buildup in MOS capacitors subjected to penetrating and nonpenetrating radiation," *Applied Physics Letters,* vol. 28, pp. 627-630, 1976.

[65] P. S. Winokur, J. M. McGarrity, and H. E. Boesch, "Dependence of Interface-State Buildup on Hole Generation and Transport in Irradiated MOS Capacitors," *IEEE Trans. Nucl. Sci.,* vol. 23, pp. 1580-1585, 1976.

[66] H. E. Boesch, "Time-dependent interface trap effects in MOS devices," *IEEE Trans. Nucl. Sci.,* vol. 35, pp. 1160-1167, 1988.

[67] N. S. Saks, C. M. Dozier, and D. B. Brown, "Time dependence of interface trap formation in MOSFETs following pulsed irradiation," *IEEE Trans. Nucl. Sci.,* vol. 35, pp. 1168-1177, 1988.

[68] P. M. Lenahan and P. V. Dressendorfer, "An electron spin resonance study of radiation induced electrically active paramagnetic centers at the Si/SiO_2 interface," *J. Appl. Phys.,* vol. 54, pp. 1457-1460, 1983.

[69] P. J. Caplan, E. H. Poindexter, B. E. Deal, and R. R. Razouk, "ESR centers, interface states, and oxide fixed charge in thermally oxidized silicon wafers," *J. Appl. Phys.,* vol. 50, pp. 5847-5854, 1979.

[70] E. H. Poindexter, P. J. Caplan, B. E. Deal, and R. R. Razouk, "Interface states and electron spin resonance centers in thermally oxidized (111) and (100) silicon wafers," *J. Appl. Phys.,* vol. 52, pp. 879-884, 1981.

[71] Y. Y. Kim and P. M. Lenahan, "Electron-spin-resonance study of radiation-induced paramagnetic defects in oxides grown on (100) silicon substrates," *J. Appl. Phys.,* vol. 64, pp. 3551-3557, 1988.

[72] A. Stesmans and V. V. Afanas'ev, "Electron spin resonance features of interface defects in thermal (100) Si/SiO_2," *J. Appl. Phys.,* vol. 83, pp. 2449-2457, 1998.

[73] D. K. Schroder and J. A. Babcock, "Negative bias temperature instability: Road to cross in deep submicron silicon semiconductor manufacturing," *Journal of Applied Physics,* vol. 94, p. 1, 2003.

[74] M. L. McLain, "Radiation Induced Inter-Device Leakage Current in 90 nm Bulk CMOS Devices and Circuits," *IEEE Nuclear and Space Radiation Effects Conference (NSREC),* 2008.

[75] C. F. Lin, W. T. Tseng, M. S. Feng, and Y. L. Wang, "A ULSI shallow trench isolation process through the integration of multilayered dielectric process and chemical-mechanical planarization," *Thin Solid Films,* vol. 347, pp. 248-252, 1999.

[76] H. E. Boesch, "Interface-State Generation in Thick SiO_2 Layers," *IEEE Trans. Nucl. Sci.,* vol. 29, pp. 1445-1451, 1982.

[77] M. R. Shaneyfelt, P. E. Dodd, B. L. Draper, and R. S. Flores, "Challenges in hardening technologies using shallow-trench isolation," *IEEE Trans. Nucl. Sci.,* vol. 45, no. 6, pp. 2584-2592, Dec. 1998.

[78] N. S. Saks, M. G. Ancona, and J. A. Modolo, "Generation of Interface States by Ionizing Radiation in Very Thin MOS Oxides," *IEEE Trans. Nucl. Sci.,* vol. 33, pp. 1185-1190, 1986.

[79] N. S. Saks, M. G. Ancona, and J. A. Modolo, "Radiation Effects in MOS Capacitors with Very Thin Oxides at 80°K," *IEEE Trans. Nucl. Sci.,* vol. 31, pp. 1249-1255, 1984.

[80] M. Turowski, A. Raman, and R. Schrimpf, "Nonuniform total-dose-induced charge distribution in shallow-trench isolation oxides," *IEEE Trans. Nucl. Sci.,* vol. 51, pp. 3166-3171, 2004.

[81] I. S. Esqueda, H. J. Barnaby, and M. L. Alles, "Two-dimensional methodology for modeling radiation-induced off-state leakage in CMOS technologies," *IEEE Trans. Nucl. Sci.,* vol. 52, pp. 2259-2264, 2005.

[82] N. Guofu, S. J. Mathew, G. Banerjee, J. D. Cressler, S. D. Clark, M. J. Palmer, and S. Subbanna, "Total dose effects on the shallow-trench isolation leakage current characteristics in a 0.35 μm SiGe BiCMOS technology," *IEEE Trans. Nucl. Sci.,* vol. 46, pp. 1841-1847, 1999.

[83] A. H. Johnston, R. T. Swimm, G. R. Allen, and T. F. Miyahira, "Total Dose Effects in CMOS Trench Isolation Regions," *IEEE Trans. Nucl. Sci.,* vol. 56, pp. 1941-1949, 2009.

[84] R. C. Lacoe, "Improving Integrated Circuit Performance Through the Application of Hardness-by-Design Methodology," *IEEE Trans. Nucl. Sci.,* vol. 55, pp. 1903-1925, 2008.

[85] R. C. Lacoe, J. V. Osborn, R. Koga, S. Brown, and J. Gambles, "Total dose tolerance of the commercial TSMC 0.35μm CMOS process," *2001 IEEE Radiation Effects Data Workshop,* vol. IEEE cat no. 01TH8588, pp. 72-77, 2001.

[86] R. C. Lacoe, J. V. Osborn, R. Koga, S. Brown, and D. C. Mayer, "Application of hardness-by-design methodology to radiation-tolerant ASIC technologies," *IEEE Trans. Nucl. Sci.,* vol. 47, pp. 2334-2341, 2000.

[87] M. McLain, H. J. Barnaby, K. E. Holbert, R. D. Schrimpf, H. Shah, A. Amort, M. Baze, and J. Wert, "Enhanced TID Susceptibility in Sub-100 nm Bulk CMOS I/O Transistors and Circuits," *IEEE Trans. Nucl. Sci.,* vol. 54, pp. 2210-2217, 2007.

[88] V. Goiffon, C. Virmontois, P. Magnan, S. Girard, and P. Paillet, "Analysis of Total Dose-Induced Dark Current in CMOS Image Sensors From Interface State and Trapped Charge Density Measurements," *IEEE Trans. Nucl. Sci.,* vol. 57, pp. 3087-3094, 2010.

[89] F. Faccio, H. J. Barnaby, X. J. Chen, D. M. Fleetwood, L. Gonella, M. McLain, and R. D. Schrimpf, "Total ionizing dose effects in shallow trench isolation oxides," *Microelectronics Reliability,* vol. 48, pp. 1000-1007, 2008.

[90] S. C. Witczak, R. C. Lacoe, J. V. Osborn, J. M. Hutson, and S. C. Moss, "Dose-rate sensitivity of modern nMOSFETs," *IEEE Trans. Nucl. Sci.,* vol. 52, no. 6, pp. 2602-2608, Dec. 2005.

[91] A. H. Johnston, R. T. Swimm, and T. F. Miyahira, "Low Dose Rate Effects in Shallow Trench Isolation Regions," *IEEE Trans. Nucl. Sci.,* vol. 57, pp. 3279-3287, 2010.

[92] H. P. Hjalmarson, R. L. Pease, and R. A. B. Devine, "Calculations of Radiation Dose-Rate Sensitivity of Bipolar Transistors," *IEEE Trans. Nucl. Sci.,* vol. 55, pp. 3009-3015, 2008.

[93] R. E. Stahlbush, A. H. Edwards, D. L. Griscom, and B. J. Mrstik, "Post-irradiation cracking of H2 and formation of interface states in irradiated metal-oxide-semiconductor field-effect transistors," *J. Appl. Phys.,* vol. 73, pp. 658-667, 1993.

[94] B. J. Mrstik and R. W. Rendell, "Si-SiO_2 interface state generation during X-ray irradiation and during post-irradiation exposure to a hydrogen ambient [MOSFET]," *IEEE Trans. Nucl. Sci.,* vol. 38, pp. 1101-1110, 1991.

[95] R. E. Stahlbush, B. J. Mrstik, and R. K. Lawrence, "Post-irradiation behavior of the interface state density and the trapped positive charge," *IEEE Trans. Nucl. Sci.,* vol. 37, pp. 1641-1649, 1990.

[96] H. P. Hjalmarson, R. L. Pease, S. C. Witczak, M. R. Shaneyfelt, J. R. Schwank, A. H. Edwards, C. E. Hembree, and T. R. Mattsson, "Mechanisms for radiation dose-rate sensitivity of bipolar transistors," *IEEE Trans. Nucl. Sci.,* vol. 50, pp. 1901-1909, 2003.

[97] F. B. McLean and T. R. Oldham, "Basic mechanisms of radiation effects in electronic materials and devices," *Harry Diamond Laboratories Technical Report,* vol. HDL-TR, p. 2129, 1987.

[98] M. R. Shaneyfelt, D. M. Fleetwood, J. R. Schwank, and K. L. Hughes, "Charge yield for cobalt-60 and 10-keV x-ray irradiations," *IEEE Trans. Nucl. Sci.,* vol. 38, pp. 1187-1194, 1991.

[99] T. R. Oldham, "Switching oxide traps," in *Radiation Effects and Soft Errors in Integrated Circuits and Electronic Devices*, R. D. Schrimpf and D. M. Fleetwood, Eds., ed New Jersey: World Sci., 2004.

[100] *Radiation Effects Module User's Manual,* 5.9.31.C ed. Santa Clara: Silvaco International, 2005.

[101] D. Braunig and F. Wulf, "Atomic Displacement and Total Ionizing Dose Damage in Semiconductors," *Radiation Phys. Chem.,* vol. vol. 43, pp. pp.105-127, 1994.

[102] C. M. Dozier, D. M. Fleetwood, D. B. Brown, and P. S. Winokur, "An evaluation of low-energy x-ray ad cobalt-60 irradiations of MOS transistors," *IEEE Trans. Nucl. Sci.,* vol. NS-34, pp. 1535-1538, 1987.

[103] D. K. Schroder, *Semiconductor Material and Device Characterization*, 2 ed. NY: Wiley-Interscience, 1998.

[104] R. S. Muller and T. I. Kamins, *Device Electronics for Integrated Circuits* New York: Wiley, 1986.

[105] X. J. Chen, H. J. Barnaby, P. Adell, R. L. Pease, B. Vermeire, and K. E. Holbert, "Modeling the Dose Rate Response and the Effects of Hydrogen in Bipolar Technologies," *IEEE Trans. Nucl. Sci.,* vol. 56, pp. 3196-3202, 2009.

[106] I. G. Batyrev, D. Hughart, R. Durand, M. Bounasser, B. R. Tuttle, D. M. Fleetwood, R. D. Schrimpf, S. N. Rashkeev, G. W. Dunham, M. Law, and S. T. Pantelides, "Effects of Hydrogen on the Radiation Response of Bipolar Transistors: Experiment and Modeling," *IEEE Trans. Nucl. Sci.,* vol. 55, pp. 3039-3045, 2008.

[107] X. J. Chen, H. J. Barnaby, B. Vermeire, K. Holbert, D. Wright, R. L. Pease, G. Dunham, D. G. Platteter, J. Seiler, S. McClure, and P. Adell, "Mechanisms of Enhanced Radiation-Induced Degradation Due to Excess Molecular Hydrogen in Bipolar Oxides," *IEEE Trans. Nucl. Sci.*, vol. 54, pp. 1913-1919, 2007.

[108] P. S. Winokur, J. R. Schwank, P. J. McWhorter, P. V. Dressendorfer, and D. C. Turpin, "Correlating the Radiation Response of MOS Capacitors and Transistors," *IEEE Trans. Nucl. Sci.*, vol. 31, pp. 1453-1460, 1984.

[109] E. W. Enlow, R. L. Pease, W. Combs, R. D. Schrimpf, and R. N. Nowlin, "Response of advanced bipolar processes to ionizing radiation," *IEEE Trans. Nucl. Sci.*, vol. 38, pp. 1342-1351, 1991.

[110] D. M. Fleetwood, S. L. Kosier, R. N. Nowlin, R. D. Schrimpf, R. A. Reber, Jr., M. DeLaus, P. S. Winokur, A. Wei, W. E. Combs, and R. L. Pease, "Physical mechanisms contributing to enhanced bipolar gain degradation at low dose rates," *IEEE Trans. Nucl. Sci.*, vol. 41, pp. 1871-1883, 1994.

[111] S. N. Rashkeev, C. R. Cirba, D. M. Fleetwood, R. D. Schrimpf, S. C. Witczak, A. Michez, and S. T. Pantelides, "Physical model for enhanced interface-trap formation at low dose rates," *IEEE Trans. Nucl. Sci.*, vol. 49, pp. 2650-2655, 2002.

[112] J. Boch, F. Saign, R. D. Schrimpf, J. R. Vaill, L. Dusseau, and E. Lorfvre, "Physical Model for the Low-Dose-Rate Effect in Bipolar Devices," *IEEE Trans. Nucl. Sci.*, vol. 53, pp. 3655-3660, 2006.

[113] L. M. Terman, "An investigation of surface states at a silicon/silicon oxide interface employing metal-oxide-silicon diodes," *Solid-State Electronics*, vol. 5, pp. 285-299, 1962.

[114] P. V. Gray and D. M. Brown, "Density of SiO_2-Si Interface States," *Applied Physics Letters*, vol. 8, pp. 31-33, 1966.

[115] C. Zhang, K. J. Weber, and H. Jin, "Passivation and Depassivation of Si-SiO_2 Interfaces with Atomic Hydrogen," *Journal of The Electrochemical Society*, vol. 156, pp. H836-H840, 2009.

[116] J. L. Autran, F. Seigneur, C. Plossu, and B. Balland, "Characterization of Si–SiO_2 interface states: Comparison between different charge pumping and capacitance techniques," *Journal of Applied Physics*, vol. 74, p. 3932, 1993.

[117] R. L. Pease, "Total ionizing dose effects in bipolar devices and circuits," *IEEE Trans. Nucl. Sci.,* vol. 50, pp. 539-551, 2003.

[118] J. L. Titus, D. Emily, J. F. Krieg, T. Turflinger, R. L. Pease, and A. Campbell, "Enhanced low dose rate sensitivity (ELDRS) of linear circuits in a space environment," *IEEE Trans. Nucl. Sci.,* vol. 46, pp. 1608-1615, 1999.

[119] J. L. Titus, W. E. Combs, T. L. Turflinger, J. F. Krieg, H. J. Tausch, D. B. Brown, R. L. Pease, and A. B. Campbell, "First observations of enhanced low dose rate sensitivity (ELDRS) in space: One part of the MPTB experiment," *IEEE Trans. Nucl. Sci.,* vol. 45, pp. 2673-2680, 1998.

[120] W. Wu, C. Ten-Lon, G. Gildenblat, and C. C. McAndrew, "Physics-based mathematical conditioning of the MOSFET surface potential equation," *IEEE Trans. Electron Devices,* vol. 51, pp. 1196-1199, 2004.

[121] C. C. McAndrew and J. J. Victory, "Accuracy of approximations in MOSFET charge models," *IEEE Trans. Electron Devices,* vol. 49, pp. 72-81, 2002.

[122] D. R. Collins and C. T. Sah, "Effects of X-Ray Irradiation on the Characteristics of Metal-Oxide-Silicon Structures," *Applied Physics Letters,* vol. 8, pp. 124-126, 1966.

[123] M. Gaitan and T. J. Russell, "Measurement of Radiation-Induced Interface Traps Using MOSFETs," *IEEE Trans. Nucl. Sci.,* vol. 31, pp. 1256-1260, 1984.

[124] J. M. Benedetto and H. E. Boesch, "Mosfet and MOS Capacitor Responses to Ionizing Radiation," *IEEE Trans. Nucl. Sci.,* vol. 31, pp. 1461-1466, 1984.

[125] X. J. Chen, H. J. Barnaby, R. L. Pease, R. D. Schrimpf, D. Platteter, M. Shaneyfelt, and B. Vermeire, "Estimation and verification of radiation induced N_{ot} and N_{it} energy distribution using combined bipolar and MOS characterization methods in gated bipolar devices," *IEEE Trans. Nucl. Sci.,* vol. 52, pp. 2245-2251, 2005.

[126] X. J. Chen, H. J. Barnaby, R. D. Schrimpf, D. M. Fleetwood, R. L. Pease, D. G. Platteter, and G. W. Dunham, "Nature of Interface Defect Buildup in Gated Bipolar Devices Under Low Dose Rate Irradiation," *IEEE Trans. Nucl. Sci.,* vol. 53, pp. 3649-3654, 2006.

[127] M. Knoll, D. Braunig, and W. R. Fahrner, "Generation of Oxide Charge and Interface States by Ionizing Radiation and by Tunnel Injection Experiments," *IEEE Trans. Nucl. Sci.*, vol. 29, pp. 1471-1478, 1982.

[128] C. Sah, J. Y. Sun, and J. J.-T. Tzou, "Generation-annealing kinetics of the interface donor states at 0.25 eV above the midgap and the turn-around phenomena on oxidized silicon during avalanche electron injection," *Journal of Applied Physics*, vol. 54, pp. 2547-2555, 1983.

[129] I. S. Esqueda, H. J. Barnaby, K. E. Holbert, and Y. Boulghassoul, "Modeling Inter-Device Leakage in 90 nm Bulk CMOS Devices," *IEEE Trans. Nucl. Sci.*, vol. PP, pp. 1-1, 2011.

[130] A. G. Revesz, "Chemical and Structural Aspects of the Irradiation Behavior of SiO_2 Films on Silicon," *IEEE Trans. Nucl. Sci.*, vol. 24, pp. 2102-2107, 1977.

[131] G. Gildenblat, L. Xin, W. Wu, W. Hailing, A. Jha, R. van Langevelde, G. D. J. Smit, A. J. Scholten, and D. B. M. Klaassen, "PSP: An Advanced Surface-Potential-Based MOSFET Model for Circuit Simulation," *IEEE Trans. Electron Devices*, vol. 53, pp. 1979-1993, 2006.

[132] J. R. Brews, "A charge-sheet model of the MOSFET," *Solid-State Electronics*, vol. 21, pp. 345-355, 1978.

[133] G. Gildenblat, "Derivation of Charge-Sheet Model," *Class notes for EEE 598: Compact Modeling, Arizona State Univerisity*, pp. 1-9, Feb. 16, 2007.

[134] H. C. Pao and C. T. Sah, "Effects of diffusion current on characteristics of metal-oxide (insulator)-semiconductor transistors," *Solid-State Electronics*, vol. 9, pp. 927-937, 1966.

[135] G. Gildenblat, *Private communication, cited with permission.*, 2010.

[136] T. L. Chen and G. Gildenblat, "Symmetric bulk charge linearisation in charge-sheet MOSFET model," *Electronics Letters*, vol. 37, pp. 791-793, 2001.

[137] G. Gildenblat, W. Hailing, C. Ten-Lon, G. Xin, and C. Xiaowen, "SP: an advanced surface-potential-based compact MOSFET model," *Solid-State Circuits, IEEE Journal of*, vol. 39, pp. 1394-1406, 2004.

[138] K. F. Galloway, M. Gaitan, and T. J. Russell, "A Simple Model for Separating Interface and Oxide Charge Effects in MOS Device Characteristics," *IEEE Trans. Nucl. Sci.*, vol. 31, pp. 1497-1501, 1984.

[139] F. W. Sexton and J. R. Schwank, "Correlation of Radiation Effects in Transistors and Integrated Circuits," *IEEE Trans. Nucl. Sci.*, vol. 32, pp. 3975-3981, 1985.

[140] D. Zupac, K. F. Galloway, R. D. Schrimpf, and P. Augier, "Effects of radiation-induced oxide-trapped charge on inversion-layer hole mobility at 300 and 77 K," *Applied Physics Letters*, vol. 60, pp. 3156-3158, 1992.

[141] C. L. Huang and G. S. Gildenblat, "Measurements and modeling of the n-channel MOSFET inversion layer mobility and device characteristics in the temperature range 60-300 K," *IEEE Trans. Electron Devices*, vol. 37, pp. 1289-1300, 1990.

[142] P. A. Muls, G. J. Declerck, and R. J. Van Overstraeten, "Characterization of the Mosfet Operating in Weak Inversion," in *Advances in Electronics and Electron Physics*. vol. Volume 47, L. Marton, Ed., ed: Academic Press, 1978, pp. 197-266.

[143] V. Ferlet-Cavrois, P. Paillet, and O. Faynot, "Radiation Effects in Advanced Single- and Multi-Gate SOI MOSFETs," in *FinFETs and Other Multi-Gate Transistors*, J. P. Colinge, Ed., ed: Springer, 2008.

[144] J. W. Sleight and R. Rios, "A continuous compact MOSFET model for fully- and partially-depleted SOI devices," *IEEE Trans. Electron Devices*, vol. 45, pp. 821-825, 1998.

[145] W. Wu, W. Yao, and G. Gildenblat, "Surface-potential-based compact modeling of dynamically depleted SOI MOSFETs," *Solid-State Electronics*, vol. 54, pp. 595-604, 2010.

[146] I. S. Esqueda, H. J. Barnaby, M. L. McLain, P. C. Adell, F. E. Mamouni, S. K. Dixit, R. D. Schrimpf, and W. Xiong, "Modeling the Radiation Response of Fully-Depleted SOI n-Channel MOSFETs," *IEEE Trans. Nucl. Sci.*, vol. 56, pp. 2247-2250, 2009.

[147] I. S. Esqueda, H. J. Barnaby, K. E. Holbert, F. El-Mamouni, and R. D. Schrimpf, "Modeling of Ionizing Radiation-Induced Degradation in Multiple Gate Field Effect Transistors," *IEEE Trans. Nucl. Sci.*, vol. 58, pp. 499-505, 2011.

[148] W. Wu, Y. Wei, G. Gildenblat, and A. J. Scholten, "Compact Modeling of Junction Current in Dynamically Depleted SOI MOSFETs," *IEEE Trans. Electron Devices*, vol. 55, pp. 3295-3298, 2008.

[149] C. Mallikarjun and K. N. Bhat, "Numerical and charge sheet models for thin-film SOI MOSFETs," *IEEE Trans. Electron Devices,* vol. 37, pp. 2039-2051, 1990.

[150] C. M. Snowden, *Introduction to Semiconductor Device Modeling*: World Scientific, 1986.

APPENDIX I. DISCRETIZATION OF CONTINUITY EQUATIONS

Full expansion of the continuity equations for the mobile species (i.e., *n*, *p*, and H^+) given by (2.8), (2.9) and (2.10) is presented in this section of the dissertation. The time-dependent Scharfetter-Gummel continuity equation discretization can be obtained using "explicit" or "implicit" time-stepping schemes. However, the explicit schemes are inherently unstable and require excessively small time steps [150]. An implicit method that allows a larger stability region and therefore permits using larger time steps is utilized for the discretization. In this approach, the continuity equations are given by

$$
\begin{aligned}
&\frac{D_{n(i-1/2)}}{a_{i-1}} B\left(\frac{\psi_{i-1}^{k+1}-\psi_{i}^{k+1}}{\mathrm{V_t}}\right) n_{i-1}^{k+1} \\
&-\left[\frac{(a_i+a_{i-1})}{2\Delta t}+\frac{D_{n(i+1/2)}}{a_i} B\left(\frac{\psi_{\mathrm{i}}^{k+1}-\psi_{\mathrm{i}+1}^{k+1}}{V_t}\right)\right. \\
&\left.+\frac{D_{n(i-1/2)}}{a_{i-1}} B\left(\frac{\psi_{\mathrm{i}}^{k+1}-\psi_{\mathrm{i}-1}^{k+1}}{V_t}\right)\right] n_{i}^{k+1} \\
&+\frac{D_{n(i+1/2)}}{a_i} B\left(\frac{\psi_{\mathrm{i}+1}^{k+1}-\psi_{\mathrm{i}}^{k+1}}{V_t}\right) n_{i+1}^{k+1} \\
&=\left(R_n-G_n-\frac{n_i^k}{\Delta t}\right)\frac{(a_i+a_{i-1})}{2},
\end{aligned}
\tag{A.1}
$$

$$
\begin{aligned}
&\frac{D_{p(i-1/2)}}{a_{i-1}} B\left(\frac{\psi_i^{k+1}-\psi_{i-1}^{k+1}}{V_t}\right) p_{i-1}^{k+1} \\
&- \left[\frac{(a_i + a_{i-1})}{2\Delta t} + \frac{D_{p(i+1/2)}}{a_i} B\left(\frac{\psi_{i+1}^{k+1}-\psi_i^{k+1}}{V_t}\right)\right. \\
&\left. + \frac{D_{p(i-1/2)}}{a_{i-1}} B\left(\frac{\psi_{i-1}^{k+1}-\psi_i^{k+1}}{V_t}\right)\right] p_i^{k+1} \\
&+ \frac{D_{p(i+1/2)}}{a_i} B\left(\frac{\psi_i^{k+1}-\psi_{i+1}^{k+1}}{V_t}\right) p_{i+1}^{k+1} \\
&= \left(R_p - G_p - \frac{p_i^k}{\Delta t}\right)\frac{(a_i + a_{i-1})}{2}
\end{aligned}
\tag{A.2}
$$

and

$$
\begin{aligned}
&\frac{D_{H^+(i-1/2)}}{a_{i-1}} B\left(\frac{\psi_i^{k+1}-\psi_{i-1}^{k+1}}{V_t}\right) {n_{H^+}}_{i-1}^{k+1} \\
&- \left[\frac{(a_i + a_{i-1})}{2\Delta t} + \frac{D_{H^+(i+1/2)}}{a_i} B\left(\frac{\psi_{i+1}^{k+1}-\psi_i^{k+1}}{V_t}\right)\right. \\
&\left. + \frac{D_{H^+(i-1/2)}}{a_{i-1}} B\left(\frac{\psi_{i-1}^{k+1}-\psi_i^{k+1}}{V_t}\right)\right] {n_{H^+}}_i^{k+1} \\
&+ \frac{D_{H^+(i+1/2)}}{a_i} B\left(\frac{\psi_i^{k+1}-\psi_{i+1}^{k+1}}{V_t}\right) {n_{H^+}}_{i+1}^{k+1} \\
&= \left(R_{H^+} - G_{H^+} - \frac{{n_{H^+}}_i^k}{\Delta t}\right)\frac{(a_i + a_{i-1})}{2}.
\end{aligned}
\tag{A.3}
$$

In (A.1) – (A.3), a_i is the distance between adjacent nodes at the *i*-th mesh location and *k* refers to the time step. The discretization of the continuity

equations follows a backward Euler method where the continuity equations are made implicit in carrier concentration and velocity (i.e., implicit in potential). As described in [150], explicit solutions of the continuity equations require restricting the time steps Δt to the order of the dielectric relaxation time and the space steps Δx should not be larger than a Debye length. Both of these parameters are a function of the doping density and the dielectric permittivity. Although, the use of implicit schemes and Scharfetter-Gummel discretization alleviates the restriction on Δt and Δx, using smaller values yield more accurate results.